Airborne Wind Energy System: Flight Data Analysis Using System Identification and Machine Learning, and Control of Launching

モスタファ, アリ, モハメド, ルシュディ

Airborne Wind Energy Systems: Flight Data Analysis Using System Identification and Machine Learning, and Control of Launching

by

Mostafa Ali Rushdi

Submitted to the Earth System Science and Technology
in partial fulfillment of the requirements for the degree of

Doctor of Philosophy in Engineering

at

Kyushu University

March 2021

Airborne Wind Energy Systems: Flight Data Analysis Using System Identification and Machine Learning, and Control of Launching

by

Mostafa Ali Rushdi

Submitted to the Earth System Science and Technology
on June 9th, 2020, in partial fulfillment of the
requirements for the degree of
Doctor of Philosophy in Engineering

Abstract

This research investigates several aspects of a new paradigm for utilizing wind energy, namely harvesting energy from wind at high altitudes, conveniently called the paradigm of Airborne Wind Energy (AWE). Systems were developed according to this paradigm constitute an emerging technology for harvesting energy from wind of steady high speed without the need of a heavy tower and foundation, such as wind turbines used for generating energy from surface-level wind. The most prominent part of an AWE system is a device or vehicle flying in the air while being mechanically connected to the ground (e.g., tethered kites or tethered balloons, which employ a tether for ground connection). Such an AWE system al-

lows the beneficial exploitation of the relative velocity between the wind the AWE vehicle.

The 7 kW kite system of Kyushu University including the system's design, tests, and experimental results was demonstrated. The kite system consists of an inflatable kite with fixed tether length. The kite is controlled by a device, called kite control unit (KCU). With the help of a small measurement unit mounted on the leading edge of the kite, it is able to measure its location and orientation. Several tests had been performed to analyze the kite performance, and tension forces result from those tests are presented in different truck speeds and flight cases.

After collecting the data from the flight tests, the next step was post-processing and data analysis. Starting the analysis with using the system identification (SI) to come up with a simple model for the kite using Plackett's algorithm, which is based on one input (roll angle of the kite) and the output tension. So, in the future, it could be possible apply and implement any control technique to stabilize the kite in a real-time flight.

Expanding the analysis by adding more features, and making a detailed sensitivity analysis; data-based and model-based were presented and showed consistency. The resultant highly correlated features with the output feature (tension) were stated. Then several Machine Learning

(ML) algorithms were applied to predict the value of the tension forces, so it could be possible to know the power production amount in different cases in the future. The Neural Network (NN) algorithm proves a clear success in fitting the data of AWE towing tests. This study is the main novelty of the thesis, as it is the first attempt to ML within the AWE community.

The thesis presents another notable contribution along a different line of research pertaining to another flying vehicle type. It was observed that the soft kites may have some problems in launching, which makes many pioneering AWE companies started to explore ways to simplify this process and they found that the simple solution is to use a rigid wing flying devices with vertical take-off and landing (VTOL) capabilities. To catch up with the promising research concerning such devices, a detailed study was presented, which concerns with the control and simulation of the transition phase of the AP-2 aircraft, recently developed by a leading AWE company, namely, Ampyx Power. By applying optimal control, it was able to find the control action sequence to perform the transition maneuver in two cases; minimum time and minimum power. It has been found that the minimum power case is more appropriate and will have a notable effect on the whole cycle. This study is an important prelude

to a complete study of the overall pumping cycle, including not only the transition phse, but also both its preceding phase (VTOL phase) and succeeding phase (flight-mode phase).

It could be summarized that the novelties within the thesis are stated, in order according to importance, as follows:

- Prediction of the power generated from the kite system. It is the first attempt within the AWE community to employ machine learning techniques to the AWE problems.
- Achieving the optimal trajectory of the transition phase based on minimum power criteria.
- Data-based system identification for the kite.

Thesis Supervisor: Shigeo Yoshida
Title: Professor
Date: December 23rd, 2020

Acknowledgments

First of all, I would like to express my deepest gratitude to my supervisor; Prof. Shigeo Yoshida for his continuous support, technical guidance, and providing the perfect work environment. Your precious comments and mentoring have improved the quality and output of this work throughout the whole three years. I am so grateful and so proud to be a member of the laboratory of Professor Yoshida.

Prof. Changhong Hu (Kyushu University) and Prof. Yasutake Takahashi (University of Fukui); thank you so much for your precious time reviewing my thesis. Your valuable comments and suggestions have enhanced the quality of my work.

I have to thank the Shiroishi Town and Saga Sports Flight Club for giving us the opportunity to perform the flight tests at their place. The collected data from these tests were very important in this thesis.

I should also thank the Ministry of Education, Culture, Sports, Science, and Technology (MEXT), Japan government, for completely funding my PhD research and degree. Also, I should thank the Interdisciplinary Graduate School of Engineering Sciences (IGSES) for funding the expenses of my internships and scientific conferences.

I must thank the student support center and the support section in IGSES. You have been of great help during all the three years. I would like to specially thank Ms. Kojima, Ms. Nishiyama, and everyone else in this amazing and professional place.

I would also like to thank all the staff of Nonlinear Fluid Engineering Laboratory. Academic staff, technical staff specially; Mr. Masahiro Hamasaki, and administrative staff; Ms. Sakura Kawasaki, and Ms. Yukiko Matsuse, for all your kind help and support in all aspects during my 3 years PhD program.

A major role in the achievement of this thesis was due to the efforts of Prof. Roland Schmehl, and my colleague Sebastian Rapp of the Delft University of Technology (TU Delft). My three months internship in TU Delft was one of the main reasons I was able to complete my work and have a better understanding of the theory I used in accomplishing

this thesis, thank you a lot. Also, thanks to all the staff of TU Delft university for your kind welcoming in your community and helping me in the social life during my stay. Thanks to my friends Ammar Taher and Marwan for helping me during my staying in Netherlands.

My classmates of the 4th batch of the IEI PhD program, thank you for everything. We have been working together as a team specially in organizing the IEICES conference. You have been amazing friends and the best team I could ever work with. Thank you so much.

My dear friends Kamra, Ibrahim, Nassef, Ali, Islam, Egiza, Abdelrahman, Sameh, Youssef, Hatem, Omar, Tarek Attia, Tarek Amen, Ramadan, Sami, Jabir, and many more, thank you guys for all the awesome events we had. My life in Japan was made enjoyable by all of you.

Thanks to Future University in Egypt (FUE), for allowing me to travel and pursue the PhD degree. Thanks to the faculty and department board members. Specially Prof. Mohamed Badr and Prof. Yehia Hendawy. Also thank you to my colleagues and friends who have been supporting me overseas, specially Alaa, Eman, Magdy, Rana, Anas, Ahmed Adel, Amira, Abdelbarr, Essam, Aya, and many more. Also, my friends from the administrative staff Doaa and Mona.

Thanks to all my friends around the world from Aerospace department, Cairo University. Specially; Bork, Hassan, Ayyad, Shalaby, Khattab, Sadek. Your support and help was valuable.

My friend and mentor Dr. Ahmed A. Hussein, from Aerospace and Ocean Engineering, Viriginia Tech, you have been my tutor one day, and yet you have come to be a friend who has helped me a lot during my study whether in the undergraduate or the post graduate studies. You guided me to apply optimal control to my problem. Thank you so much.

My dearest friends, the companions of my journey; Tarek Dief, Amr Halawa, and

Amr Ismaiel. We have started this journey about 12 years ago since the undergraduate studies, and yet we continued together till we achieved the PhD. We have been together through ups and downs, through happiness and sorrow, and you have been always of great support to me when I feel down or insecure about my progress in study or any other aspect. No words can describe how grateful I am to you.

My brother and my role model since I was child, Dr. Ahmad A. Rushdi, from Sandia Labs, Albuquerque, USA. Your guidance and motivation to learn Machine Learning are unforgettable. I was able to achieve a great results to be published very fast.

Last but not least, my family, my source of power, who has sacrificed a lot so that I can achieve this degree. My parents, my brothers and sisters; they have supported me by all means, they have waited and have borne my absence for 3 years. However, they have been with me for all my steps despite the distance, they have taken care of me while I'm away, and I wish I can pay back your sacrifices after my return.

Mostafa Ali Rushdi

Kyushu University

March, 2021

Declaration

No portion of the work referred to in the thesis has been submitted in support of an application for another degree or qualification of this or any other university or other institute of learning.

Dedication

With all love and respect, I dedicate this work to **my father** and **my mother** whom without I wouldn't be a responsible person capable of learning and benefiting myself, and I wouldn't be able to achieve any of my dreams. **My wife** and beloved son **Omar**, their love and support was the main power during this journey.

Nomenclature

Latin Symbols

a_1, a_2 Numerator coefficients of the open-loop TF

AR Aspect ratio

b Wing span

b_1, b_2 Denominator coefficients of the open-loop TF

$\bar{c}$ Mean chord length

C_{i_j} with $i = [X, Y, Z, l, m, n]$ and $j = [\alpha, \beta, p, q, r, \delta_a, \delta_e, \delta_r, 0]$ denote the dimensionless aerodynamic derivatives

C_{R} Resultant aerodynamic coefficient

D Aerodynamic drag force

$\boldsymbol{F}_a^B$ Aerodynamic force vector in the body frame; contains $[F_x, F_y, F_z]$

F_{t} Tether tension force

F_T Thrust force

g Magnitude of the gravitational acceleration (intensity of the gravitational field)

$G(z)$	Open-loop TF of the Plackett's model
h	Hypothesis function
$\boldsymbol{I}$	Inertia matrix $\in R^{3\times3}$
L	Aerodynamic lift force
m	Mass
M_a^B	Aerodynamic moment vector in the body frame; contains $[L,M,N]$
n	Number of input features
r	Regularization factor
R^2	Coefficient of determination
S_w	Wing area
$\boldsymbol{u}$	Control action vector
$U(z)$	System input
v_a	Apparent wind speed at kite
v_w	Apparent wind speed at towing vehicle
$\mathbf{x}$	Input variables/features for the ML algorithm
$Y(z)$	Estimated value determined by the system identification in the z-domain
y	Measured output variable using sensor
$\hat{y}$	Predicted output variable of the ML algorithm (here: tether force)
Y_m	Measured data obtained from sensor

z^{-1} Backward shift operator in the z-domain

Greek Symbols

α Learning rate

β Elevation angle

δ_e Elevator deflection angle

θ Model's parameter vector containing the bias term θ_0 and the feature weights θ_1 to θ_n

ρ Air density

ϕ Azimuth angle

ω Angular velocity $\in R^{3\times1}$

Abbreviations

AOA Angle of Attack

AP Ampyx Power

AWE Airborne Wind Energy

CLL Control Line Length

DOE Design of Experiment

DOF Degree of Freedom

GPS Global Positioning System

HAWT Horizontal Axis Wind Turbine

HDI	Human Development Index
ICLOCS	Imperial College London Optimal Control Software
IMU	Inertial Measurment Unit
IPOPT	Interior-Point OPTimizer
KCU	Kite Control Unit
MAE	Mean Absolute Error
ML	Machine Learning
MSE	Mean Squared Error
NN	Neural Network
OED	Optimal Experimental Design
PCC	Pearson Correlation Coefficient
RC	Remote Control
SA	Sensitivity Analysis
SI	System Identification
TF	Transfer Function
TRL	Technology Readiness Level
UQ	Uncertainty Quantification
VTOL	Vertical Take-Off Landing

Contents

List of Figures

List of Tables

Chapter 1

Introduction

Contents

There is a prominent role played by engineering and engineers in probing, investigating, looking into, and shaping the future of mankind [20,21]. A future paradigm of engineering work is being created via the forces of sustainable development, the requirements of industrial ecology, the principles of ecological engineering, the principles of green engineering and the precautionary principle [22–24]. This work deals with an effective engineering solution to one of the most crucial, long-term and gravely-threatening problems facing mankind, namely, the energy problem.

1.1 Energy Crises

On our planet Earth, contemporary humans have adopted a high-consumption lifestyle that is not sustainable, leading to the depletion of natural resources, failing to maintain an ecological balance, destroying inter-generational equity, and transgressing the rights of future human generations to inherit a livable world. The energy problem is just one of the many extremely preeminent problems that humanity must tackle as soon as possible. This problem could be summarized in the following points:

Consumption

World energy demand is projected to grow by 1.3% p.a. from 2016 to 2040, thereby reaching 680 quadrillion British Thermal Units ($7.2 * 10^{17}$ joules) in 2040. All of this growth comes from emerging economies, and half of it comes from industrial uses, just over a third from residential/commercial buildings, and about a sixth from transportation. By the end of the century, the global consumption is expected to reach 1 ZJ (zettajoule $=10^{21}$ joules). The rate at which energy consumption is rising already exceeds the rate at which new fuel deposits are being discovered.

Climate Change

Fossil fuel (coal, oil, natural gas) combustion generates CO_2, which has been linked to global climate change, including global warming, sea level rise, more violent storms, and changes in rainfall rates. This will disrupt agriculture, disease control, and other human activities. Therefore, a substantial fraction of our energy must be generated without any CO_2 emissions within the next few decades.

Human Development Index (HDI)

Electricity consumption is closely positively correlated with quality of life (Figure 1.1). To improve the quality of life in under-developed or developing countries, it is vital to implement a tenfold increase in the energy consumption per capita, which is an undisputed right and an essential need for the citizens of these countries.

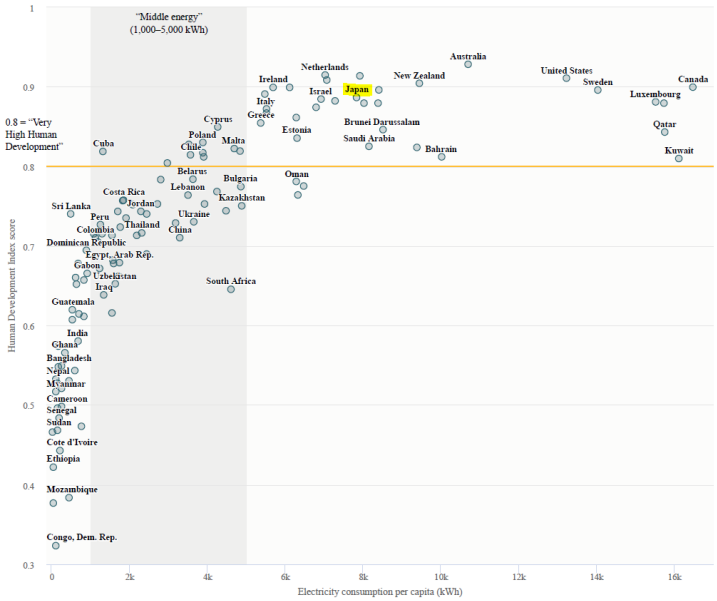

Figure 1.1: Human Development Index score versus electricity consumption (kWh) per capita for a variety of developed and developing countries [1].

1.2 Renewable Energy

Renewable energy is energy collected from resources, which are naturally replenished, and hence are not expected to be depleted on a human timescale. These resources include sunlight, wind, water falls, tides, sea waves, and geothermal heat. Humans are expected to die out (go extinct) long before they could see these resources run out. Reliance on renewable energy allows for a sustainable future of the human species.

Renewable energy has the distinctive advantages that, in comparison with traditional energy, its facilities generally require less maintenance, and its 'fuels' are naturally available at almost no cost. As an offshoot, it produces little or no waste products such as carbon dioxide or other chemical pollutants, so it has minimal detrimental impact on the environment. For all these reasons, the world interest in renewable was increased through the last decade. According to the Renewables 2019 global status report (REN21), the usage of renewable energy increased by 20% over the past decade. The renewable share jumped from 45% in 2008 to 65% in 2018 against the non-renewable share. This is an indication of the increasing rate of the renewable energy addition share in the net annual additions of power generating capacity. The total renewable energy added in 2018 was 181 Gigawatts, as shown in Figure 1.2.

By having a detailed look to this increase, it could be found that the major part is due to the solar power addition, as shown in Figure 1.2. It could be noticed that over the years 2012 to 2018, the hydropower and wind power additions are fluctuating, on the other side the solar power additions are increasing with an ascending rate, while the rest of the renewable energy types additions are almost constant. The share of the renewable energy in global power capacity grew to over 33% in 2018. According to all this information, wind energy is playing an important role in renewable energy technologies. However, more power is still needed, and that's why a new method of harvesting energy from wind will be represented later.

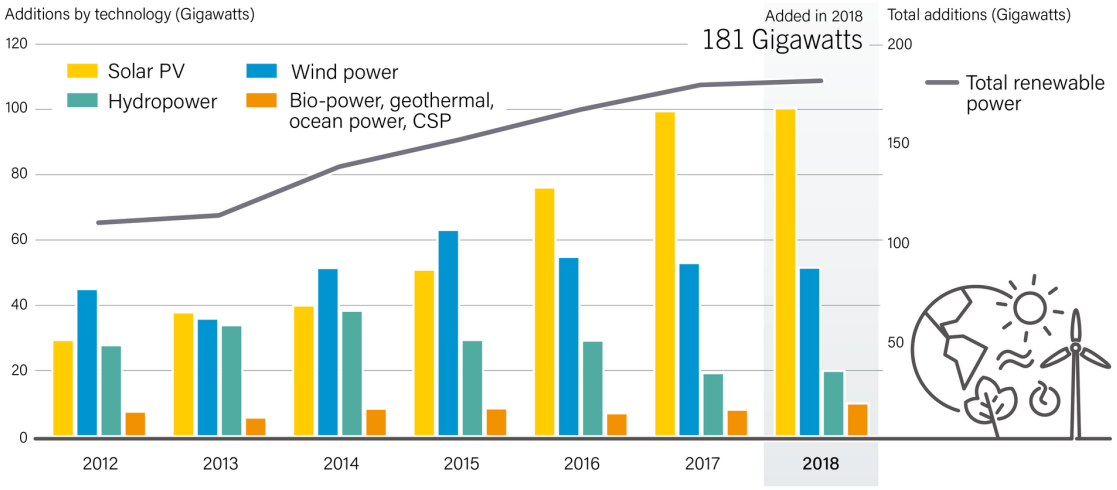

Figure 1.2: Annual additions of renewable power capacity, 2012-2018 [2].

In the latest data represented in the Renewables 2019 global status report (REN21), the renewable energy share of the global electricity production was 26.2%, as shown in Figure 1.3.

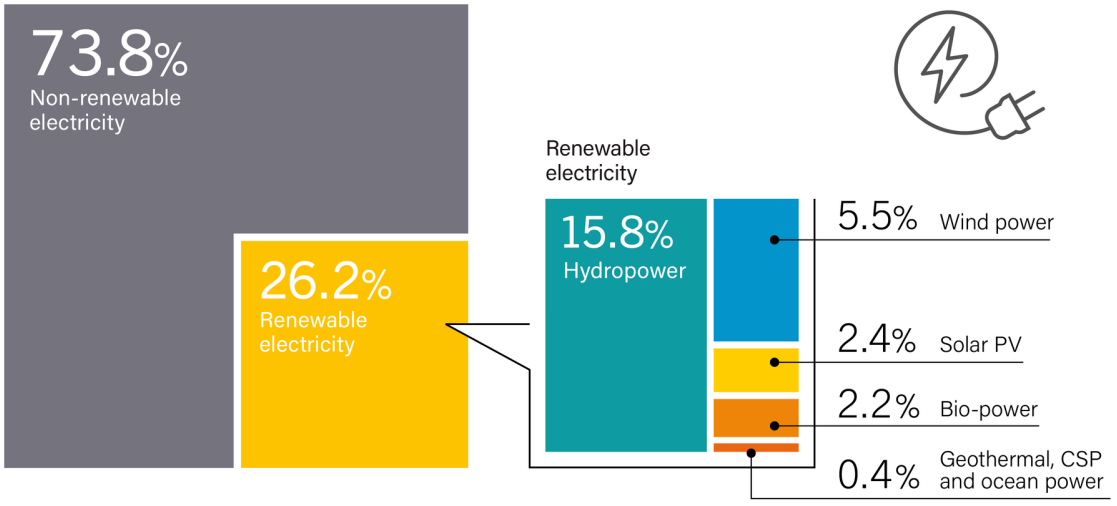

Figure 1.3: Renewable energy share of global electricity production, end of 2018 [2].

The global investment, among the renewable energy types indicates the dominance of solar and wind powers, as shown in Figure 1.4.

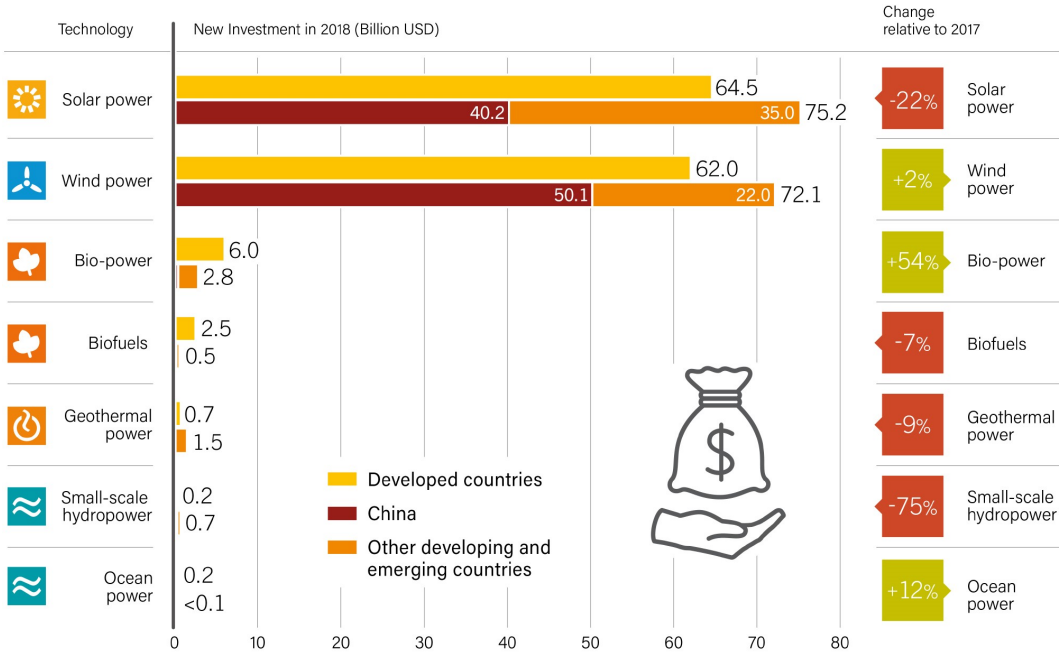

Figure 1.4: Global new investment in renewable energy, 2018 [2].

1.3 Wind Energy

1.3.1 History

Humans used wind energy since early recorded history. Ancient Egyptians harnessed the energy of the wind, propelling boats along the River Nile as early as 5000 B.C. By the 11th century, people in the Middle East used windmills extensively for pounding and grinding grains, two of the heaviest tasks humans have ever undertaken. The Dutch refined the windmill and adapted it for draining lakes and marshes in the delta of the River Rhine, and to pump water for farms and ranches and later to generate electricity for homes and industry. Throughout the 20th century, wind power was utilized in producing electricity to light buildings. The same century witnessed the development of small wind plants, suitable for farms and residencies, and larger utility-scale wind farms that could be connected to electricity grids.

1.3.2 Statistics

As showed previously before in Figure 1.3, the share of the wind energy in the global electricity production is 5.5% at the end of 2018. This may be considered a little contribution, but by having a look on the past few years, it could be found that the total installations (onshore and offshore) is increased with a high rate, as shown in Figure 1.5. Also, the investments in the wind energy is increasing, compared to the closer comparator, which is solar energy that have a big decrease in the amount of investment, with -22% relative to 2017, as shown in Figure 1.4.

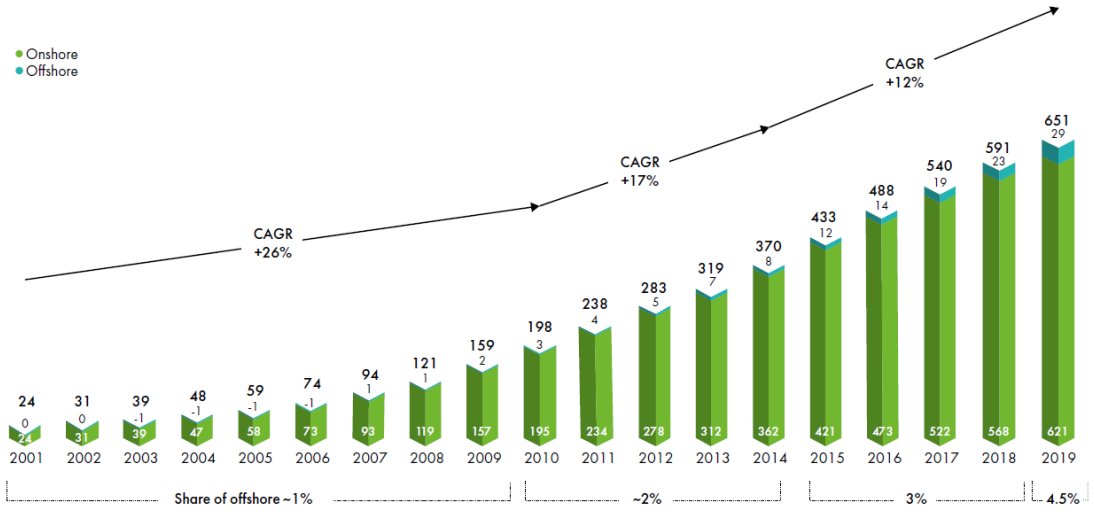

Figure 1.5: Historic development of total installations (onshore and offshore), 2001-2019 [3].

1.3.3 Growth of wind turbines

Throughout the years, it was observed that increasing the height means more density for the energy harvested (see Figure 1.6), which needs more structures and materials for the tower based systems.

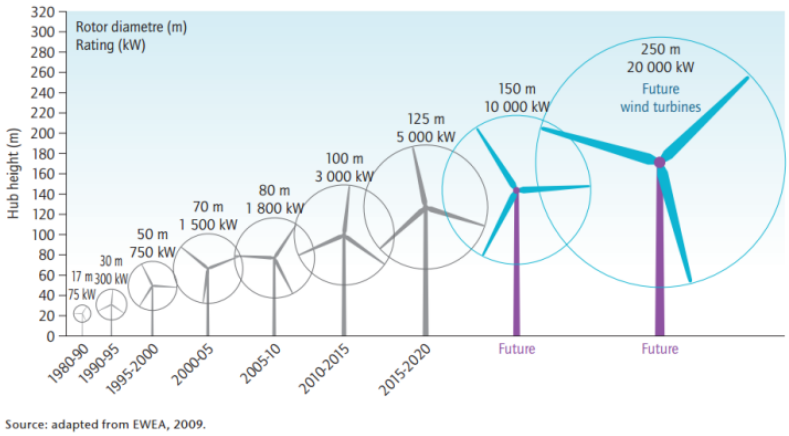

Figure 1.6: WT growth over the past four decades (with future predictions) [4].

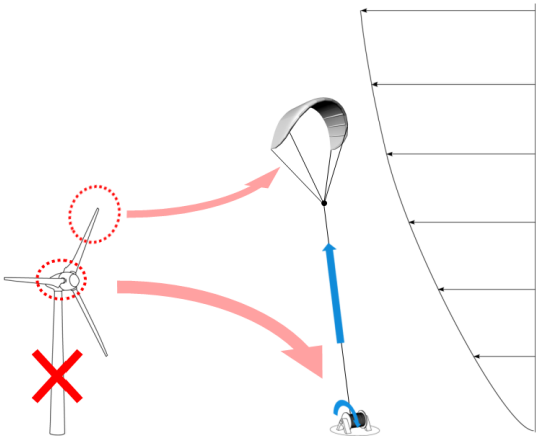

Figure 1.7: AWE concept [5].

1.4 Airborne Wind Energy

From the aforementioned observation, the airborne wind energy (AWE) concept was conceived and established, as shown in Figure 1.7, by reaching higher altitudes with simpler amount of materials. For more energy harvesting, it could be summarized that the aim is (a) higher energy density at higher altitude, (b) less materials, and all these points lead to AWE concept establishment.

1.4.1 Concept

The main principle of AWE is that the flying device generates aerodynamic forces, which are transferred as tension in the tether, effectively as mechanical energy, that could be converted to electrical energy at the ground station via a drum and a generator, as shown in Figure 1.8. The power is generated during the reel-out phase, and there is some power consumption during the reel-in phase.

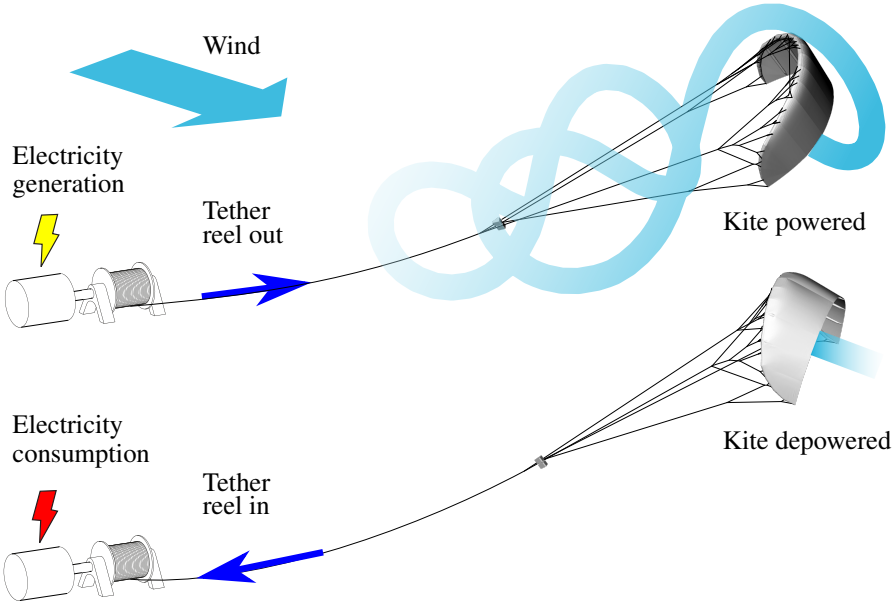

Figure 1.8: Working principle of the pumping kite power system [6].

1.4.2 History

Airborne wind energy (AWE) is an emerging renewable energy technology, which utilizes flying devices for harnessing wind energy at higher altitudes than conventional wind turbines [25–29]. Although the fundamental working principles of the technology were already formulated in the 1980s by Miles L. Loyd [30], the systematic and networked exploration of the technology did not start until the beginning of 21st century. One of the pioneering teams was led by Wubbo J. Ockels at Delft University of

Technology (TU Delft), initially proposing the visionary "Laddermill" concept [31], but eventually resorting to a pumping kite power system using a single flexible membrane wing connected to a ground station [32]. Over the last decade, AWE has evolved into a rapidly growing field of activity encompassing a global community of researchers, investors and developers. The investment in this topic is motivated by the desire to find a cost-effective renewable energy technology that can contribute substantially to reducing the dependency on fossil fuels [25, 26, 28, 29]. Floating offshore locations are considered to be particularly suitable for large-scale deployment of AWE systems [33]. The current community of AWE is very huge, as shown in Figure 1.9, with the presence of Kyushu University because of our project.

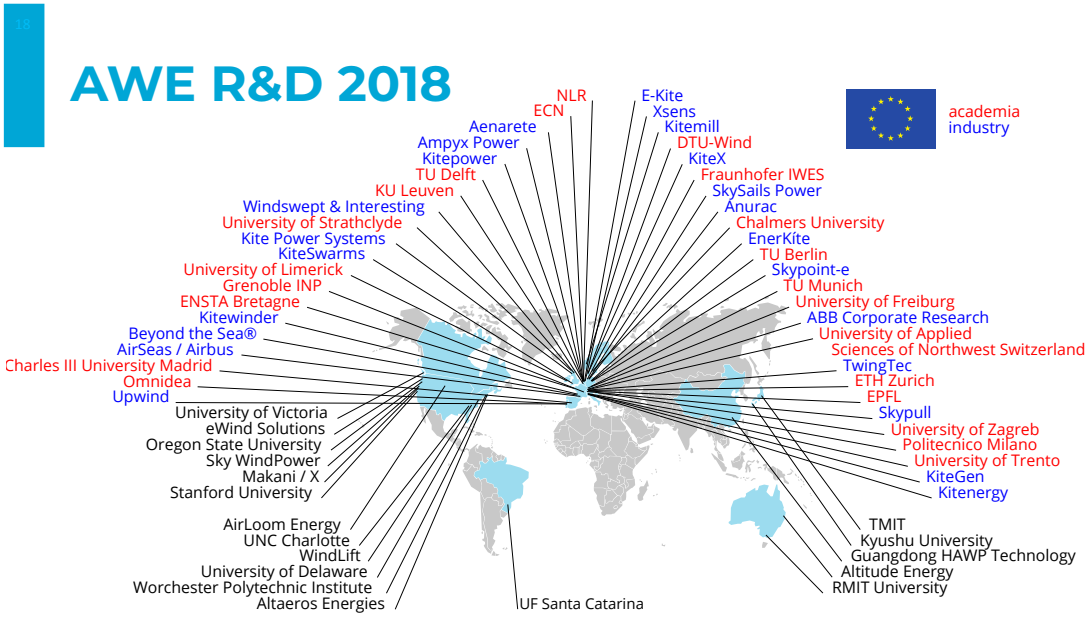

Figure 1.9: AWE R&D organizations in 2018 [7].

1.4.3 Types and classification

There is a lot of AWE types and several ways to classify these type. It could be classified based on the generator location, as in Figure 1.10, for three categories.

- On board generator, as in Magenn power, is not practical because the flying device should contain a lot of helium to be able to fly the generator. This leads to a huge vehicle with high drag.

- On ground generator, as in Ampyx Power, is simple, cheap and easy for maintenance.

- Double mission motor, as in Makani, is very expensive and hard to control because of its large scale. However, it proves its ability to produce a 600 kW, which makes it the leading prototype within the AWE community.

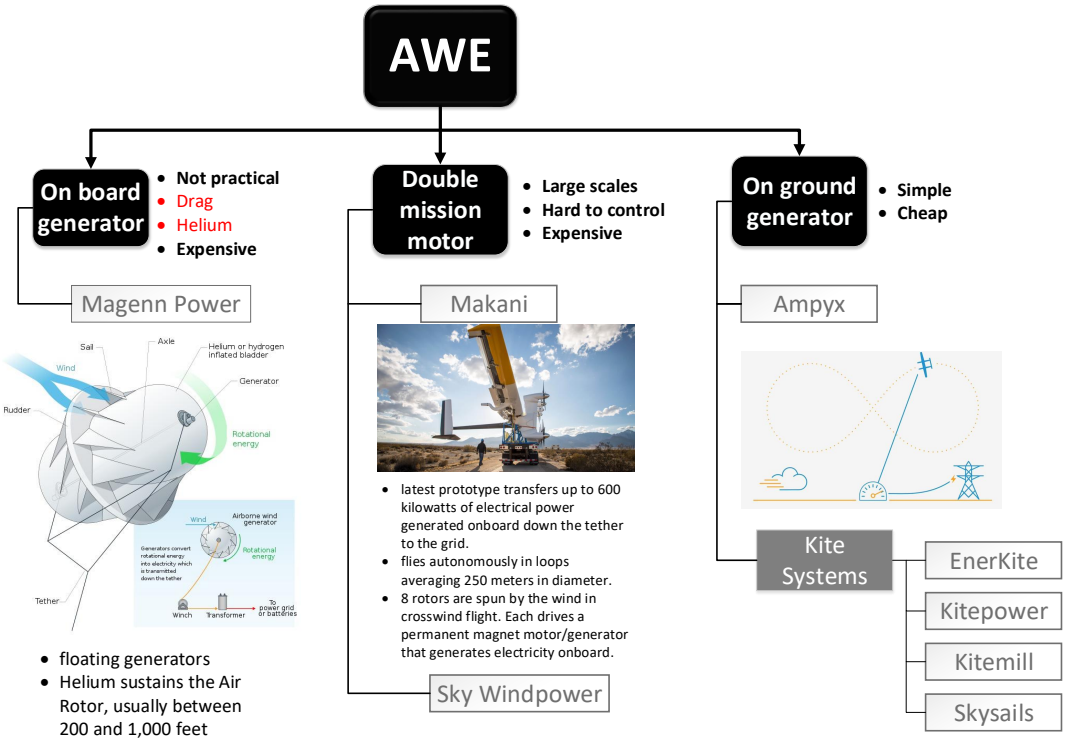

Figure 1.10: Classification of AWE types

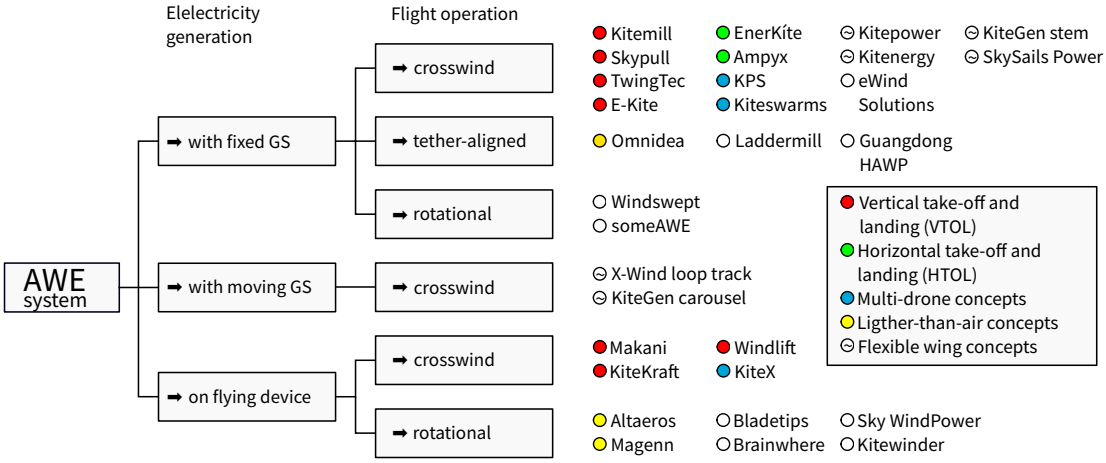

Figure 1.11: Detailed classification of AWE types [7].

Also, it could be classified based on the flight operation or the launching type, etc, as proposed by AWESCO, shown in Figure 1.11.

- The *power generation* is on board or fixed on the ground.
- The *flight operation* is crosswind or rotational or tether-aligned.
- The *flying vehicle type* is rigid aircraft or flexible kite or lighter-than-air-vehicle.
- The *launching mechanism* for the rigid aircrafts it will be VTOL or HTOL, for the flexible kites it will using mast configuration (shown in Figures 1.13 and 5.1) or multi-drones.

Although a number of different harvesting concepts have been explored, the most pursued type of concept is that of a flying device that performs fast crosswind maneuvers and transfers the generated pulling force via a tether to a ground station [7]. At the ground station the tether is reeled off a drum-generator module to convert the pulling force into electrical energy. When reaching the maximal tether length, the flight pattern of the device is changed and the tether is reeled back in, which consumes a small fraction of the previously generated energy. The working principle of such a pumping

AWE system is illustrated in Figure 1.12, for the example of the 20 kW technology demonstrator of TU Delft [6].

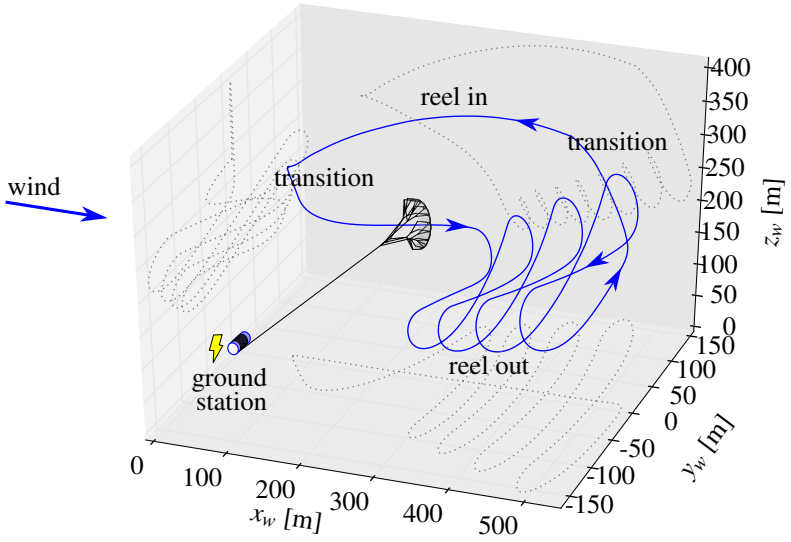

Figure 1.12: Computed flight path of a kite power system using a flexible wing with suspended kite control unit and single tether (kite & drum not to scale) [8].

Nowadays, many companies are developing AWE systems with flexible membrane kites: KitEnergy [34], KiteGen [14], SkySails Power [15], and Kitepower [35]. Among these the highest technology readiness level (TRL) has been reached by the company Kitepower which commercially develops a 100 KW system with a kite of 60 m^2 wing surface area.

As will be shown in the next chapter, Kyushu University project is similar to Kitepower, the electricity generation is done with fixed ground station, the flight operation is cross-wind, and the flying device is based on flexible wing concept.

1.4.4 Comparison with HAWT

So far, AWE has been demonstrated only on a level of several hundred kilowatts, i.e. one magnitude lower than what would be commercially viable for the utility sector [25, 26]. However, AWE systems have several promising advantages compared to the horizontal

axis wind turbines (HAWTs), for example, substantially less material use for both tower structure and foundations as well as lower costs for transportation, installations, and maintenance. Conventional wind turbines use the tower and foundation to transfer the load of the rotor to the ground. AWE systems use one or more tethers to transfer forces of a similar magnitude. The design as tensile structure substantially reduces the material use, which leads to lower system costs and environmental footprint. It also allows a dynamic adjustment of the operational altitude to the available wind resources, which can greatly increase the capacity factor [36]. For a HAWT, almost 30% of the power is generated by the tip of the rotor blades while the rest of the rotor functions mainly as a support structure for the crosswind motion of the blades [25, 26]. The rated power of the generator typically determines the installation. For the same rated power, an AWE system generally gives a higher annual yield than a HAWT because it can operate at a higher capacity factor. The higher capacity factor is a result of the more persistent and more steady wind at higher altitudes. However, an AWE system also needs more space than a HAWT, which increases the costs of an installation. These land surface costs are still quite unknown and responsible for the large differences in expected costs [26].

The prominent reasons for the particular use of AWE in electricity production could be summarized in the next points and in Table 1.1.

- AWE systems reach winds blowing at higher-altitude atmospheric layers that are inaccessible by traditional wind turbines. These winds are typically stronger and more constant than those closer to the ground (Figure 1.7).

- The area that can be swept by an AWE system is not tightly limited, unlike that of a turbine which is limited by its diameter, and hence an AWE system is inherently more efficient.

- AWE systems are expected to need less material investment per unit of usable power than most other renewable energy sources.

Table 1.1: Kite systems vs wind turbines [19].

	Kite Systems	**Wind Turbines**
System items	simple	complex
Cost	5-10% of WT	100 %
Maintenance	replacement	more time
Safety	less safe	safe
Maximum altitude	200-1000 m	180 m
Capacity power(weight)	100 kW (40-70 kg)	5 MW (600 t)

1.4.5 Kite power system components

The components of the airborne wind energy, specifically the kite power system (KPS), are presented in Figure 1.13. The main components are a **flying device**, which is the kite, to generate aerodynamic forces. The kite is connected to the ground using a **traction tether**, in which the aerodynamic forces of the wing are transferred as a tension force (mechanical energy). The tether is connected at the ground to a **drum/generator module**, in which the mechanical energy is converted to electrical energy. To control the movement of the kite within a prescribed path, a **kite control unit (KCU)** should be connected between the bridal/control lines and the traction tether. In the case of autonomous flight, there must be some **communication system** between the KCU and the ground, to adapt the reel in and reel out phases. Also, it should be some **sensors** available to adapt the control action autonomously. For the phase of launching, it is possible to have a special **launching mechanism**, mast mechanism for example.

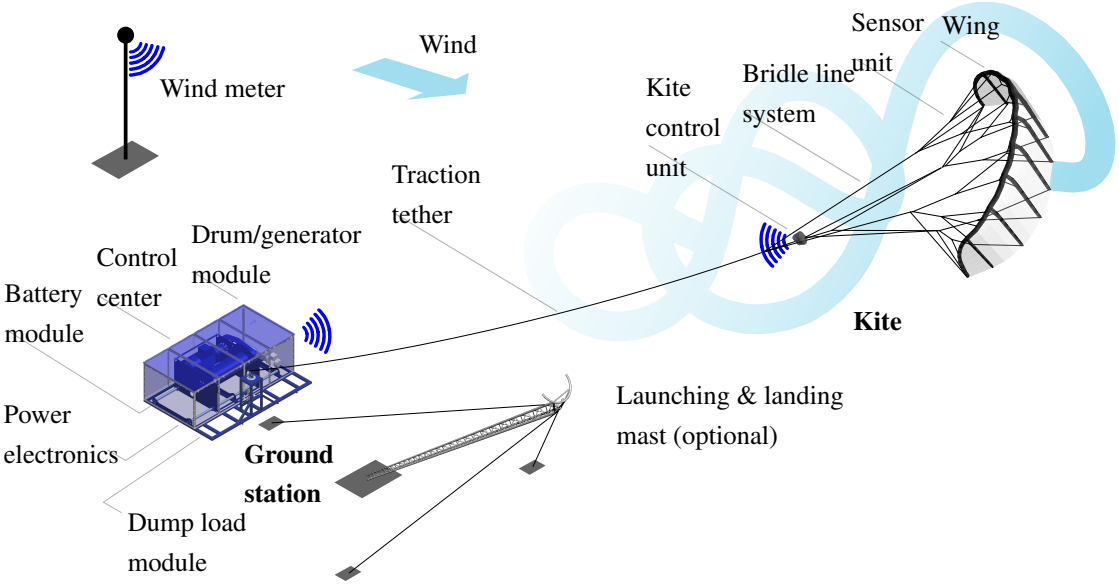

Figure 1.13: Airborne wind energy system components [9]

1.5 Objectives

The objective of this project is to develop a kite system prototype. The work started be the development of the main components like kite control unit, measurement unit, and generator (under development). The autonomous flight is aimed to, as an important target for the project, and it is still under developing. For the sake of validation, it is aimed to model and simulate a numerical model and compare it with the experimental results, this is still in progress.

The objective of this thesis is to perform experiments as a proof of concept of the current kite power system prototype. After that, analyzing the collected data from the experiments. Studying the kite behavior, using a system identification technique, is a preliminary step for the autonomous flight. The sensitivity analysis plays an important role in understanding the whole system and which features are valuable and affects the resulting power. The power prediction, using machine learning models, is essen-

tial to know the resulting power without performing flight tests or experiments. Also, introducing the optimal trajectory of a VTOL aircraft during a transition phase, based on minimizing power, is important in case of the soft kite was changed wing to avoid lunching problems.

1.6 Thesis Organization

Thesis organization are represented in a very simple way in Figure 1.14. The aim of this thesis is to introduce a new technology of harvesting energy from wind, which is airborne wind energy systems. The work done in this thesis could be divided into three parts; modeling& control, project & experimental work and data analysis using system identification (SI) & machine learning (ML).

In the first part, a tether-kite system using lumped mass model was modeled, but this part will not be included in the thesis. Due to launching problems for soft kites, the solution of rigid aircraft modeling was presented in Chapter 5 and a detailed optimal control of the transition phase was illustrated.

In the remaining two parts, Kyushu University kite project and experiments were introduced in Chapter 2. Then by taking benefit from the collected data of the early flight tests, it was able to identify the kite behavior using system identification in Chapter 3. After that, in Chapter 4, by enhancing the collected data and adding more features, it was able to train a machine leaning algorithm for power prediction, and this was the first attempt in AWE community to apply ML algorithms in AWE technology. Finally, Chapter 6 concluded the thesis.

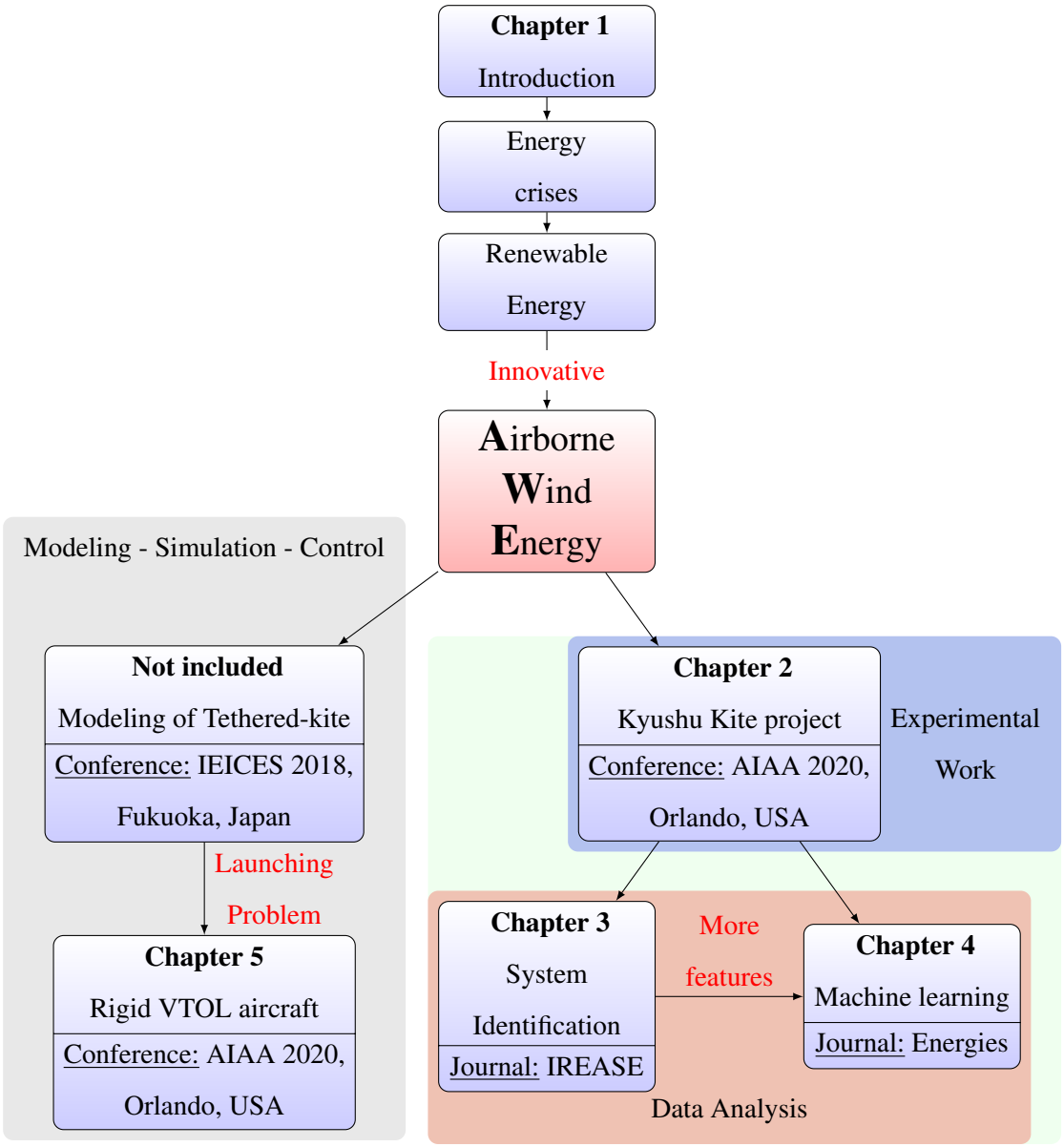

Figure 1.14: Thesis road map with published papers

Chapter 2

7 kW Class Pumping Kite Power System Project

Contents

In the current work, the concern will be with the flexible membrane kites because they are cheaper, require low maintenance costs, and are safer. For the sake of maximizing the power production of the kite, it is operated in crosswind maneuvers during tether's reeling out [30]. By using a constant length tether and attach it to a towing vehicle, a controlled relative flow environment was produced. Notice that there is no actual drum/generator module at the current stage. The typical system components of such an AWE system are shown in Figure 1.13, which represent specifically the 20 kW technology demonstrator of Delft University of Technology.

In this chapter, a KPS developed at Kyushu University is described. The system components are stated below. After that, the experiment setup is used to collect data using this system is represented. It followed by, the a representation of the measured data; specially the measured tension, which is an indication of the power generation.

2.1 System Components

The main components of Kyushu University 7 kW KPS stated below.

2.1.1 Kite

UNO V2, 6 m^2 inflatable kite, manufactured by OZONE company originally for kite surfing, is used as the flying device of the system.

Figure 2.1: The 6 m^2 inflatable kite used in the 7 kW system [10].

2.1.2 Tether

The tether is made of the ultra-high molecular weight polyethylen called "Dyneema®" [37], which is a light-weight ultra-strong fiber, which can withstand a maximum tension force of 2500 N.

2.1.3 Kite control unit

From its name, this is the robot machine which is responsible for controlling the kite movement. Figure 2.2 represents the design and the functional components of the KCU while Figure 2.3 represents the schematic illustration of the design, also a detailed information of the design is available in Appendix B. The total mass of the KCU, taking the battery in the account, is three kilograms. The location of the KCU is about 13 m below the kite. The KCU's main part is a servo motor, which is responsible of the actuating the control lines which leads to steering the kite to the desired specific path. The KCU receives the control action demand for the servo motor wirelessly from the radio control (RC). The KCU is connected to a tension meter to measure the generated pulling force during testing. The KCU is powered by a lithium battery which could sustain almost three hours of continuous operation.

The employed bridle layout is common for small surf kites and supports the leading edge tube at four points, while the rear ends of the kite tips are connected to the control lines. The kite is steered by asymmetric control input, shortening one control line, while

feeding out the other line. Such control input leads mainly to a deformation of the kite by spanwise twisting, because the front bridle largely constrains a roll motion of the kite when the power line and the control lines are tensioned. The kite twist and the modulated aerodynamic load on the kite tips induce a yaw moment by which the kite is steered into a turn [38, 39]. There is no direct control on the angle of attack of the kite, however, the length of the control lines could be varied in advance, to change the AOA.

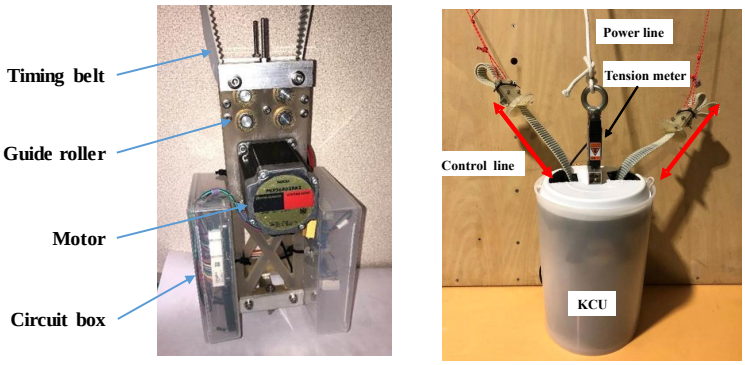

(a) (b)

Figure 2.2: Photos of the design of the KCU, including structural frame, transmission belts, electronic circuit, and motors. (a) the core of the KCU without casing and (b) after putting the casing.

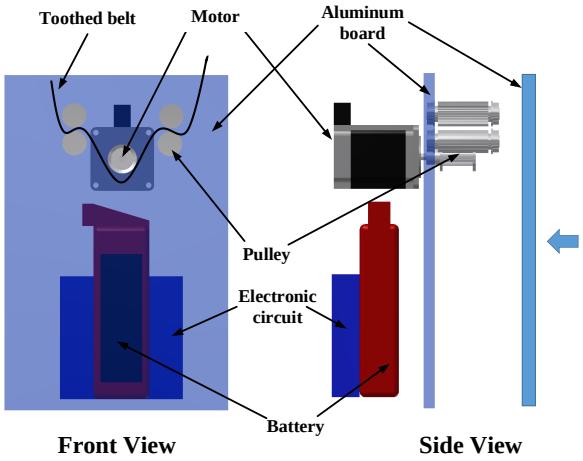

Figure 2.3: Schematic front and side views of the KCU [11].

2.1.4 Measurement unit

For the sake of measuring the kite's position, height and attitude, a small measurement unit was mounted on the connection of leading edge and center strut of the kite, as shown in Figure 2.4. To measure the aforementioned data, a global positioning system (GPS), a pressure sensor, an inertial measurement unit (IMU) were used, respectively. An Arduino® microcontroller was used to handle the connection between sensors. XBEE® was used to sent this data wirelessly to the ground station with a sampling time of 0.15 s.

(a) (b)

Figure 2.4: (a) Measurement unit and (b) attachment on the leading edge of the kite.

2.1.5 Ground station

The generator, which is the main part of the ground station for KPS, is still under development. Till now, the ground equipment is comprised of the wireless unite receiver, a speed sensor and tension meter.

2.2 Experiment Setup

In Kyushu University, a small kite system prototype was designed for 7 kW traction power. This system is similar to the airborne kite component depicted in Figure 1.13, as it contains a 6 m^2 inflatable wing and a suspended remote-controlled KCU. Early flight tests were performed with the KCU anchored at the ground at Nata Beach, Fukuoka, Japan, as shown in Figure 2.5(a). During these tests, the wind speed was between 6 and 10 m/s. The kite was launched manually from the side of the wind window (imagine the kite is placed in a certain location and there is a window in which the wind goes through it towards the kite) at which the pulling force is relatively low as a safety reason. Then the kite was operated by a human pilot to perform a figure-of-eight maneuvers, by the use of the remote control (RC) and KCU. The aim of this test was to check that the KCU is functioning in a good way.

(a) (b)

Figure 2.5: Flight tests with (a) stationary KCU anchored at the ground, and (b) towed KCU flying on a short tether.

The wind speed at the kite was hard to be measured, during the early flight tests. In addition to facing the problem of having low wind speed frequently. Because of these reasons, the test strategy was adapted to a truck towing test setup, by connecting the KCU to a truck using a tether, as shown in Figure 2.5(b). This kind of tests were performed on weak wind days to avoid the contribution of the generated relative air flow. Under these circumstances, the apparent wind speed at the kite is considered

approximately equal to the truck speed, so it could be said that this gave us another DOF to be controlled. The location of performing these tests was a small air field for unmanned aerial vehicles at Shiroshi, Saga, Japan, with a run way of 750 m, depicted in Figure 2.6. The aim was to check the resultant tension when the flight maneuver and towing speed changed [40].

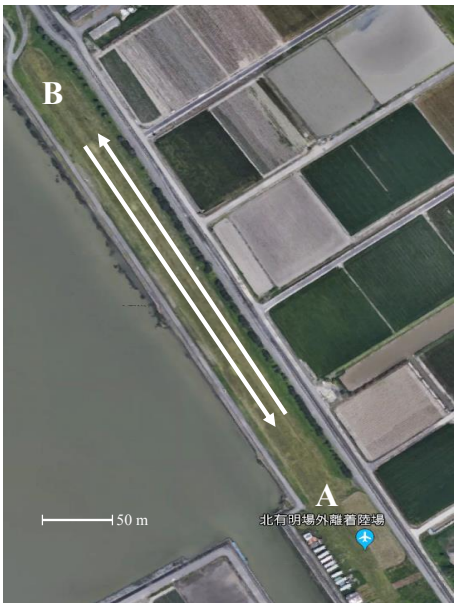

Figure 2.6: Google map photo of the run way used for the tow tests, Landing Field at Shiroshi, Saga, Japan.

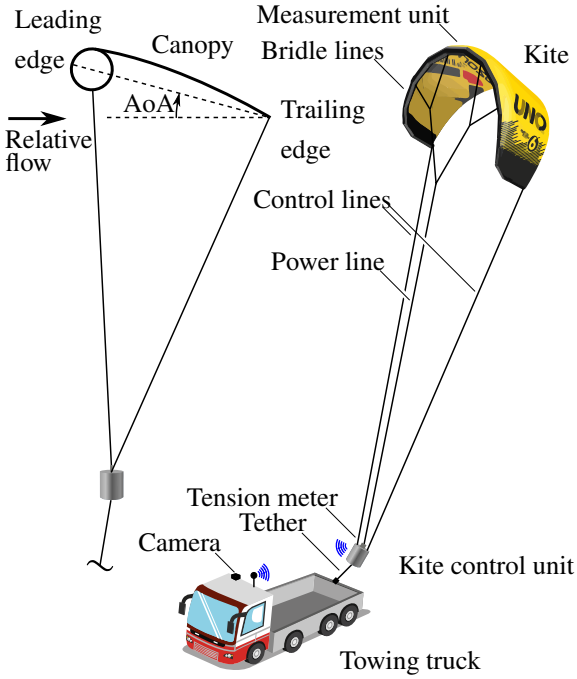

Figure 2.7: Schematic illustration of the truck towing test setup: side view with AOA definition (left) and 3D view (right).

Figure 2.7[1] represents a schematic illustration of the truck towing test setup and shows the details of how the kite is connected to the KCU. This connection is based on 3 separate lines. The first line is called the power line and it is connected to the leading edge of the wing via several bridle lines. The remaining two lines are called power lines and they are connected to the wing tips at the trailing edge. In the current experiment, the power line length was kept constant to 13.3 m (measured from the KCU to the end

[1]Truck image: Freepik.com

of the first fork). Using control lines of three different lengths, 13.4, 13.6 and 13.8 m, by which it was possible to adjust the angle of attack of the kite. The connection of the KCU to the truck deck was done using a shorter tether of a constant length equal to 0.4 m. In the actual power production setup, as in Figure 1.13, the length of this tether should be longer, to make the kite capable of sweeping a larger volume and reaching higher altitudes [6]. A tension meter attached to the KCU was used to measure the pulling force of the kite.

2.3 Experimental Results

2.3.1 Fixed KCU test

The results of the fixed KCU test are presented at Figure 2.8. When operating the kite with figure-of-eight motion the average tension was 350 N and reduced to an average of 100 N when the kite is stationary/steady flight.

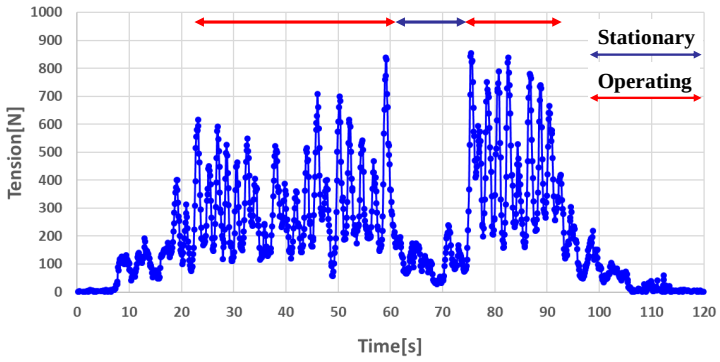

Figure 2.8: Measured tension using tension meter, in case of fixed KCU test [12].

2.3.2 Truck towing test

Using the truck affords controlling the apparent speed of the kite and checking the resultant tension when the flight maneuver and towing speed changed.

(1) Test 1: Steady flight with truck speed 40 km/h

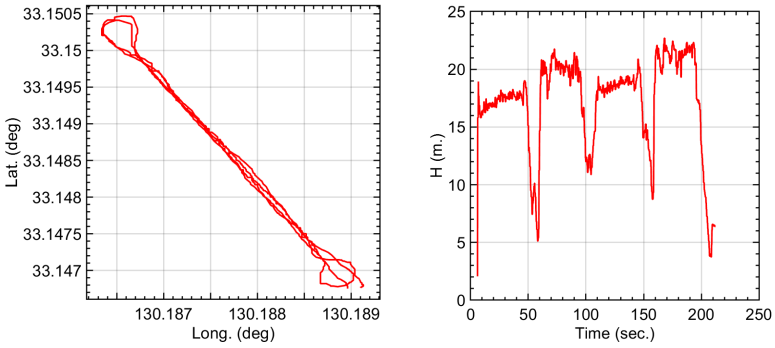

(a) Longitude-Latitude (b) Hight

Figure 2.9: Kite position for Test 1.

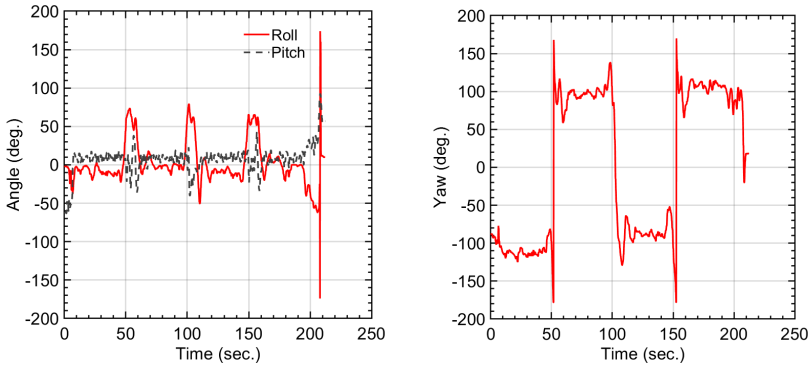

(a) Roll & Pitch angles (b) Yaw angle

Figure 2.10: Kite orientation for Test 1.

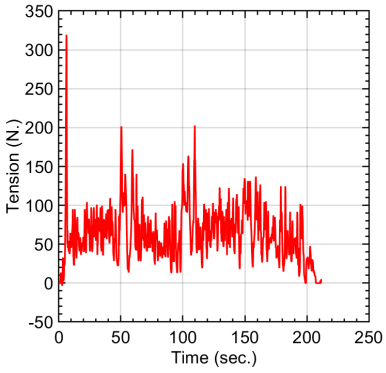

Figure 2.11: Measured tension force for Test 1.

In Test 1, the truck was moving in a fixed speed, 40 km/h, to perform a steady flight as shown in Figures 2.9a, 2.10 , and 2.11. The truck was moving in a certain path, straight lines to pass the points (A-B-A-B-A) respectively to complete two cycles, as shown in Figure 2.6. The static wind speed on the ground was 1-2 m/s measured by wind speedometer, and the day of test was chosen carefully to mitigate the impact of wind on the test results so that it is assumed the relative wind speed affecting the kite during flying is almost the same as truck speed.

The kite was flying in a steady flight; the roll and pitch angles maintain almost constants over the two cycles. Also, the kite flew in the same altitude during achieving the two cycles with slight ups and downs. In Figure 2.10a, the average roll angle was almost constant, -10°, and the pitch angle was around 5°. Also, the height of the kite was 15 m. However, in turning phases, the kite changes its direction 180° every 50 s, as indicated in Figure 2.10b. Therefore, this change in direction causes a dramatic variation for the roll and pitch data unlike the steady condition during moving between points A and B. Moreover, the kite loses its height because the truck speed is reduced to 20 km/h, so that the height becomes $5-17$ m as shown in Figure 2.9b.

The tension force obtained from the kite was measured over the two cycles, and it changes based on the kite motion. As indicated in Figure 2.11, the tension values are fluctuating around 50 N at the steady flight, however, during turning, the relative wind speed increases so that the lifting forces jump to be two times its normal value at the steady condition.

The landing occurred at the time 200 s as shown in Figure 2.9b. As a result, the tension force declined sharply to zero, Figure 2.11. The readings of attitude were abnormal as the kite rotates during touching the ground as shown in Figure 2.10a.

(2) Test 2: Figure-of-eight flight with truck speed 40 km/h

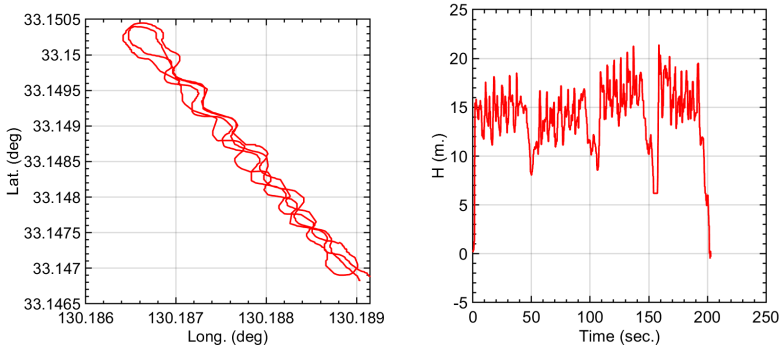

(a) Longititude-Latitude (b) Hight

Figure 2.12: Kite position for Test 2.

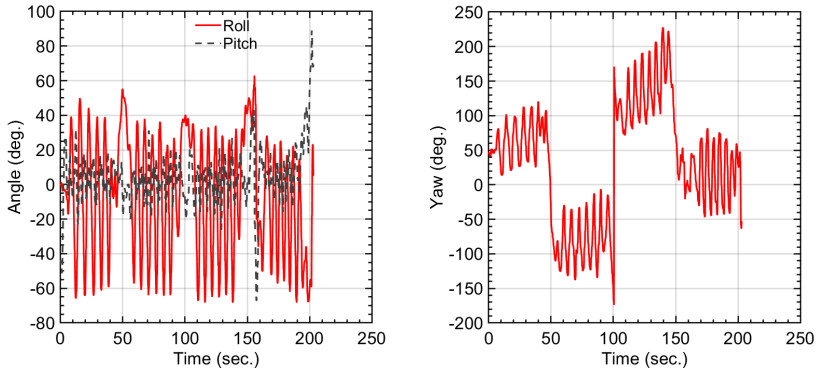

(a) Roll & Pitch angles (b) Yaw angle

Figure 2.13: Kite orientation for Test 2.

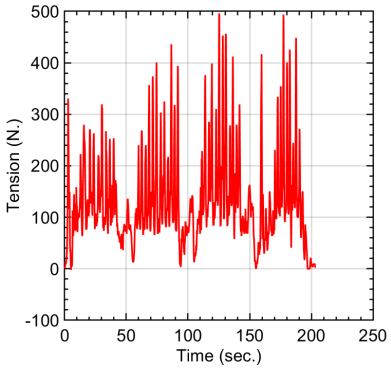

Figure 2.14: Measured tension force for Test 2.

In Test 2, the truck was moving with a fixed speed, 40 km/h, and the motion path of the truck was through the points (A-B-A-B-A) to achieve two complete cycles, as shown in Figure 2.6. Unlike Test 1 (2.3.2 (1)), the kite was forced to do maneuvers as shown in Figure 2.12a, 2.13 and 2.17. During moving between the points A and B, the kite was rolling within range of $\pm 60^{\circ}$ due to the control exerted on the kite. The pitch angle, shown in Figure 2.13a, was almost constant with small fluctuations. The kite takes 50 s to move between the two points A, B and vice-versa. The two complete cycles took around 200 s. After reaching any point of A or B, the kite has to turn, then move in a straight path again. During turning, the yawing values are changing 180° as shown in Figure 2.13b. Then it starts fluctuating again because of the maneuvers occur, between A to B.

The height of the kite also changes due to the maneuvers ± 4 m from its normal height every 50 s. The kite loses its altitude due to the turn, then climb again to its normal height with slight fluctuations as shown in Figure 2.12b. The average tension forces produced from the kite increases, as expected, because the relative wind speed affecting the kite is higher, as a result, the lifting forces increase as shown in Figure 2.14. The average tension force is 100 N, also, sometimes, it reaches to 300 N due to the maneuvers.

During landing, at the time 200 s, the tension force values decline to zero and the kite loses its height, also the data of attitude will change dramatically as it lands on the ground.

(3) Test 3: Steady flight with truck speed 50 km/h

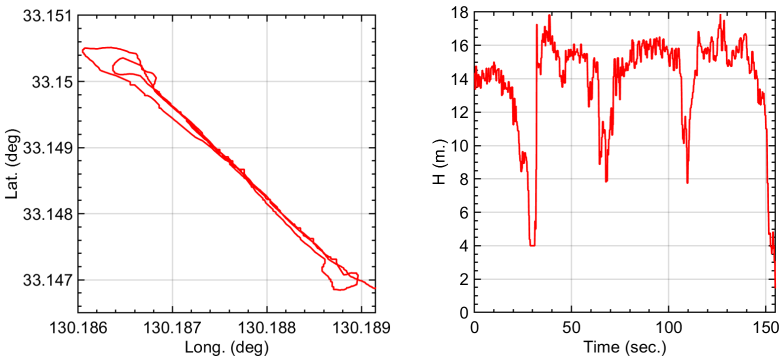

(a) Longititude-Latitude (b) Hight

Figure 2.15: Kite position for Test 3.

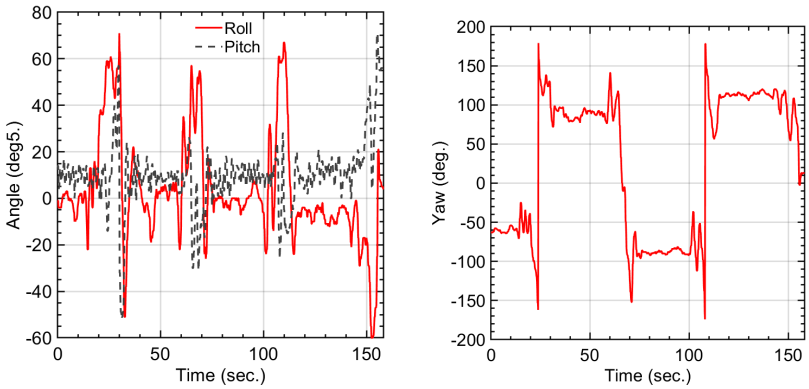

(a) Roll & Pitch angles (b) Yaw angle

Figure 2.16: Kite orientation for Test 3.

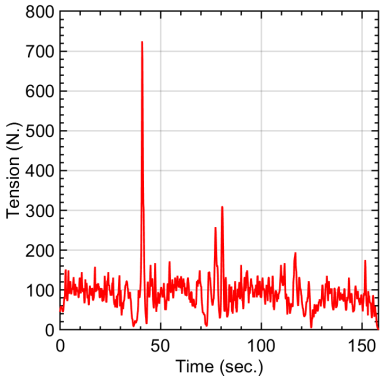

Figure 2.17: Measured tension force for Test 3.

Test 3 is aiming to perform a steady flight, the same as Test 1 (2.3.2 (1)), but with higher truck speed. The truck speed was 50 km/h, without any maneuvers as depicted in Figures 2.15a, 2.16 and 2.17.

The test started from point A towards point B, and the kite was forced to move in a straight line as shown in Figure 2.15a. Due to this motion, the values of roll and pitch angles were almost constant with slight ups and downs as shown in Figure 2.16a, they were about 0° and 10° respectively. The yaw angle and kite's height maintained almost constant till the reaching to the turn phases with -50° and 15 m in row, see Figures 2.16b and 2.15b. The time consumed to perform the motion from point A to B is less than Test 1 (2.3.2 (1)), as the truck speed is faster. It's clear from the results of Test 3 that, the total time to finish two complete cycles is 150 s compared with 200 s in the previous two tests.

The kite performed its first turn at the time 30 s as shown in Figure 2.16b, and the kite changes its direction 180° at turning. Moreover, the kite loses its height to gain more relative wind speed. After that, the kite repeat the same motion but from point B to A with the same performance.

The tension force of the kite was almost constant with average value 100 N during the whole test, except the turning phases as indicated in Figure 2.17. It had the highest peak at the time 40 s, as the kite loses its height and as a result the relative wind speed becomes high. It was found that the average tension force obtained from this test is two times the force comes from the same test with lower truck speed, Test 1 (2.3.2). It means, increasing the truck speed just 10 km/h, from 40 km/h to 50 km/h, can double the force obtained from the same kite in the same steady flight.

(4) Test 4: Figure-of-eight flight with truck speed 50 km/h

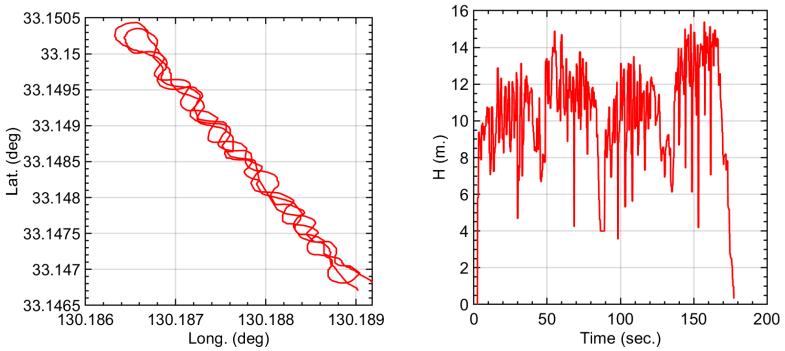

(a) Longitude-Latitude (b) Hight

Figure 2.18: Kite position for Test 4.

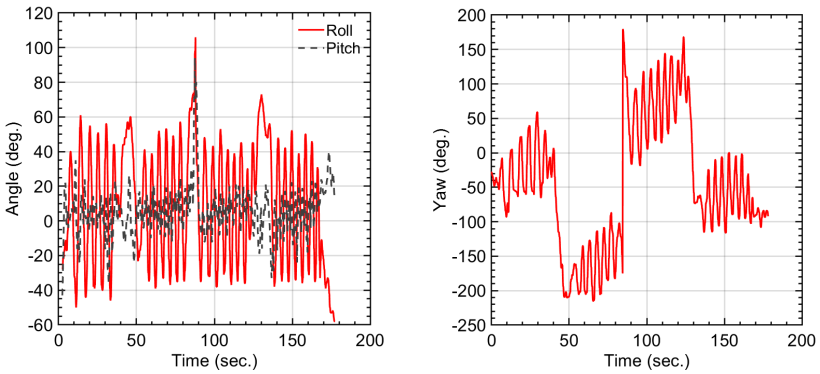

(a) Roll & Pitch angles (b) Yaw angle

Figure 2.19: Kite orientation for Test 4.

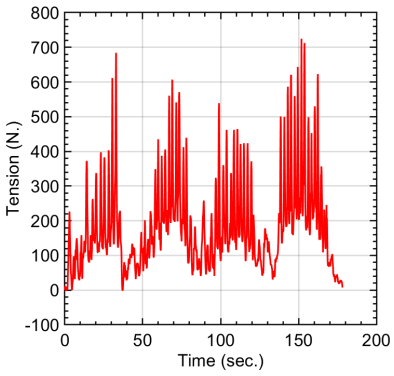

Figure 2.20: Measured tension force for Test 4.

Test 4 was performed with truck speed 50 km/h, and the kite was forced to fly in a figure-of-eight motion as shown in Figures 2.18a, 2.19 and 2.20. The truck started its motion from point A to B while the kite was doing figure-of-eight as depicted in Figure 2.18a. The readings of roll angles are fluctuating by high rates $\pm 60^{\circ}$ from its normal value, while the pitch and yaw angles were changing with small rates, $\pm 10^{\circ}$ and $\pm 30^{\circ}$ around their normal values as shown in Figures 2.19a, and 2.19b. The yaw angle changes also 180° at every turn. Due to the higher truck speed and the kite's manoeuvres, the tension forces recorded the highest readings over the four tests, average tension force was around 200 N as shown in Figure 2.20.

2.4 Data Analysis

In this section, a modified/comparable way of the experimental results in the previous section will be represented and will be used in the SI algorithm, in the next chapter. Flight tests summary is represented in Table 2.1.

Table 2.1: Flight tests outline

	Test 1	Test 2	Test 3	Test 4
Speed [km/h]	40	40	50	50
Maneuver	steady	Fig-of-8	steady	Fig-of-8

2.4.1 Overview of the 4 flight tests

In this subsection, the representation of the 4 tests will be in a comparable way to show the effect of the flight maneuver type and truck speed. Figures 2.21 and 2.23 are representing the longitude-latitude of the tests. It is easy to distinguish the effect of the flight maneuver, the steady flight, represented by the red line, is showing a straight line along the runway, except at turns at the two ends of the runway. On another hand, the figure-

of-eight flight, represented by the black line, is fluctuating around the main path of the runway. Figures 2.22 and 2.24 are representing the time history of the roll angles for the 4 tests. It is clear from each figure that the roll angle is almost zero along the runway except turns, for the case of steady flight. In the cases of the figure-of-eight flight, the rolling is fluctuating between 50° and -50° around zero along the runway. Figure 2.22 shows that the time history ends after 200 s, while in Figure 2.24 it ends after around 165 s. This difference is due to the effect of the truck speed.

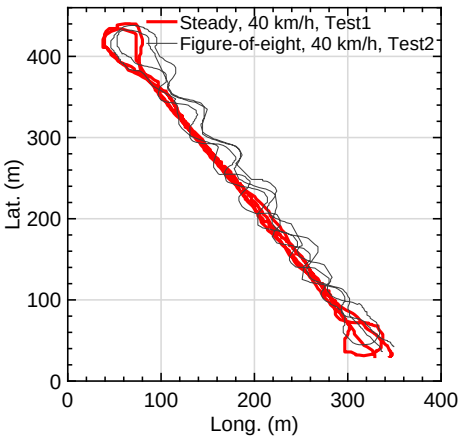

Figure 2.21: Recorded data for the longitude and latitude for Test 1 and 2.

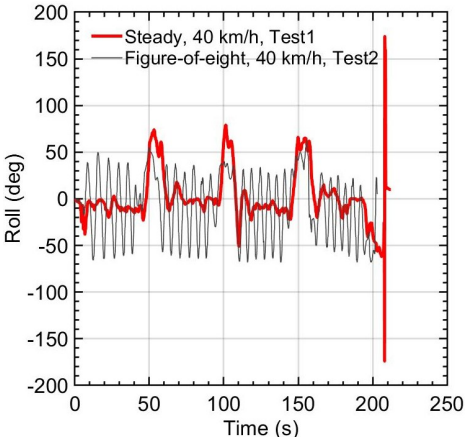

Figure 2.22: Time history of roll angle for Test 1 and 2.

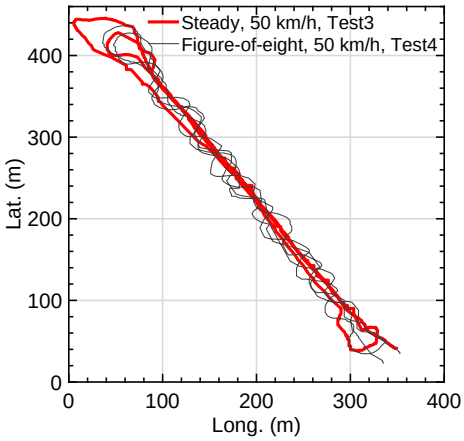

Figure 2.23: Recorded data for the longitude and latitude for Test 3 and 4.

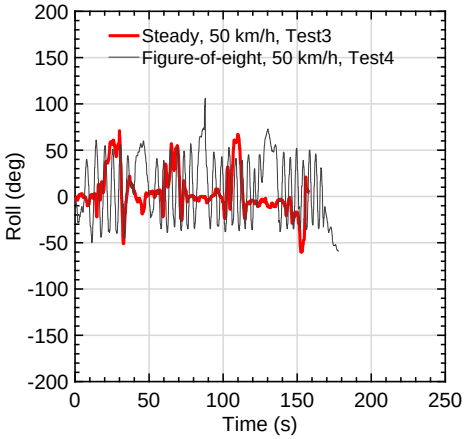

Figure 2.24: Time history of roll angle for Test 3 and 4.

2.4.2 The effects of flight maneuver and truck speed on the tension force

The following two figures show the impact of changing the truck speed and the flight mode on the measured tension force obtained from the kite and recorded using tension-meter. In Figure 2.25, a comparison between two flight modes for the same truck speed 40 km/h is presented. As shown, the steady flight had generated an average tension force of 63.16 N, and it had very small perturbations with some ups and downs at turns. On the other hand, the tension forces of the figure-of-eight path had dramatically fluctuations that reached 400 N with an average value of 128.01 N.

The tension forces result, depicted in Figure 2.26, were recorded at truck speed 50 km/h for the steady and figure-of-eight flight modes. Despite the two curves have the same behavior as shown in Figures 2.25 and 2.26, their average tension force for the steady flight was 91.95 N and the fluctuations of the figure-of-flight had become much higher. It is because of the increase in the relative wind affecting the kite which get more lifting forces from the kite body.

To analyze the data, it was separated into 4 pieces (N_1, S_1, N_2, S_2), which indicates the 4 straight ways among the two loops (A-B-A-B-A), as shown in Figure 2.6. Table 2.2 represents the time intervals of the 4 straight ways. These intervals are shown in Figure 2.25 for Test 2. Table 2.3 represents the average tension of each interval for each test.

Note that, in Table 2.4, the average tension is represented in two ways. The first way is the average all over the time history of the tension. The second way is the average of the tension measured during the straight path only (the 4 aforementioned intervals; N_1, S_1, N_2, S_2) and removing the data measured while turn. It could be noticed that the two ways result in almost the same values in the case of steady flight, but there is a big difference in the Fig-of-8 flight because the low values at the turn were deleted. It is important to mention that the turn is performed as a steady flight.

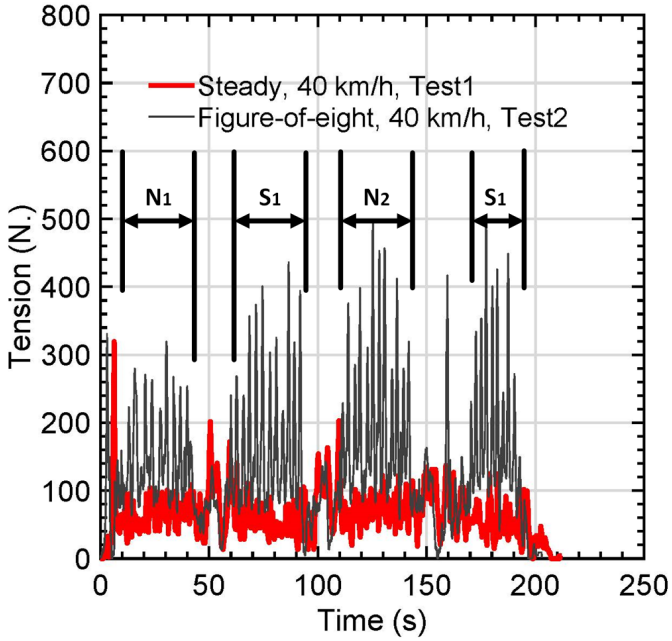

Figure 2.25: Time history of the measured tension of tests 1 and 2 at truck speed 40 km/h.

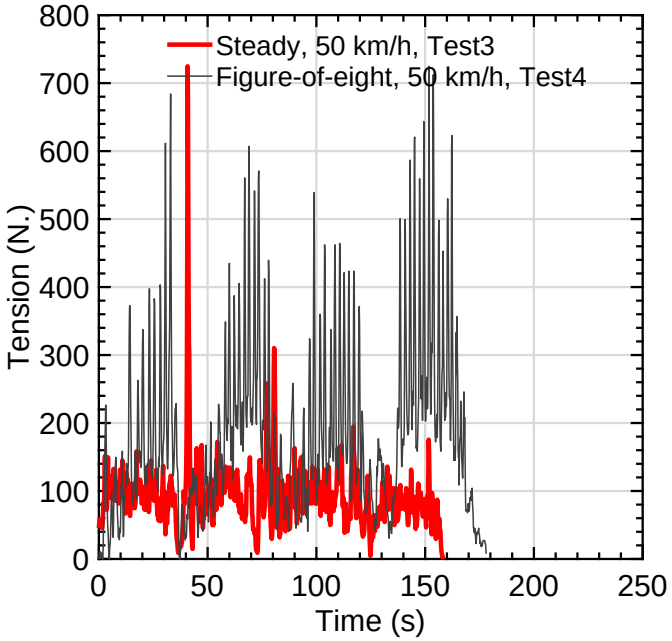

Figure 2.26: Time history of the measured tension of tests 3 and 4 at truck speed 50 km/h.

Table 2.2: The time intervals of the 4 ways without turns [s]

	Test 1	Test 2	Test 3	Test 4
N_1	15-45	10-40	5-40	17-35
S_1	55-95	60-90	50-80	60-80
N_2	115-145	110-140	90-120	100-120
S_2	170-200	165-190	130-157	140-170

Table 2.3: Average tension of each way [N]

	Test 1	Test 2	Test 3	Test 4
N_1	64.93	142.71	88.71	215.60
S_1	60.06	158.29	97.23	260.05
N_2	72.91	185.08	100.82	218.50
S_2	49.85	166.49	78.89	278.09
average	61.94	163.14	91.41	243.06
SD	24.66	87.10	31.77	126.51

Table 2.4: Average and standard deviation summaries for the tension force

	Test 1	Test 2	Test 3	Test 4
Speed [km/h]	40	40	50	50
Maneuver	steady	Fig-of-8	steady	Fig-of-8
Tension without turns [N]	61.94	163.14	91.41	243.06
Tension including turns [N]	63.16	128.01	91.95	178.26
Standard deviation (SD)	24.66	87.10	31.77	126.51

Table 2.5: The average tension measured in the N & S directions to indicate the influence of wind speed

	Test 1	Test 2	Test 3	Test 4
N_1 & N_2	68.92	163.89	94.76	181.66
S_1 & S_2	54.96	162.39	88.06	269.07
average	61.94	163.14	91.41	243.06

Table 2.5 represents the average tension measured in the N and S directions to indicate the influence of wind speed. It seems that, at the first three tests the wind direction was to the north then changed at the time of the forth test. As the values of the average tension is always higher in the N direction, as shown in Table 2.5, except for the last test.

2.5 Conclusions

In this chapter, a full description of kite system has been discussed. It included the electronics technology, kite specifications, and control actuator to steer the kite (KCU). Tow types of tests was addressed. Four truck towing tests have been performed and discussed in this chapter. The data of those tests were presented; positions, heights, attitude, and tension forces.

Tests 1 (2.3.2 (1)) and Test 2 (2.3.2 (2)) were performed for the same wind speed, but with different flight conditions to show the influence of kite motion on the tension force resulted from the kite. Moreover, Test 3 and Test 4 had also the same wind speed, but higher than the first two tests. The results of tension forces obtained from Test 3 (2.3.2 (3)) and Test 4 (2.3.2 (4)) were given and discussed to show the effect of wind speed on the total force generated from the kite.

Chapter 3

System Identification of a 6 m^2 Kite Power System in Fixed-Tether Length Operation

Contents

This chapter aims to apply system identification (SI) to the data from Chapter 2, to identify the correlation between the tension force and kite rolling angle. This is a study of the kite behavior as a preliminary step for the autonomous flight. It could be said that the novelty in this chapter is the using of the SI algorithm to identify the kite behavior

based on an experimental data.

3.1 Introduction

Early work in system identification was developed by the statistics and time-series communities. It has its roots since the middle of eighteenth century and it is intimately related to the theory of stochastic processes. In 1960, it began to experience dramatic improvements with the start of the state-space era. Most notably the year 1965 witnessed the simultaneous appearance of two milestone seminal papers, one by Ho and Kalman [41], and the other by Astrom and Bohlin [42], which gave birth to modern system identification, and established it as a new paradigm in various engineering disciplines. Since then, identification techniques and algorithms have been gradually and continuously evolving [43]. Nowadays, SI techniques are used in a variety of scientific and engineering applications, including the chemical [44], medical [45], mechanical [46], aerospace [47], wind energy [48] areas. In particular, new techniques of machine learning [49] blossomed during the past decade.

By using SI methodology, it could be possible to take advantage of statistical methods to build a mathematical model for the current dynamic system, based on the available measured data [50]. Knowing the input and output only and treating the whole dynamical system as a black box, SI enables us to come up with a transfer function that describes the system. For that reason, SI is widely used when it is hard to describe a system. In the AWE community, SI was used in several papers, using a kite [51], [52] or an aircraft [53], [54] as a flying device.

3.2 System Identification

The results presented in this section are based on the four flight tests illustrated in Section 2.4. Each test consists of 2 complete cycles. The flight motion of the kite is affected by different parameters, such as the change in the truck speed at turns, the steering actuation of the KCU, and the change in the kite's dynamics due to the variation of truck speed. As a result, the SI algorithm was applied to identify those parameters utilizing the experimental data. The recorded data obtained from the measurement unit and tension-meter were sufficient to identify the parameters of the transfer function a_1, a_2, b_1 and b_2 in real time, noting that these parameters don't have direct physical meaning (as common in control engineering), but they will be able to describe the behavior of the kite. There are two typical approaches for the simulation of AWE. The first one is accurate dynamic model with precise parameters. And the other one is estimating the characteristics by the flight data. The present approach is the second one. So, the SI algorithm could be one of the choices to define the kite dynamics. The results presented in this section will be crucial to develop the autonomous flights as a future work.

3.2.1 The SI algorithm

The purpose of applying the SI algorithm is to calculate approximate values for the system parameters during flying using the recorded sensor data. Consequently, it is required to update the parameters in real time by analyzing the history of the tension force and rolling angle [51]. There are several techniques for the parameter estimation, the applied technique here is called Plackett's algorithm (Appendix A) [55,56]. The chosen algorithm calculates the system parameters rapidly, without iterations. Moreover, it has no singularity and the implementation on a micro-controller is very simple.

The algorithm minimize the mean square error (MSE) of the tension force measured

via the tension-meter as defined by:

$$MSE = \frac{1}{k}\sum_{r=1}^{k}(Y_r - Y_{m,r})^2, \tag{3.1}$$

where k is total number of time steps in the discrete time process, $Y_{m,r}$ is the measured data for time step r and Y_r the estimated value determined by the SI algorithm. The open-loop transfer function (TF) of the kite, Eq. 3.6, illustrates the relation between the tension force and the kite's rolling angle. The rolling angle are denoted as $U(z^{-1})$ and the tension force is expressed as $Y(z^{-1})$. The block diagram of the SI algorithm is illustrated in Figure 3.1.

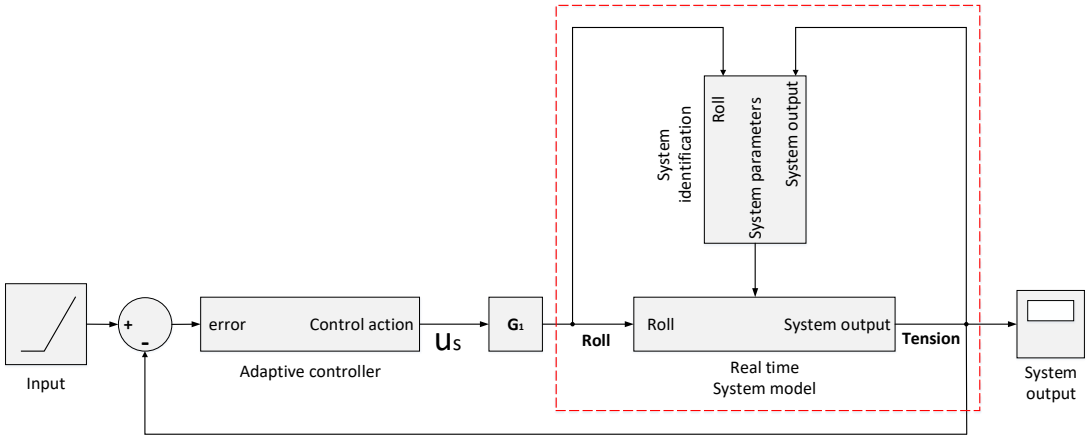

Figure 3.1: Block diagram of the SI algorithm and adaptive control system.

The SI algorithm will estimate the tension forces and update the coefficients of the open-loop TF a_1, a_2, b_1 and b_2 based on the variation of the rolling angle to generate the open-loop TF illustrated in Eq. 3.6. The data discussed in subsection 3.2.2 considered the tension force obtained from the experiments in Section 2.4 as a measured tension force. This force data was used with the rolling angle values of the kite to calculate the estimated tension force of the four flight tests, in difference form as follows

$$Y_k = -a_1 Y_{k-1} - a_2 Y_{k-2} + b_1 U_{k-1} + b_2 U_{k-2}. \tag{3.2}$$

The open-loop TF for the correlation between the tension force and the kite rolling angle in z-form can be approximated as

$$G(z^{-1}) = \frac{Y(z^{-1})}{U(z^{-1})} = \frac{B(z^{-1})}{A(z^{-1})}, \tag{3.3}$$

where $A(z^{-1})$ and $B(z^{-1})$ are considered as second order polynomial equations in z-form

$$A(z^{-1}) = 1 + a_1 z^{-1} + a_2 z^{-2}, \tag{3.4}$$

$$B(z^{-1}) = b_1 z^{-1} + b_2 z^{-2}. \tag{3.5}$$

The coefficients a_1, a_2, b_1 and b_2 are changing with time due to the variation of the system's dynamics. From Eqs. 3.4 and 3.5, Eq. 3.3 could be written as follows:

$$\frac{Y}{U}(z^{-1}) = G(z^{-1}) = \frac{b_1 z^{-1} + b_2 z^{-2}}{1 + a_1 z^{-1} + a_2 z^{-2}}. \tag{3.6}$$

3.2.2 Parameter identification

The kite parameters presented in this subsection discuss the change occurred for every flight test. The data for the parameters a_1 and a_2 are almost constant for the four tests, however, the values of b_1 and b_2 vary depending on the truck speed and flight mode. The following average values are the average of the time history after cutting the unnecessary/turn data, as illustrated in Section 2.4.

(1) Test 1: Steady flight with truck speed 40 km/h:

In Test 1, the values of the parameters b_1 and b_2 were changing at every half cycle as the truck performs the half cycle every 50 s. The average values of the variables a_1, a_2

were -1.393, 0.347 respectively. The variables b_1 and b_2 were fluctuating with average values -40.273 and 35.813 respectively, as shown in Figure 3.2. Table 3.1 represents the average values of the SI parameters for Test 1 for the four straight ways and the total average.

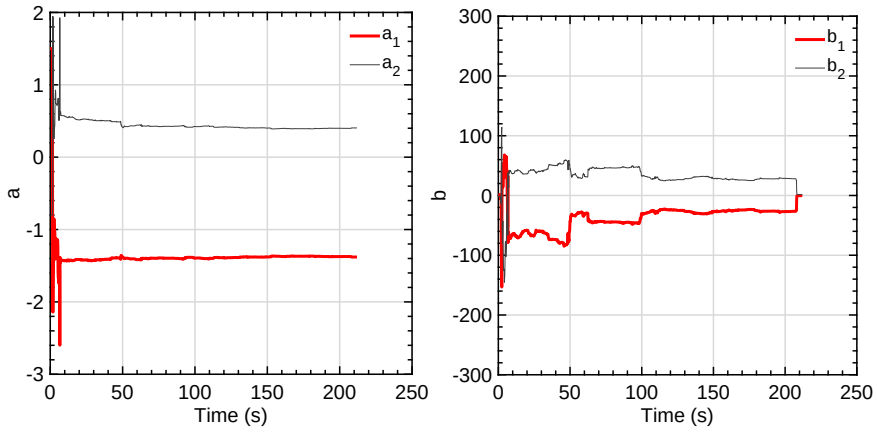

(a) a_1 & a_2 parameters (b) b_1 & b_2 parameters

Figure 3.2: Time history for the SI parameters (a and b) from Test 1.

Table 3.1: Average and standard deviation (SD) values of the SI parameters for Test 1

Test 1	N_1	S_1	N_2	S_2	average	SD
a_1	-1.416	-1.399	-1.384	-1.371	-1.393	0.017
a_2	0.512	0.429	0.410	0.396	0.347	0.044
b_1	-66.911	-41.877	-26.569	-25.643	-40.273	16.27
b_2	44.147	43.544	28.246	27.314	35.813	9.21

To check that the SI algorithm is working well, the data of Test 1 was split and the algorithm was run twice and the results are presented in Figures 3.3 and 3.4.

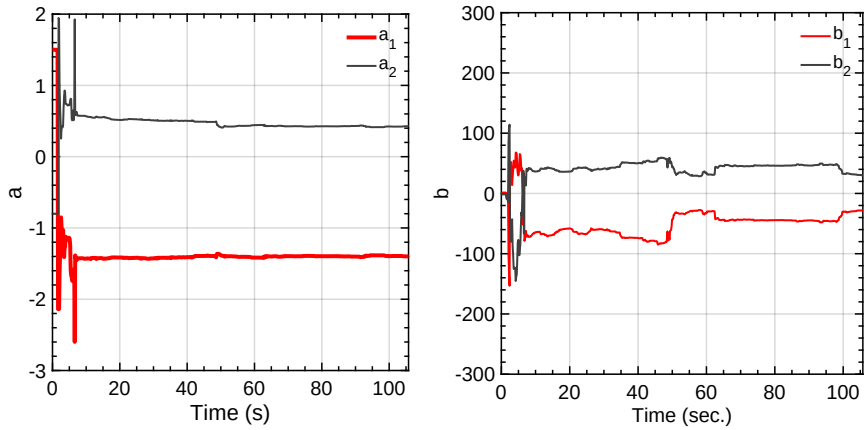

(a) a_1 & a_2 parameters (b) b_1 & b_2 parameters

Figure 3.3: Time history of the SI parameters (a and b) from the 1st half data of Test 1.

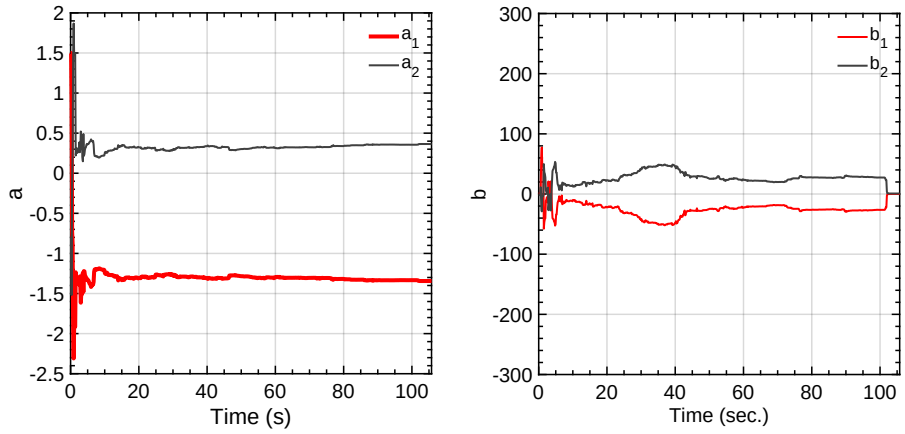

(a) a_1 & a_2 parameters (b) b_1 & b_2 parameters

Figure 3.4: Time history of the SI parameters (a and b) from the 2nd half of Test 1.

It was expected to have almost the same values for the parameters of the two data sets along with the original Test 1 results. The average values of the SI parameters for 1st split of Test 1, which represented in Table 3.2, are exactly the same as the first two columns in Table 3.1, which represent the average values of the SI parameters for

Test 1. However, the average values of the SI parameters for 2nd split of Test 1, which represented in Table 3.3, are not the same as the second two columns in Table 3.1. This is because of the change in the initial condition and the algorithm needs some time to settle at the same values. By a closer look to the SI parameters for Test 1, shown in Figure 3.2, and the SI parameters for two splits, shown in Figures 3.3 and 3.4, it could be noticed that Figure 3.3 is exactly the same as the first half of the Figure 3.2. On the other hand, the Figure 3.4 is a little different from the second half of Figure 3.2 for the first 40 s, then they have the same pattern and settle in to the same values, this indicate the effect of the initial condition. The ultimate benefit gain from the SI algorithm is to use it in real-time, which means different SI parameters values and different transfer functions, accompanied by a controller, adaptive controller for example. In the cases that the SI parameters are not changing dramatically (like the current case), it could be possible to use the average values of the SI parameters, which means only one transfer function, and the controller will still be able to control the system.

Table 3.2: Average and SD values of the SI parameters for 1st split of Test 1

	N_1	S_1	average	SD
a_1	-1.416	-1.399	-1.408	0.011
a_2	0.512	0.429	0.471	0.042
b_1	-66.911	-41.877	-54.394	13.906
b_2	44.147	43.544	43.846	5.954

Table 3.3: Average and SD values of the SI parameters for 2nd split of Test 1

	N_2	S_2	average	SD
a_1	-1.285	-1.319	-1.302	0.025
a_2	0.306	0.339	0.323	0.026
b_1	-30.434	-24.178	-27.306	10.481
b_2	30.516	25.632	28.074	9.245

Table 3.4: Summary of the average values of the SI parameters for Test 1 and the two split sets

	Whole Test 1	1st split of Test 1	2nd split of Test 1
a_1	-1.393	-1.408	-1.302
a_2	0.347	0.471	0.323
b_1	-40.273	-54.394	-27.306
b_2	35.813	43.846	28.074

(2) Test 2: Figure-of-eight flight with truck speed 40 km/h:

Test 2 had a different performance for the parameters b_1 and b_2 as the kite was performing a figure-of-eight motion with the same truck speed 40 km/h. Those parameters started with high values as they had a very strong sudden tension force which affected the calculations of the SI algorithm. The average values of the parameters a_1, a_2, b_1, b_2 are -1.546, 0.575, 1.701, and -3.134 respectively, as shown in Figure 3.5. Table 3.5 represents the average values of the SI parameters for Test 2 for the four straight ways and the total average.

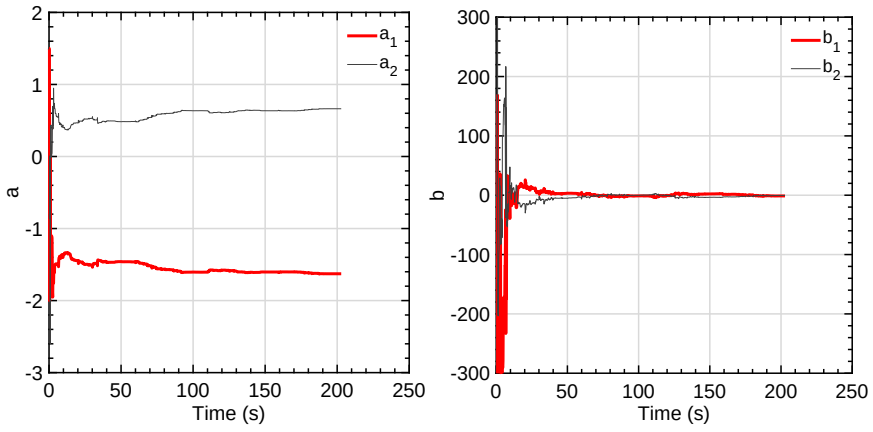

(a) a_1 & a_2 parameters (b) b_1 & b_2 parameters

Figure 3.5: Time history for the SI parameters (a and b) from Test 2.

Table 3.5: Average and SD values of the SI parameters for Test 2

Test 2	N_1	S_1	N_2	S_2	average	SD
a_1	-1.447	-1.536	-1.590	-1.612	-1.546	0.07224
a_2	0.473	0.562	0.621	0.645	0.575	0.07417
b_1	6.859	-0.609	0.421	0.132	1.701	5.36157
b_2	-8.406	-0.723	-1.824	-1.581	-3.134	5.36151

(3) Test 3: Steady flight with truck speed 50 km/h:

Test 3 was performed for the truck speed 50 km/h and steady flight mode. The identified parameters of the kite a_1 and a_2 had almost the same values as Tests 1 and 2. However, those parameters started with different values then settled with values -1.5 and 0.5 at the time 40 s till the end of the two cycles, but the average value will be -1.434 and 0.462. The parameters of b_1 and b_2 were perturbating with high rate in the beginning of the simulation then became steady after 10 s, as shown in Figure 3.6. The reason of this fluctuation is that the initial conditions were not close to the exact solution, then it took more time to settle. The average values for the parameters b_1 and b_2 were -2.109 and 2.354 respectively. Table 3.6 represents the average values of the SI parameters for Test 3 for the four straight ways and the total average.

Table 3.6: Average and SD values of the SI parameters for Test 3

Test 3	N_1	S_1	N_2	S_2	average	SD
a_1	-1.230	-1.510	-1.504	-1.491	-1.434	0.123
a_2	0.244	0.547	0.538	0.520	0.462	0.133
b_1	-15.971	1.753	2.784	2.995	-2.109	12.091
b_2	9.192	1.105	0.111	-0.990	2.354	10.417

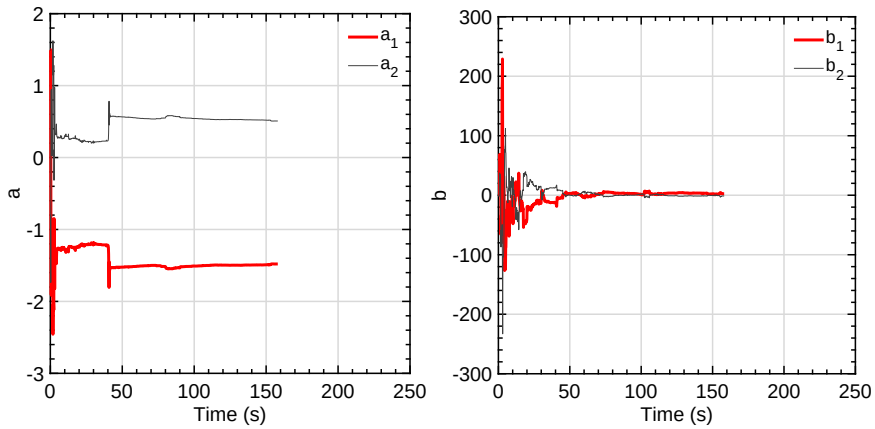

(a) a_1 & a_2 parameters (b) b_1 & b_2 parameters

Figure 3.6: Time history for the SI parameters (a and b) from Test 3.

(4) Test 4: Figure-of-eight flight with truck speed 50 km/h:

In Test 4, the kite was flying in a figure-of-eight path with truck speed 50 km/h. The values of parameters a_1 and a_2 were almost the same as the previous three tests with an average values -1.614 and 0.652. The variables b_1 and b_2 started with fluctuations then settled in a steady line with a smooth deviation with time with average values 27.148 and -26.200, as shown in Figure 3.7. Table 3.7 represents the average values of the SI parameters for Test 4 for the four straight ways and the total average.

Table 3.7: Average and SD values of the SI parameters for Test 4

Test 4	N_1	S_1	N_2	S_2	average	SD
a_1	-1.629	-1.605	-1.617	-1.606	-1.614	0.018
a_2	0.664	0.642	0.656	0.646	0.652	0.017
b_1	30.685	31.009	26.493	20.407	27.148	5.445
b_2	-31.853	-29.775	-24.847	-18.323	-26.200	6.175

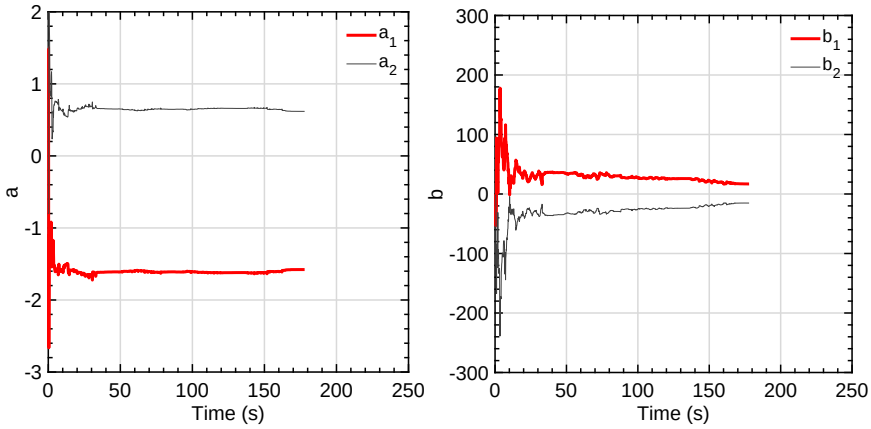

(a) a_1 & a_2 parameters (b) b_1 & b_2 parameters

Figure 3.7: Time history for the SI parameters (a and b) from Test 4.

From Figures 3.2-3.7, it is important to note that all the variables should be settled at the values of its average value of the whole time history (without any trimming) except the values of b_1 and b_2 in Test 2 and 3, because of the huge fluctuations at the beginning. The summary of the average values of the SI parameters for the four tests are represented in Table 3.8.

Table 3.8: Summary of the average values of the SI parameters for the four tests

	Test 1	Test 2	Test 3	Test 4
a_1	-1.393	-1.546	-1.434	-1.614
a_2	0.347	0.575	0.462	0.652
b_1	-40.273	1.701	-2.109	27.148
b_2	35.813	-3.134	2.354	-26.200

The used SI technique needs some time to settle its parameters. Therefore, it was noticed that, the parameters are not settled for the same condition before 40 s of the starting time of recording. The SI technique is very powerful when you are trying to identify a system based on one input/output, just like the current case. If there are more

features that affecting the output, then machine learning techniques will be better to describe the system.

3.3 Conclusion

In this chapter, the experimental results obtained from fixed-tether length kite operation was studied. This work shows the influence of increasing the wind speed and flying in different paths on the lifting force obtained from the kite during flying. For the same wind speed, the 6 m^2 kite can get average tension force during flying in figure-of-eight path almost two times its value in the steady flight. Furthermore, the tension force obtained from the kite becomes two times after increasing the wind speed just 25 % of its original value for the same flight path.

Four different flight tests were performed to identify the relation between the tension force and rolling angle using SI algorithm. This technique was assessed on the basis of the four flight tests that were characterized by different wind speeds and flight paths. Therefore, every test had a different correlation between the tension force and rolling angle. Those correlations included four parameters to define the TF that can be used to design and implement the autonomous flight.

The aim of this study is to identify the kite using SI parameters in real-time. So, it could be possible to apply and implement any control technique, the model predictive controller (MPC) for example, to stabilize the kite in a real-time flight. Even though that the SI was used within AWE before, the novelty in this work is the using of the SI algorithm to identify the kite behavior based on experimental data.

Chapter 4

Sensitivity Analysis and Power Prediction of AWE using Machine Learning

Contents

This chapter aims to apply machine learning (ML) to an enhanced data from the presented one in Chapter 2. Starting with selecting the appropriate features and the highly correlated with the output among those features, as a preprocessing analysis. Then applying the ML algorithms for power prediction. This part is considered the main novelty of the thesis, as this is the first attempt to apply ML within the AWE community. The data-based sensitivity analysis was consistent with the model-based sensitivity analysis, even with the small number of samples available. The performance of different ML techniques was assessed and the neural network algorithm proves its superiority over the other algorithms.

4.1 Introduction

4.1.1 Machine learning methods in AWE

Accurate modeling of nonlinear input-output relations is crucial for achieving high-quality solutions of classification and regression problems. This modeling process has been substantially improved with the emergence of the methods of machine learning (ML) and deep learning (DL). Those methods extend to multivariate problems where the number of input variables or features is quite high. The ML and DL methods have

demonstrated superior outcomes in the fields of computer vision [57], statistical pattern analysis [57], bioinformatics [58], and computer-aided medical diagnosis [59]. The wide applicability of ML and DL methods has been boosted by the creation of hardware-optimized software libraries including Scikit Learn [60], PyTorch [61], and TensorFlow [62].

One large class of widely used ML methods is based on supervised learning, where pairs of the input $\mathbf{x}$ and output y variables are used to learn an approximate input-output mapping $y = f(\mathbf{x})$ through the optimization of some objective function. Then, given new unlabeled test data samples $\mathbf{x}^*$, the associated outputs could be predicted using the learned mapping. For example, in one-dimensional linear regression, it is sought to fit a line $y = ax + b$ to a set of n labeled points $\{\mathbf{x}, y\}_{i=1}^{n}$ such that the sum of the least-square errors (or any other loss function) is minimized.

A one-dimensional illustration, using linear regression, is shown in Figure 4.1 in which fitting a linear model $y = ax + b$ to a set of n labeled points $\{\mathbf{x}, y\}_{i=1}^{n}$, in order to minimize the sum of least-square errors.

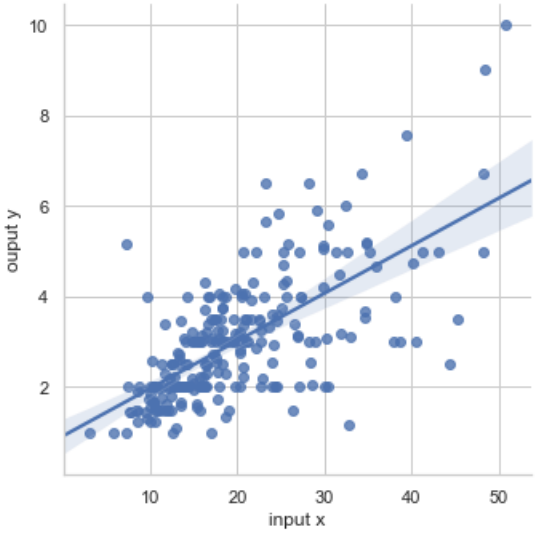

Figure 4.1: One-dimensional illustration of a linear regression ML model.

Numerous approaches have been proposed to design model-based AWE systems with different flight mechanisms such as kites [8, 51, 63, 64] and tethered aircrafts [18, 54, 65]. However, few approaches involved experimental verification [66], data-driven methods [67], and system identification [51–53, 68]. Dief et al. [40] collected experimental data from early flight tests, but no in-depth data analysis was performed. In this work, the data collection process is enhanced and more flight tests are carried out to collect more data. Then, machine learning algorithms are applied to predict the power generation in AWE systems. To the best of our knowledge, this work represents the first attempt to employ machine learning schemes in AWE systems, albeit some notable approaches generally exploited machine learning in wind energy research (see, e.g., [69–72])

4.1.2 Contribution and organization

In this chapter, the AWE research platform [73] developed at Kyushu University was exploited. A detailed description of this platform is given in Chapter 2, and covers the system set-up, the ground station, and the kite control unit (KCU). The kite performance was analyzed through several tests of truck speeds and flight conditions. For each of these flight tests, the tether force curve was generated and analyzed. Then, several machine learning algorithms and sensitivity analysis were applied for output power prediction in the AWE system.

This chapter has four sections. Section 4.2 summarizes the statistics of the data collected based on the AWE system set-up of Chapter 2. Section 4.3 discusses the experimental setup and results for the truck tests. Data and sensitivity analyses are described in Section 4.4. The machine learning system construction and the model performance evaluation are detailed in Section 4.5. Neural networks and other machine learning techniques are reviewed in Section 4.6.Section 4.7 contains conclusions and future research directions.

4.2 Data Collection

The collected multi-sensor data is listed in Table 4.1. Two data attributes, not displayed in Table 4.1 as they are almost constants and not necessary, are the sampling time (or time step) and the number of satellites to which the GPS is connected (or satellite count). Two other data attributes were considered: the maneuver type (steady flight or figure-of-eight maneuver), and the control line length (CLL). As shown in Figure 2.7 (left), the nominal angle of attack is controlled by the difference in length between the control lines and the power line controls. The output is the tether force, a key factor for power generation. This force was measured using a tension meter. Another important factor for generating power is the tether reeling speed which can be measured using a drum/generator module. In the current work, the reeling speed wasn't considered.

Some statistics of the collected data is presented in Table 4.1. These statistics include the minimum, the maximum, the mean, the standard deviation (std), and the median or the 50th percentile (50%). A percentile statistic indicates a data value below which a certain percentage of data samples falls.

Table 4.1: Multi-sensor data and statistics for the kite-based AWE system.

	Kite Position			Kite Orientation			Towing speed [km/h]	Tether force [N] (output)
	Longitude [deg]	Latitude [deg]	Height [m]	Roll [deg]	Pitch [deg]	Yaw [deg]		
min	130.186294	33.146762	38.5	-178.0	-159.0	-196.0	0.0	0.0
max	130.189163	33.150520	90.8	176.0	129.0	179.0	50.6	1263.8
mean	130.187766	33.148546	73.8	0.9	5.5	-16.1	32.7	118.0
std	0.000823	0.001138	12.3	30.8	22.6	101.8	12.2	94.3
median	130.187774	33.148536	77.7	0.0	8.0	-2.0	36.8	97.3

4.3 Design of Experiment (DOE)

This section shows the experimental setup and results for seven tests (summarized in Table 4.2) with different combinations of towing speeds, kite maneuvers, and control

line lengths. These tests were designed to quantify the influence of those parameters on the tether force. For the first four tests, a continuous towing path A-B-A-B-A with two loops was followed by the truck on the runway (see Figure 2.6). At the end points A and B, the truck reduced its speed to 20 km/h and had a U-turn. For the remaining three tests, only a single loop was traced. During the towing operation, the kite either performed figure-of-eight flight maneuvers, or was flying in a steady state while keeping a constant distance from the truck.

Next, the outcomes of the seven tests will be represented. Figure 4.2 shows 3D plots of the trajectories of the kite and the truck for tests in which the kite either has a steady flight, or carries on a figure-of-eight maneuver. The crosswind maneuver effects may be identified from the tether force evolution patterns for cases of similar towing speeds, such as Tests 1 and 2. As demonstrated in Figure 4.3, the tether force nearly doubled and exhibited stronger fluctuations for the figure-of-eight flight maneuver. For the steady-state flight mode, Figure 4.4 shows how the tether force increases with increasing the towing speed, as in Tests 1 and 3. For Figures 4.5 to 4.11, Subfigures b, d, e, and f demonstrate similar sinusoidal patterns. This obviously reflects the towing loop count, which is 2 for Tests 1–4 and just 1 for Tests 5–6. Figures 4.5 to 4.11 show the data used for training and testing of the ML algorithm.

Table 4.2: Specifications for seven tests with different combinations of the truck speed, the flight mode, and the control line length (CLL).

Test no.	Towing speed [km/h]	Flight mode	CLL [m]
1	$30 \sim 40$	Steady flight	13.8
2	$30 \sim 40$	Figure-of-eight maneuvers	13.8
3	$40 \sim 50$	Steady flight	13.8
4	$40 \sim 50$	Figure-of-eight maneuvers	13.8
5	$30 \sim 40$	Steady flight	13.6
6	$30 \sim 40$	Steady flight	13.4
7	$40 \sim 50$	Steady flight	13.6

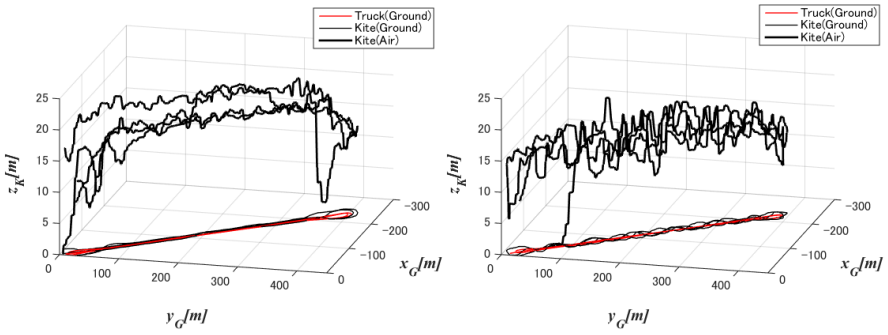

(a) Test 1: A kite in a steady flight mode (b) Test 2: A kite making a fig-of-8 maneuver

Figure 4.2: A 3D plot of the kite spatial trajectory for Tests 1 and 2.

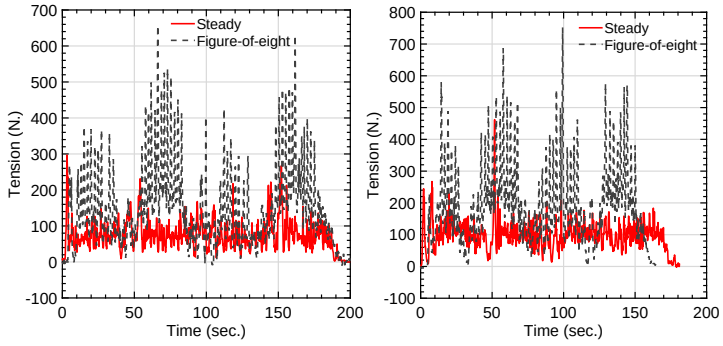

(a) 30 ∼ 40 km/h (b) 40 ∼ 50 km/h

Figure 4.3: Flight mode effects for (a) Tests 1 [red line] & 2 [black dash line] and (b) Tests 3 [red line] & 4 [black dash line].

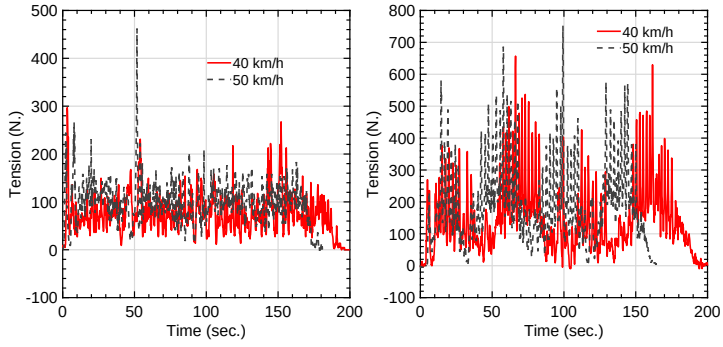

(a) A kite in a steady flight mode (b) A kite making a fig-of-8 maneuver

Figure 4.4: Towing speed effects for (a) Tests 1 [red line] & 3 [black dash line] and (b) Tests 2 [red line] & 4 [black dash line].

(1) Test 1: A kite in a steady-flight mode with a towing speed of 30∼40 km/h and a CLL of 13.8 m

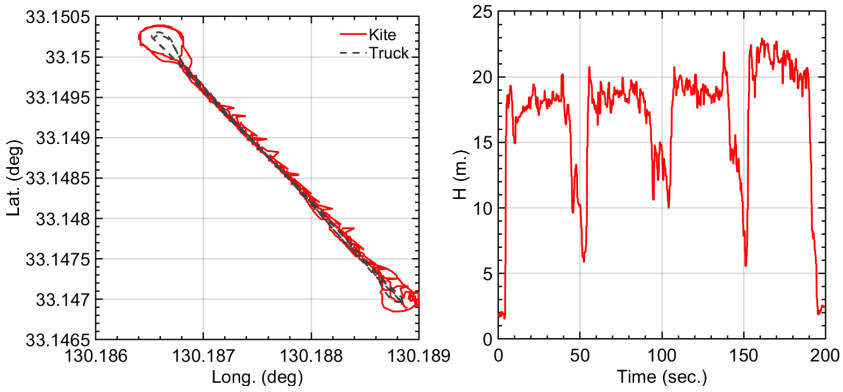

(a) Longitude-latitude

(b) Height

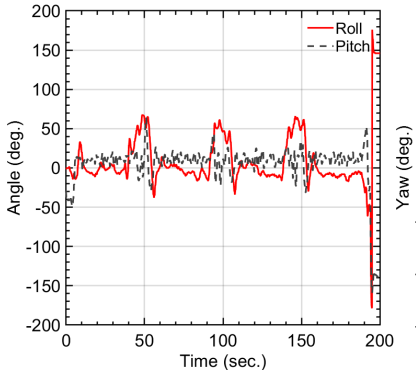

(c) Roll & pitch angles

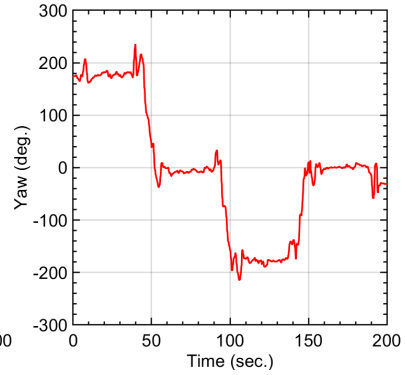

(d) Yaw angle

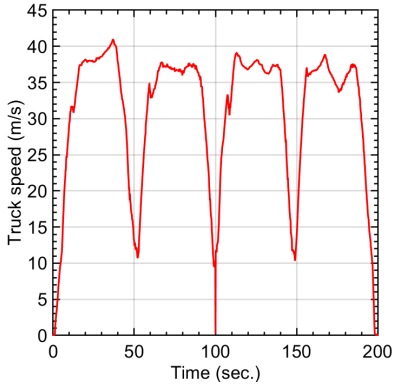

(e) Towing speed

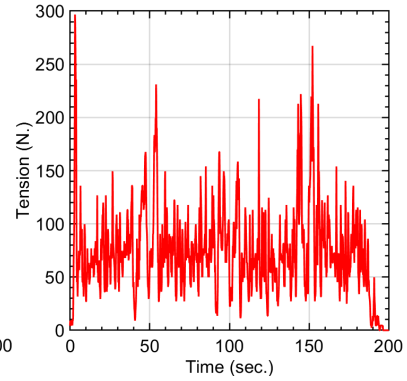

(f) Tether force

Figure 4.5: Data set from Test 1.

(2) Test 2: A kite in a figure-of-eight maneuver with a towing speed of 30∼40 km/h and a CLL of 13.8 m

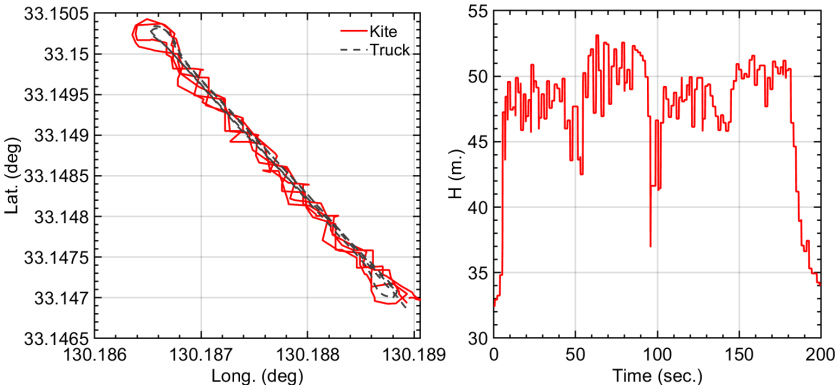

(a) Longitude-latitude

(b) Height

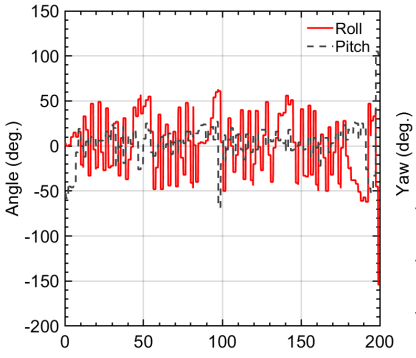

(c) Roll & pitch angles

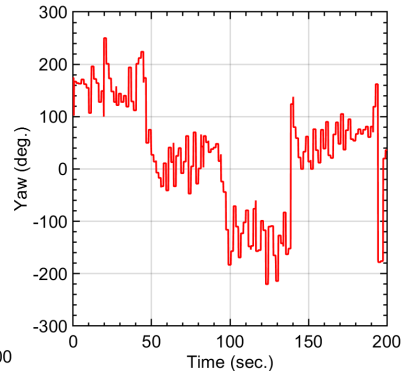

(d) Yaw angle

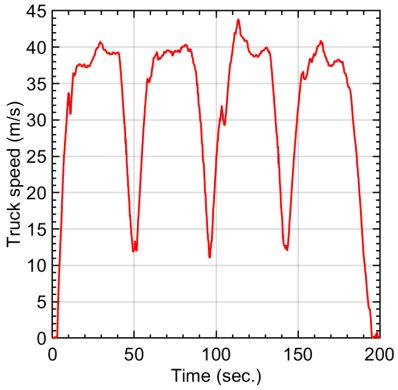

(e) Towing speed

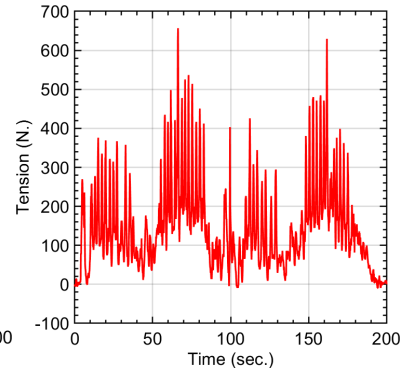

(f) Tether force

Figure 4.6: Data set from Test 2.

(3) Test 3: A kite in a steady-flight mode with a towing speed of 40∼50 km/h and a CLL of 13.8 m

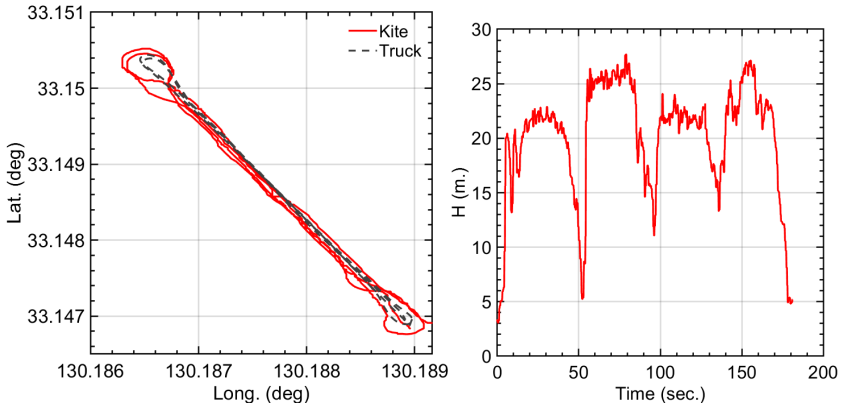

(a) Longitude-latitude

(b) Height

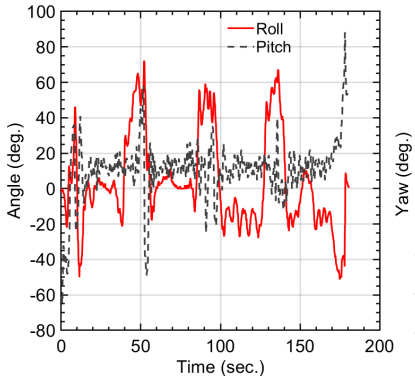

(c) Roll & pitch angles

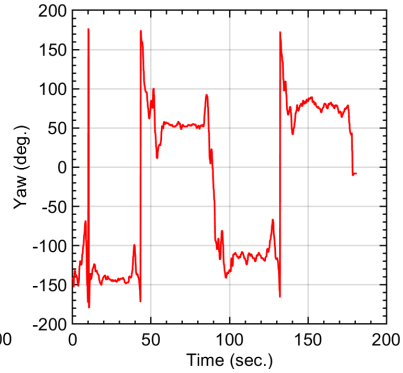

(d) Yaw angle

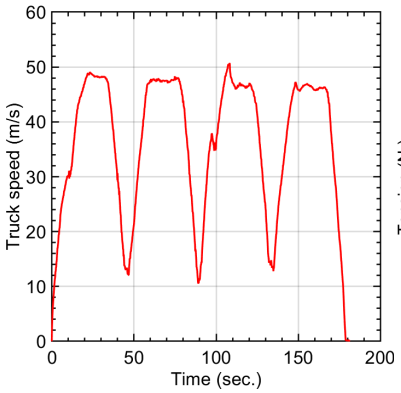

(e) Towing speed

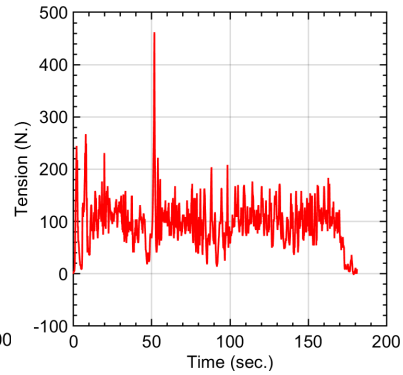

(f) Tether force

Figure 4.7: Data set from Test 3.

(4) Test 4: A kite in a figure-of-eight maneuver with a towing speed of 40∼50 km/h and a CLL of 13.8 m

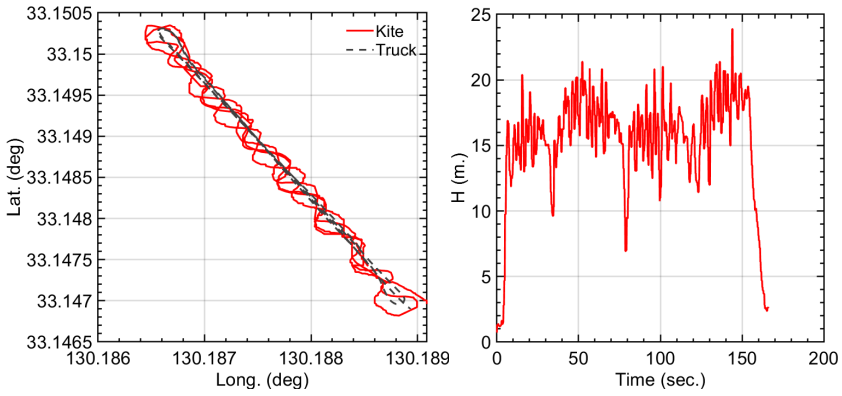

(a) Longitude-latitude (b) Height

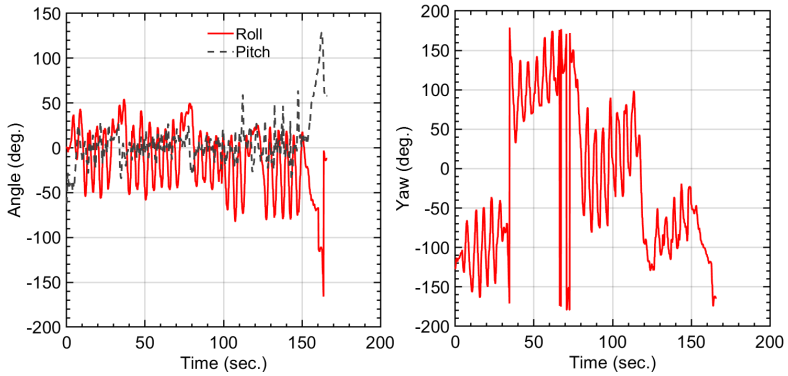

(c) Roll & pitch angles (d) Yaw angle

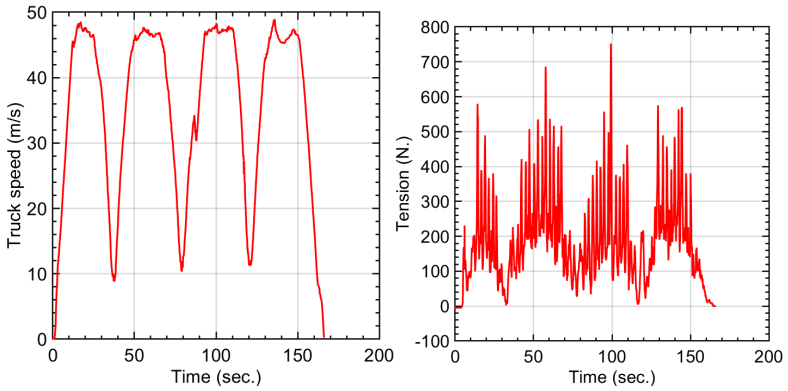

(e) Towing speed (f) Tether force

Figure 4.8: Data set from Test 4.

(5) Test 5: A kite in a steady-flight mode with a towing speed of 30∼40 km/h and a CLL of 13.6 m

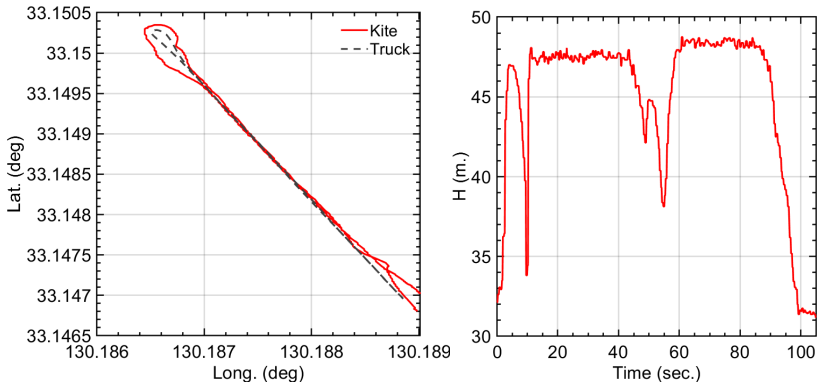

(a) Longitude-latitude (b) Height

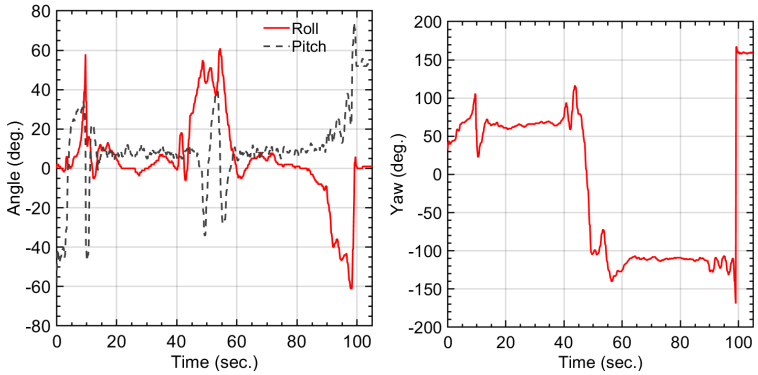

(c) Roll & pitch angles (d) Yaw angle

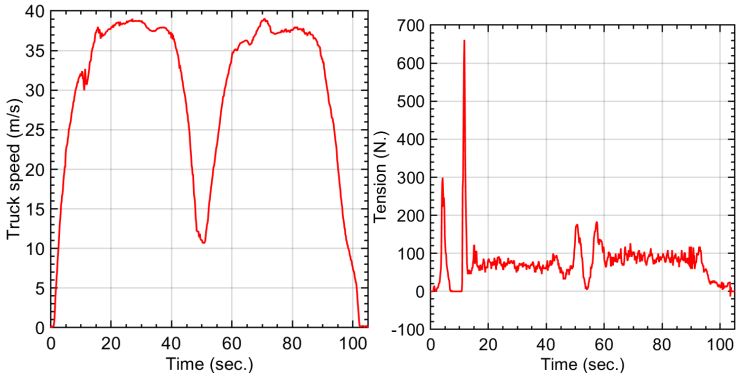

(e) Towing speed (f) Tether force

Figure 4.9: Data set from Test 5.

(6) Test 6: A kite in a steady-flight mode with a towing speed of 30∼40 km/h and a CLL of 13.4 m

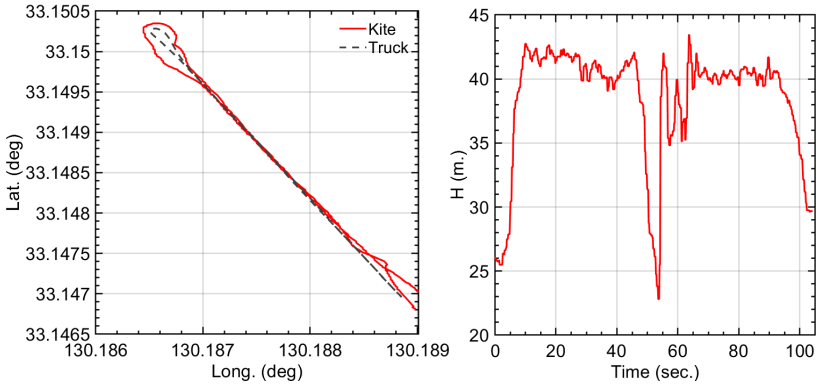

(a) Longitude-latitude

(b) Height

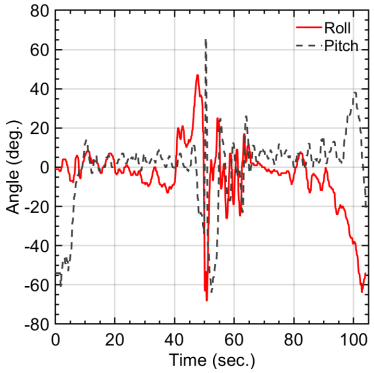

(c) Roll & pitch angles

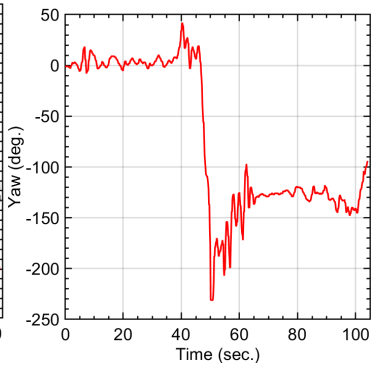

(d) Yaw angle

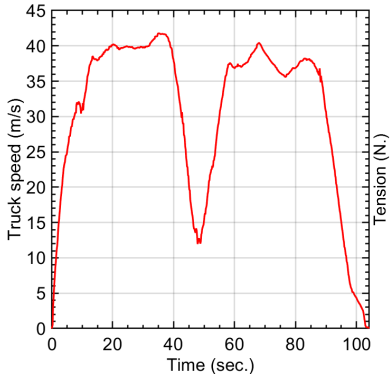

(e) Towing speed

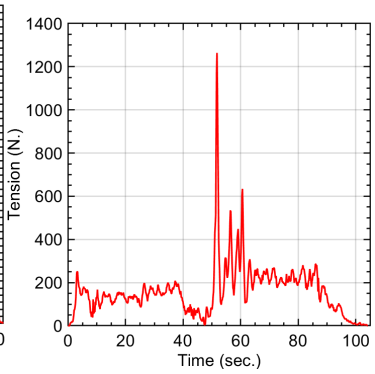

(f) Tether force

Figure 4.10: Data set from Test 6.

(7) Test 7: A kite in a steady-flight mode with a towing speed of 40∼50 km/h and a CLL of 13.6 m

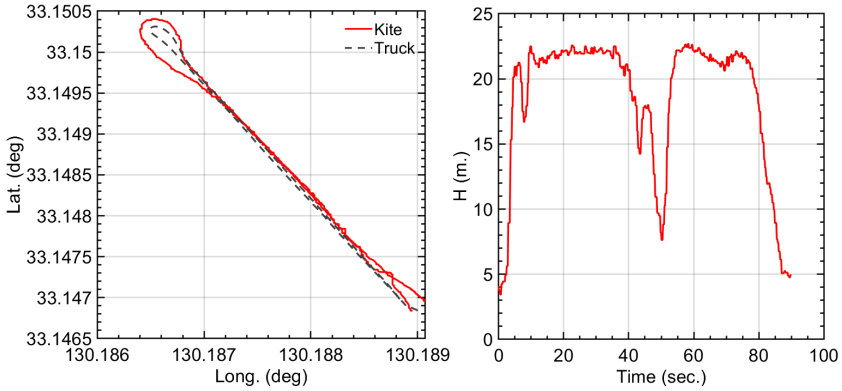

(a) Longitude-latitude (b) Height

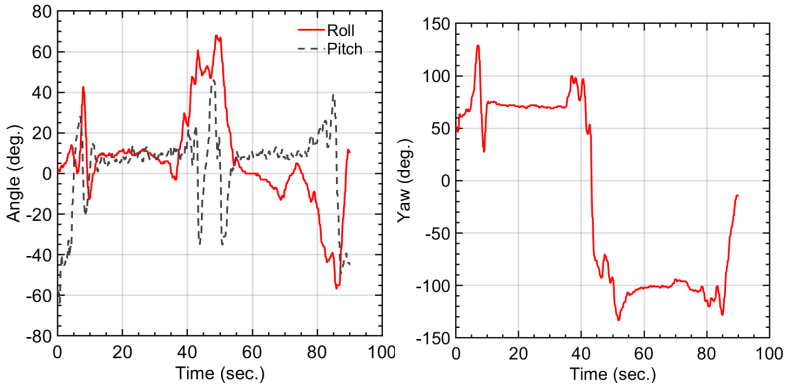

(c) Roll & pitch angles (d) Yaw angle

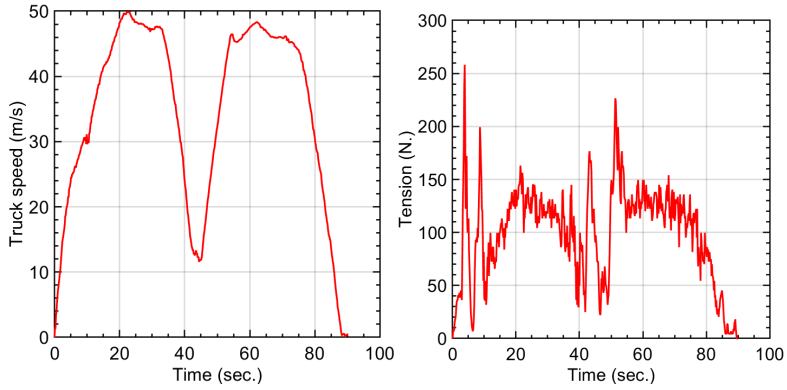

(e) Towing speed (f) Tether force

Figure 4.11: Data set from Test 7.

4.4 Data Analysis and Preprocessing

In this section, the preparation and pre-processing of the data measurements described in Section 4.3 will be addressed. These steps are necessary before feeding the data to the machine learning framework. In addition, an analysis of the sensitivity of the output tether force to changes in the input parameters was conducted.

4.4.1 Handling categorical variables

The input variables (features) in our framework are either numeric (of continuous or discrete domains), or categorical (of non-numeric values). A one-hot numeric array is used to encode the categorical variables (such as the motion type whose value belongs to $= \{\text{Steady, FigEight}\}$). The encoder input can be an array of possible values for the categorical features. Those feature values are encoded using a one-hot encoding (also known as "dummy" or "one-of-K" encoding). Each category is thus represented by a binary column.

4.4.2 Global sensitivity analysis

Sensitivity analysis (SA) is the study of how the output model uncertainty can be ascribed to different sources of input uncertainty [74]. This type of analysis is different from uncertainty quantification (UQ) which characterizes the output uncertainty of a model according to confidence bounds or an empirical probability density. That is, UQ seeks to address questions on how uncertain a model output is, while SA seeks to identify the key sources of this uncertainty, according to the input uncertainties. Also, SA is usually used for model reduction, making inferences about different aspects of the studied phenomenon, as well as and optimal design of experiments.

In general, sensitivity analysis may be performed locally or globally. For the local SA methods,the sensitivity of the model inputs is examined at a certain point in the

input space. On the other hand, the global SA methods find the sensitivities at multiple input-space points, and then compute some average measure of these sensitivities.

4.4.3 Feature ranking and selection

Outcomes of the global sensitivity analysis are usually used for feature subset selection. Essentially, feature selection methods seek to pick features that can make the learning outcomes more accurate, and eliminate irrelevant features that can lead to deterioration in model accuracy and quality.

Assuming statistical input independence, univariate feature selection methods examine features, one by one, to figure out the degree of strength of the relationship between each feature and the predicted output. One simple univariate method for investigating such relations is the Pearson correlation coefficient (PCC) method. This coefficient quantifies the linear correlation between two variables. The range of this coefficient is between -1 and 1, where $+1$ indicates positive correlation, 0 indicates no correlation, while -1 indicates negative correlation (i.e., as one variable increases, the other variable decreases).

The Pearson correlation coefficients were computed for all variable pairs using scikit-learn, the Python-based machine-learning module. A heat map was used to visualize the computed coefficients in Figure 4.12. The correlation values of all input variables with the predicted output tether force are shown in Table 4.3. Figure 4.13 shows an alternative bar-chart visualization of a subset of the heat-map data. The correlation results exhibit a stronger variability of the tether force with the height, towing speed, and one-hot encoded maneuver variables. These outcomes match our intuition, observations, as well as the experimental results given in Figure 4.3 for the maneuver-type variable and Figure 4.4 for the towing-speed variable.

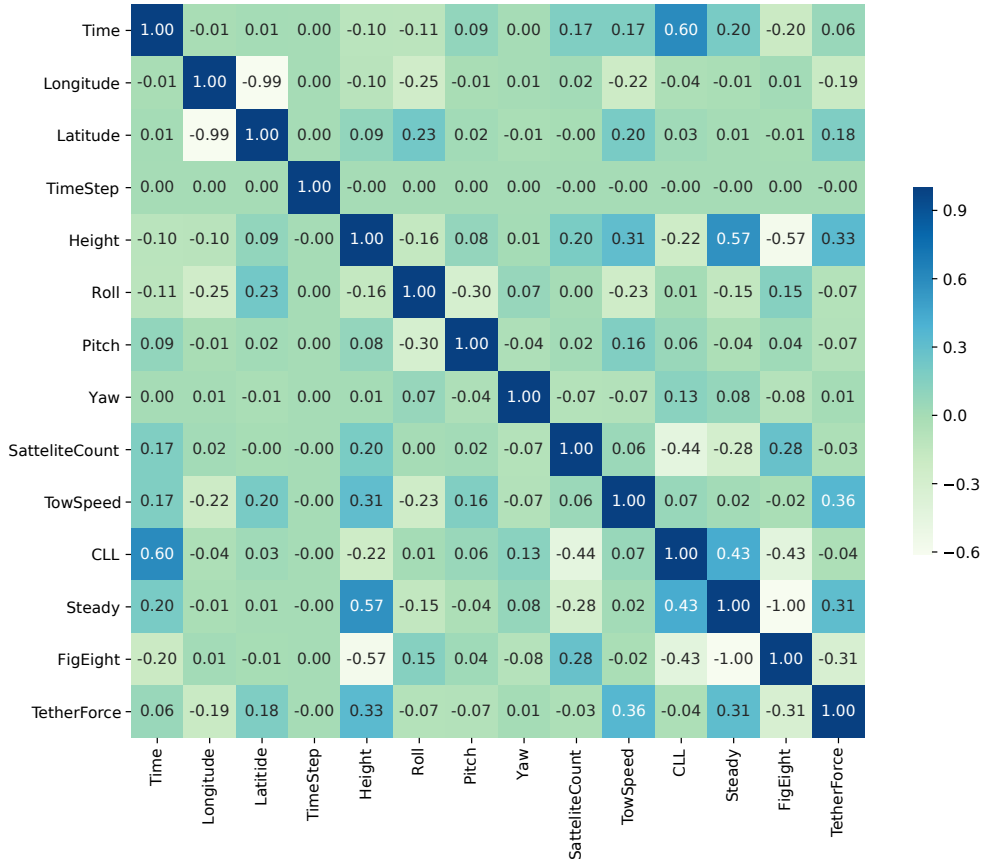

Figure 4.12: The Pearson correlation coefficient values for the towing test.

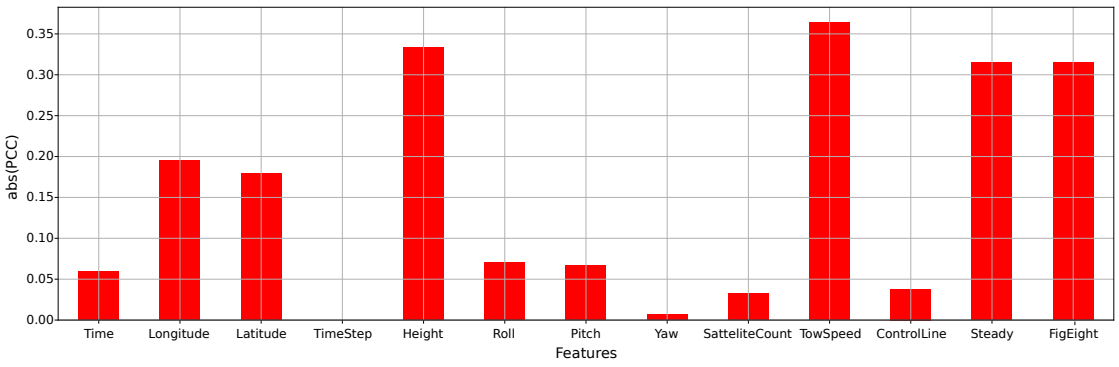

Figure 4.13: The absolute values of the Pearson correlation coefficient between the input features and the predicted output tether force.

To avoid the possibility of a high ranking for statistically dependent variables, the

pairwise correlation between the top-four features and the output tether force was evaluated. These correlation values are given in Table 4.4 and they generally indicate relative statistical independence. These results essentially indicate that the output tether force is primarily affected by those 4 features and that these features are highly uncorrelated. Thus, the effects of these four variables on the output are independent of each other.

Table 4.3: Pearson correlations between the output prediction (tether force) and different input features.

TetherForce	1.0000
TowSpeed	0.3643
Height	0.3330
Steady	0.3147
Latitude	0.1793
Time	0.0596
Yaw	0.0071
TimeStep	≈ 0
SatteliteCount	-0.0328
ControlLine	-0.0388
Pitch	-0.0662
Roll	-0.0704
Longitude	-0.1948
FigEight	-0.3147

Table 4.4: The pairwise Pearson correlation coefficients among the tether force and the top-correlated features.

	TetherForce	towSpeed	Height	Steady	FigEight
TetherForce	1.0000	0.3643	0.3330	0.3147	-0.3147
towSpeed	0.3643	1.0000	0.3082	0.0172	-0.0172
Height	0.3330	0.3082	1.0000	0.5684	-0.5684
Steady	0.3147	0.0172	0.5684	1.0000	-1.0000
FigEight	-0.3147	-0.0172	-0.5684	-1.0000	1.0000

It is important to mention that the representation of the correlation is considered as a preprocessing procedure of the ML project, based on the data only. If more correlation is needed, more data samples should be collected. In our case, the correlation is 0.35 which is in the medium range [0.25-0.55], so it is still acceptable. The important thing is that it shows the highly correlated features with the output as expected from the model-based sensitivity analysis, in the next section.

4.4.4 Model-based sensitivity analysis

To evaluate the sensitivity of the tether force to input parameter variations, the theoretical framework that was developed in [30] and later extended in [64, 75] was adopted . First of all, the tether force can be given by

$$F_{\mathrm{t}} = \frac{1}{2}\rho C_{\mathrm{R}} S v_{\mathrm{a}}^2, \tag{4.1}$$

where ρ is the air density, C_{R} is the resultant aerodynamic coefficient for the kite, S is the wing area, and v_{a} is the apparent wind velocity of the kite. The gravitational force affecting the kite is assumed to be negligible in comparison to the aerodynamic force. In the next analysis, the kite is assumed to be towed with a constant speed at a constant tether length under windless conditions. The wind speed relative to the towing truck speed is denoted by v_{w}. For a kite in a steady-flight mode, the apparent wind velocity of the kite is identical to the generated wind speed

$$v_{\mathrm{a}} = v_{\mathrm{w}} \tag{4.2}$$

and from Eq. (4.1), it could be found that

$$F_{\mathrm{t}} \propto v_{\mathrm{w}}^2. \tag{4.3}$$

For a kite flying with a crosswind maneuver, the apparent wind velocity is given by

$$v_a = v_w \cos\beta \cos\phi \sqrt{1 + \left(\frac{L}{D}\right)^2}, \tag{4.4}$$

where β is the elevation angle, ϕ is the azimuth angle, and L/D is the lift-to-drag ratio for the kite. Equation (4.4) follows from [75, Eq. (2.15)] as the special case with negligible gravitational force contributions and a constant tether length. This theoretical framework can be extended to account for the gravitational effects [75, Eq. (2.67)], but this is beyond the scope of our work. The term $\cos\beta\cos\phi$ represents the angular tether deviation from the wind speed vector generated by kite towing, while the square-root term is a scale-up term induced by the crosswind kite maneuver. For the kite, a higher lift-to-drag ratio leads to higher flight speed and apparent wind speed. By substituting Eq. (4.4) into Eq. (4.1), the tether force becomes

$$F_t \propto v_w^2 \cos^2\beta \cos^2\phi \left[1 + \left(\frac{L}{D}\right)^2\right]. \tag{4.5}$$

The parameters of this tether force model are related to the sensor data as follows. For a steady-flight kite, Eq. (4.3) shows that the tether force is only influenced by the wind speed v_w (TowSpeed) generated by kite towing. Also, this tether speed is kinematically coupled to the longitude, latitude, and time data. Due to the diagonal orientation of the runway (see Figure 2.6), the tether force should have roughly the same correlation value to the longitude and latitude. For the kite in a crosswind maneuver, Eq. (4.5) demonstrates an additional maneuver influence, as expressed by the factor $\cos^2\beta\cos^2\phi$. The amplification factor in brackets depends on the aerodynamic kite performance, which is not investigated as a variable in our work.

The above model [75] for a kite with a lift-to-drag ratio $L/D = 3$ will be illustrated. This ratio is typical for this kite size where an additional line drag is included. For a

crosswind maneuver at an elevation angle of $\beta = 60^\circ$, the tether force is amplified by a factor of 10 due to the aerodynamic term, while the maneuver term causes a reduction by a factor of $\cos^2 60^\circ = 0.25$. The combined effect is a maximum force increase by a factor of 2.5, compared to the steady-towing case. This increase can be generally observed in the measured tether forces of Figure 4.3.

4.5 Regression Model Construction

In this section, regression models of different types were constructed, to approximate the output tether force, and predict the generated power. Quality metrics are then used to assess the predictions.

4.5.1 Multivariate regression

Regression models seek to represent the relationship between input independent variables and output response variables, and use such a relationship for output prediction. The regression model accuracy depends on the types of the input and output variables as well as the model order. For example, in linear regression, a linear model is fit to known data points in order to minimize the sum of squared residuals between the measured output and the model predictions. Common regression models include linear models, neural networks, support vector machines, and decision trees.

In this work, several regression methods were considered like linear regression, neural networks, decision trees, and gradient boosting. Common statistical measures are used to compare the performance of these models under the same set of training data.

4.5.2 Quality measures

For evaluating the performance of the regression algorithms, the collected data was split into training and test subsets with 70% and 30% of the data samples, respectively (See Figure 4.14).

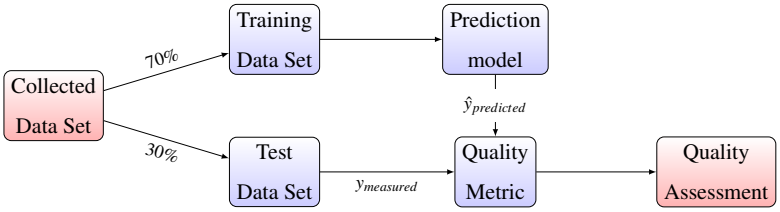

Figure 4.14: Assessing the performance of machine learning to build a predictive model.

Based on the regression model training, a model for predicting the tether force is obtained and tested. Then comparing the model predictions to the tether force measurements for the test data. This quantitative comparison is based on quality metrics, or cost functions. The quality metrics are optimized using iterative algorithms such as the gradient descent algorithm. Numerous quality metrics may be used for model assessment. Let $\hat{y}_i$ denote the predicted value of the i-th sample, and let y_i denote the corresponding true value, where n is the number of samples, and Var is the data variance. Then, the following quality measures or metrics were examined:

- **Mean Square Error:** This is the expected value of the squared error, which is given by

$$\text{MSE}(y,\hat{y}) = \frac{1}{n}\sum_{i=0}^{n-1}(y_i - \hat{y}_i)^2. \tag{4.6}$$

- **Coefficient of Determination** (R^2): This measure represents the proportion of the variance (of y) that is explainable by the independent model variables. Thus, this coefficient gives an assessment of the goodness of fit and how well unseen samples can be predicted by the fit model. The coefficient of determination can

be mathematically defined as

$$R^2(y,\hat{y}) = 1 - \frac{\sum_{i=1}^{n}(y_i - \hat{y}_i)^2}{\sum_{i=1}^{n}(y_i - \bar{y})^2}, \tag{4.7}$$

where $\bar{y} = \frac{1}{n}\sum_{i=1}^{n} y_i$ and $\sum_{i=1}^{n}(y_i - \hat{y}_i)^2 = \sum_{i=1}^{n} \varepsilon_i^2$. The highest possible value of this coefficient is 1. The coefficient can still be negative indicting that the suggested model is worse than the expected-value model in explaining the data. A constant model that always predicts the expected value of y, irrespective of the input features, would result in a coefficient of 0.

- **Maximum Residual Error:** This metric gives the worst-case error between the predicted and true values. For a perfect-fit regression model with a single output, this metric would have a value of 0 on the training set. The metric exhibits the maximum error extent for a fit model. This is metric is given mathematically as

$$\text{Max Error}(y,\hat{y}) = \max(|y_i - \hat{y}_i|). \tag{4.8}$$

- **Explained Variance:** The highest possible value of this metric is 1. Lower values of this metric indicate worse fit. The metric can be defined mathematically as:

$$\text{Explained Variance}(y,\hat{y}) = 1 - \frac{\text{Var}\{y - \hat{y}\}}{\text{Var}\{y\}}. \tag{4.9}$$

- **Mean Absolute Error:** This is the expected value of the absolute error loss. It is commonly called the l_1-norm loss, and is given by

$$\text{MAE}(y,\hat{y}) = \frac{1}{n}\sum_{i=0}^{n-1} |y_i - \hat{y}_i|. \tag{4.10}$$

4.6 Experimental Regression Results

The data collected from all seven tests and listed in Table 4.2 have been used in our experiments. Firstly, a basic neural-network models was tried and then compared their performance against multivariate regression models.

4.6.1 Neural-network regression models

Neural network models have been widely used due to their capabilities in modeling nonlinear mappings. An artificial neural network works in principle in a similar fashion to the biological neural networks of the human brain. In an artificial neural network, a "neuron" is a mathematical function that gathers and categorizes information based on some given architecture, in order to achieve certain tasks such as curve fitting and regression analysis.

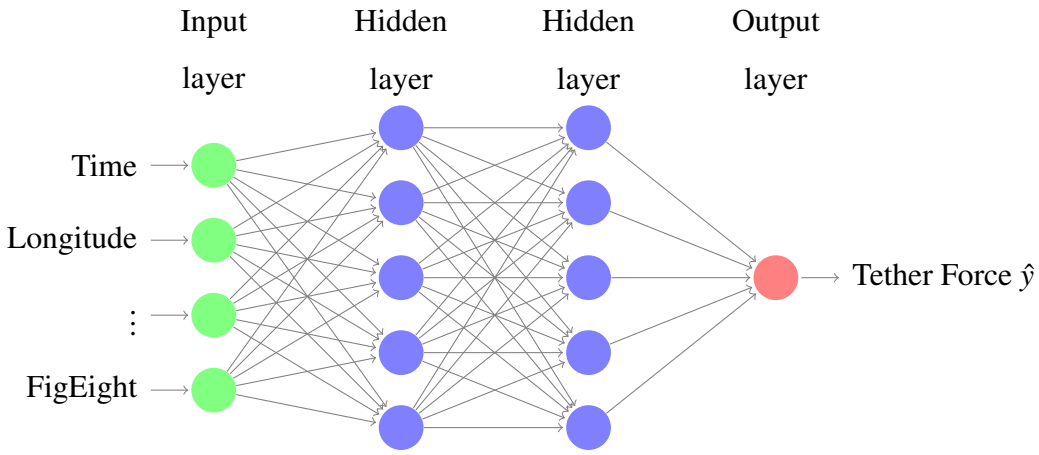

Figure 4.15: A neural network illustration of tether force prediction with two hidden layers.

In terms of architecture, a neural network contains layers of interconnected nodes. Figure 4.15 illustrates the tether force prediction problem as a neural network with 2 hidden layers. Each node is a perceptron and is similar to a multiple linear regression.

The perceptron feeds the signal produced by a multiple linear regression into an activation function that may be nonlinear. In a multi-layered perceptron (MLP), perceptrons are arranged in interconnected layers. The input layer collects input patterns. The output layer has classifications or output signals to which input patterns may map. In our work, our predicted output is the tether force. Hidden layers fine-tune the input weightings until the neural network's margin of error is minimal. It is hypothesized that hidden layers extrapolate salient features in the input data that have predictive power regarding the outputs.

Tensorflow and Keras [76] libraries were used to create a regression-based neural network with linear activation functions. For exploration, two hidden layers were used and they contain 12 and 8 neurons, respectively, over 500 optimization iterations (epochs, forward and backward passes). A model summary is reported in Table 4.5, followed by a visual highlighting the decreasing training and validation losses along epochs in Figure 4.16. Once the model is trained to a satisfactory error metric, it could be used for predicting tether force values of new input vectors. Figure 4.16 shows how the model is learning by representing the loss reduction over the epochs. Notice that, at the current stage of the research, there isn't any hyper-parameter tuning done yet. Thus, it could be possible to find a better solution, if the parameters were tuned in an optimized way.

Table 4.5: Keras model summary.

Layer (type)	Output Shape	Param #
Dense_9 (Dense)	(None, 12)	168
Dense_10 (Dense)	(None, 8)	104
Dense_11 (Dense)	(None, 1)	9

Total params: 281

Trainable params: 281

Non-Trainable params: 0

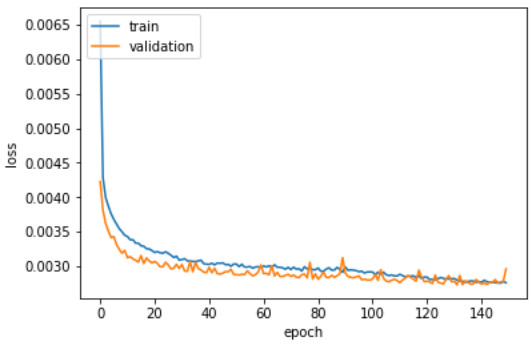

Figure 4.16: Neural network model loss performance.

4.6.2 Comparing regression models

To further demonstrate the value of machine learning regression models for an accurate prediction of the power output of airborne wind energy systems, a different standard regression models were evaluated per the quality metrics in Section 4.5.2, along with the training time. The standard Scikit Learn implementations was used. Results are reported in Table 4.6. For this study, the full data set was split into random train and test subsets, with ratio of 70% for training and the remaining 30% was saved for testing.

Table 4.6: Quality metrics of different regression models.

Model	MSE	Coef. of det.	max_error	Exp_Var	MAE	train_time
Voting Regressor	2733	0.678	573.46	0.678	32.41	0.437
Neural Network	3623	0.573	553.71	0.591	39.14	22.03
Gradient Boosting	3890	0.542	791.53	0.542	37.02	0.468
Decision Tree Regressor	4206	0.504	1005.66	0.504	30.29	0.062
Non-linear Regression	4709	0.445	671.06	0.445	43.16	0.031
Linear Regression	5487	0.354	702.99	0.354	49.38	0.000
Ridge Regression	5552	0.346	729.97	0.346	49.59	0.000
Lasso Regression	5557	0.345	731.64	0.345	49.61	0.000
Elastic Net Regression	6154	0.275	784.32	0.275	52.90	0.000
Adaptive Boosting	7211	0.151	496.41	0.260	62.99	0.156

A key remark at this point is that no one model scores best for all data sets in terms of all quality metrics. Multiple iterations and hyper-parameter tuning operations would be needed for further model optimization. The different trade-offs was highlighted in Table 4.6, e.g., between training time and accuracy [77].

For example, linear regression is one of the simplest algorithms trained using gradient descent (GD), which is an iterative optimization approach that gradually tweaks the model parameters to minimize the cost function over the training set. A linear model might not have the best accuracy but is simple to implement and hence is best of quick

domain exploration. It makes a prediction by computing a weighted sum of the input features, plus a constant called the bias term $\hat{y} = h_\theta(x) = \boldsymbol{\theta} \cdot \boldsymbol{x}$, where $h_\theta(x)$ is the hypothesis function and $\boldsymbol{\theta}$ is the model's parameter vector containing the bias term θ_0 and the feature weights θ_1 to θ_n.

Regularization is often used to further improve the loss function optimization. On the one hand, ridge regression is a regularized version of linear regression where a regularization term equal to $\alpha \sum_{i=1}^{n} \theta_i^2$ is added to the cost function. This forces the learning algorithm to not only fit the data but also keep the model weights as small as possible. The hyper-parameter α controls how much you want to regularize the model. If $\alpha = 0$, then ridge regression is just a linear regression. If α is very large, then all weights end up very close to zero and the result is a flat line going through the data's mean. On the other hand, Lasso regression is another regularized version of linear regression that adds a regularization term to the cost function, but uses the l_1 norm of the weight vector instead of half the square of the l_2 norm; like this $\alpha \sum_{i=1}^{n} |\theta_i|$. Lasso regression tends to completely eliminate the weights of the least important features (i.e., set them to zero), in other wards; automatically performs feature selection and outputs a sparse model (i.e., with few nonzero feature weights). Elastic net regression is a middle ground between ridge regression and lasso regression. The regularization term is a simple mix of both ridge and lasso regularization terms, and you can control the mix ratio r. When $r = 0$, elastic net is equivalent to ridge regression, and when $r = 1$, it is equivalent to lasso regression.

Despite their longer training times, nonlinear models are expected to perform better for our dataset though. As noticed in Figures 4.5 to 4.11, input features and output force are not linearly related. To start, polynomial regression introduces non-linearity by imposing powers of each feature as new features. It then trains a linear model on this extended set of features.

Alternatively, ensemble learning methods use a group of predictors, voting amongst

them for the best performance; and hence are often called voting regression. The accuracy of voting regression depends on how powerful each predictor is in the group and their independence. Finally, boosting refers to any ensemble method that combines several weak learners into a strong learner. The general idea of most boosting methods is to train predictors sequentially, each trying to correct its predecessor, often resulting in the best performance, compared to individual models.

Per these machine learning experiments, it could be concluded that there is a clear success of a neural network model applied to AWE for predicting tether force, even without hyper-parameter tuning. The main model drawback is that it takes a longer training time than other algorithms, despite its overall accuracy performance.

A major advantage for this ML model is cost. Once a model is trained, there is no need to physically run new experiments (with the same test setup, as shown in Figure 2.7, to predict the tether force. Instead, it could easier to rely on the current NN model to predict the estimated tether force for new input combinations. The gradient boosting model could be used, if the concern is about evaluation/prediction time, rather than model accuracy. Note that the evaluation time is the time required to calculate the predicted tether force from our model (prediction formula). The neural network generates a more accurate formula, but also more complex and takes more time for evaluation.

4.7 Conclusions and Future Work

This work demonstrated a novel approach to employ machine learning regression methods for the prediction of the power generated by AWE systems. Using an experimental kite system designed at Kyushu University, a seven design scenarios of different input specifications were orchestrated . Using the experimentally-collected numerical and categorical data from multiple sensors helps in constructing multivariate regression models to predict the generated tether force.

- The sensitivity analysis results have validated our intuitive understanding of measurement ranking in impacting the predicted tether force, and hence the generated power.
- The performance of different ML algorithms was assessed, including neural networks, linear regression, and ensemble methods, in terms of training time and different accuracy metrics. Different regression algorithms resulted in different performance scores, emphasizing the need for further studies around the training data set and hyperparameter tuning.
- This preliminary investigations highlighted the potential of ML modeling methods in predicting tether force and traction power in AWE applications.

It is important to highlight that this is the first attempt within the AWE community to employ machine learning. In other words, there is no previous studies within the AWE that apply machine learning to AWE problems.

In future work, it is beneficial to leverage the significance of height and type of motion (steady flight and figure-of-eight flight maneuvers) to the accuracy of the multivariate regression models into exploring new trajectories for improved/optimal power generation. Furthermore, there will be also an attempt to overcome different types of measurement errors by improving the data collection procedures by including:

- the steering actuation of the KCU, either directly measured as a linear motion of the control lines, or derived from the rotation of the motor,
- the apparent wind speed at the kite,
- the angle of attack of the apparent wind velocity vector with the wing, and
- the side slip angle of the apparent wind velocity vector with the wing.

Also, it is beneficial to use the information gained from the current ML models to actively determine optimal deployment locations for AWE systems.

Chapter 5

Optimal Transition for a VTOL Rigid Aircraft

Contents

This chapter aims to formulate and solve the transition phase of a VTOL rigid aircraft as an optimal control problem (OCP). The main novelty of this part is introducing the optimal trajectory of the aforementioned transition phase based on a satiable desired cost function, which is minimizing the power consumption, to the AWE community.

This minimization of energy will cause a reduction in the total mass of the airborne component (especially battery) and this leads to enhancement in the flight operation. Also, achieving the required thrust to perform the transition, will help in modifying the AP-2 aircraft.

5.1 Introduction

AWE systems are obviously evolving rapidly and will cover a significant share of wind energy consumption. It might be expected that this will happen in a few years' time, based on the rapid progress in AWE technology and the continuous flow of research funds in recent years [25]. Cherubini et al. [27] claim that the AWE research community is burgeoning in a fast way, indeed. They point out that the AWE community is divided evenly between academia (where many of the world's finest technical universities are involved), and industry (where decades-old companies face strong competitiveness by the new start-ups). The review of Cherubini et al. [27] offers a thorough overview/classification of evolving different AWE systems as well as lists of the most influential universities and companies currently working on the implementation of such systems. A summary of the patents and scientific papers produced/published within the AWE domain is given in [28]. One of the major points of discussion in AWE systems is the launch paradigm; in particular, vertical take-off and landing (VTOL) [78–83], as shown in Figure 1.11.

5.1.1 Launching problem

A main challenge for AWE technology is how to automate the launching and landing procedures for wing kite power systems (KPS), whether they are flexible (Figures 5.1, 5.2 and 5.3) or rigid (Figure 5.4). Such procedures must be robust and reliable under different weather conditions. In the case of flexible wings/soft kites, these requirements

are a significant issue by cause of the proportional relation between the kite area and the generated power. Some attempts are made to solve this problem by connecting the kite to a quad-copter that drags it to the operating altitude [78, 84]. This approach has many benefits, including the feasibility of launching in an arbitrary direction, that the setup time is satisfactorily small, and that no additional infrastructure needed. However, with bigger kites, which have high non-uniformly distributed weights, this approach remains partly ineffective. This could be solved by using extra numbers of quad-copters, but this will lead to a complex swarm robotics problem that must be solved to secure the connections among the quad-copters and the way they will work together in unison serving a specific same goal at every certain point in time [85]. Practically, a lot of companies like Makani, E-kite, Twing Tec, Kitemill [65, 86] and Skypull SA [79] chooses the rigid wing concept to make the process of VTOL easier. Several papers by Fagiano and his associates [79–83] deal with important issues concerning the VTOL paradigm. Of paramount importance is the point of transitions experienced by the AWE flying device from a hovering mode (where it acts as a multi-copter) to a forward flight mode (where it acts like an airplane), and vice versa. For take-off and landing phases, the AWE flying device uses multiple rotors to hover, while in the phase of power generation, the flying device utilizes the aerodynamic forces generated from its wings for flying as a conventional airplane. How to model and simulate the transition from one mode to another is a crucial aspect from the control design standpoint.

(a) First step (b) Second step (c) Third step

Figure 5.1: Mast launching for soft kites (a) kite is hanged upside down, (b) wind lifts the kite when the mast is going up, and (c) tether is reeled out [13].

Figure 5.2: Rotational Launch: Kite is connected to a rotating arm, as soon as take-off speed is reached the tether/kite is released [14].

Figure 5.3: Telescopic Mast: Arm extends and lift the kite to a certain altitude [15].

Figure 5.4: Catapult Launch for rigid wing aircrafts, where the system is accelerated using a linear motor [16].

The rest of this chapter is set out as follows. Section 5.2 offers a description of the complete power cycle of the pertinent AWE aircraft and identifies this cycle to consist of three phases, namely: VTOL, transition, and flight mode. Out of these three phases, the transition phase is selected for investigation, simulation, and control within the current chapter. Section 5.3 builds a mathematical model for the AWE aircraft being studied by defining the aerodynamic forces and moments that impact it, and by writing down its kinetic equations using the usual/typical formulation of optimal control problems. Such equations are carefully verified/tested for dimensional homogeneity [87]. Next, in Section 5.4, the equations are solved using a software that transforms the underlying optimal control problem (OCP) into a static optimization problem. This section also reports/shows and discusses the obtained results. Section 5.5 concludes the chapter.

5.2 Overview of the Full Power Cycle

The utmost target of our ongoing work/research is to simulate and control the dynamic model of a VTOL rigid aircraft, which is connected to a tether making a pumping cycle for the sake of power generation. However, in this chapter, the main aim was limited to simulating and controlling the aircraft within the transition phase, only. The model for aircraft simulation represents the AP-2 aircraft produced by the company Ampyx Power [53, 54, 68]. The AP-2 aircraft was not originally designed for VTOL, but it was targeted to check what will happen if it will be incorporated with vertical takeoff-landing capabilities to the aircraft. It was assumed that there are 4 propellers mounted in the shape of a conventional quad-rotor, so that the aircraft's behavior should be similar to a tail-sitter aircraft, i.e., a VTOL aircraft that takes off and lands on its tail, then rotates to the horizontal to perform forward flight [88]. Also, it was assumed that it is possible to fold the aircraft rotors or propellers. Table 5.1 summarizes the important aircraft parameters, moreover, a visualization of the AP-2 aircraft is represented in Figure 5.5.

Figure 5.5: A photograph of the AP-2 aircraft developed by Ampyx Power [17].

Table 5.1: Aircraft parameters

Parameter	Symbol	Value	Units
Aircraft mass	m	36.8	kg
Inertia	$I_{x,y,z,xz}$	25, 32, 56, -0.47	$kg\ m^2$
Wing Area	S_w	3	m^2
Wing span	b	5.5	m
Mean chord	$\bar{c}$	0.5	m
Aspect ratio	AR	10	–

To give the reader a quick sight of the overall picture, it will be shown that the operation of the full/complete power cycle (Figure 5.6) is divided into three phases/stages:

1. **VTOL mode:** The aircraft utilizes the thrust produced from the 4 propellers to go up vertically. This phase could be modeled by the quad-copter equations (neglecting the contribution of the drag that comes from the fuselage in addition to the tether effect). The key challenge within this phase is that the fuselage of the aircraft is facing the crosswind which presents a question of stability (the wind

stream directly hits the horizontal tail and causes a moment that rotates the aircraft). This leads to some requirements to control the rotors, they must be fast enough to adjust any disturbance and keep the aircraft on its vertical path.

2. **Transition mode:** The aircraft accelerates and rotates quickly enough to reach the height and reference speed that will sustain its weight during the upcoming flight stage. Capturing the optimal operation point, is the key challenge within this phase, as the transition path should be smooth enough, and there is no lift loss during the turning/rotation. In addition, the controller must respond quickly to give the specific deflections that cause a smooth path, after overcoming the disturbances from the crosswind. The formulation of the current phase could be a standard optimal control problem (OCP). Choosing an appropriate cost function is a very essential matter, in our case, the reasonable one is minimizing power.

3. **Flight mode:** The propellers could be folded and the aircraft performs similar to a glider following the prescribed figure-of-eight path, based on the modular control strategy developed by Rapp et al. [65, 86].

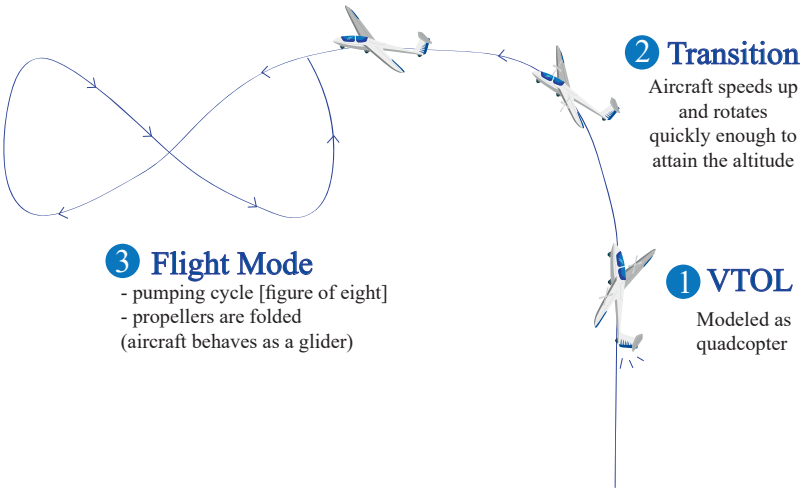

Figure 5.6: Schematic summary of the phases of the full power cycle phases [18]. The plane rendering is from http://freepik.com.

5.3 Transition Phase

Any transition phase usually contains some difficulties within the formulation procedure, in addition to solving it. In the aerospace field, there are some papers deals with the transition phase from hovering to forward flight for different types of unmanned aerial vehicles (UAVs) using different control techniques [88–92], and, for a tail-sitter UAV, there is solutions for the reverse-way transition from forward flight to hovering [92]. Moreover, for a flapping vehicle, [93] there is a paper in which the authors simulates the transition phase using optimal control with the aim to minimize the time interval during this phase [94]. In this section, a mathematical model that captures the essence of the transition phase from hovering to forward flight will be shown. Starting with modelling the longitudinal flight in the next subsection, after that representing the aerodynamic forces and moments. Then introducing the optimal control formulation for this problem.

5.3.1 Mathematical model of the VTOL aircraft

The mathematical model of a rigid-wing aircraft can be obtained using the six-degree-of-freedom equations of motion (EOM) that are used for modeling a conventional aircraft, i. e.,

$$m\dot{\boldsymbol{v}}^B = \boldsymbol{F}_a^B + \boldsymbol{F}_g^B - m(\boldsymbol{\omega}^B \times \boldsymbol{v}^B) \tag{5.1}$$

$$\boldsymbol{I}\dot{\boldsymbol{\omega}}^B = \boldsymbol{M}_a^B - (\boldsymbol{\omega}^B \times \boldsymbol{I}\boldsymbol{\omega}^B) \tag{5.2}$$

where the vector equation (5.1) represents the translational force and the vector equation (5.2) represents the angular momentum, both expressed in the body frame. The aircraft is subjected to an aerodynamic force $\boldsymbol{F}_a^B = [F_x, F_y, F_z]^T$, a gravity force $\boldsymbol{F}_g^B$ and

an aerodynamic moment $\boldsymbol{M}_a^B = [L,M,N]^T$. Equations (5.1) and (5.2) in conjunction with equations for the rate of change of angular position and the rate of change of transnational position lead to the famous 12 equations for modeling a conventional aircraft. For steady conditions, the longitudinal and lateral dynamics could be decoupled. For simplicity, the focus will be on the longitudinal dynamics, which are represented by 4 equations, namely the rate of change of each of the axial velocity, the vertical velocity, the rotational velocity around the y-axis and the pitch angle.

$$\dot{u} = \frac{F_x}{m} - g\sin\theta + rv - qw \tag{5.3}$$

$$\dot{w} = \frac{F_z}{m} - g\sin\phi\cos\theta - ru + pw \tag{5.4}$$

$$\dot{q} = [M - (I_x - I_z)pr - I_{xz}(p^2 - r^2)]/I_y \tag{5.5}$$

$$\dot{\theta} = q\cos\phi - r\sin\phi \tag{5.6}$$

where F_x is the aerodynamic force in the x-direction in addition to the thrust force, g is the gravitational acceleration constant $\approx 9.81[m/s^2]$, $[u,v,w]$ are the velocity components in the x, y and z directions, respectively, $[p,q,r]$ are the angular velocities around the x, y and z axes, and $[\phi,\theta,\psi]$ are the roll, pitch and yaw angles, respectively. To assure full definition of the previous equations, the aerodynamic model of this aircraft, which will define the aerodynamic forces and moments, will be presented.

The aerodynamic forces and moments are defined in the body frame as follow:

$$\boldsymbol{F}_a^B = \frac{1}{2}\rho V^2 S_w \begin{bmatrix} C_X \\ C_Y \\ C_Z \end{bmatrix} \tag{5.7}$$

$$M_a^B = \frac{1}{2}\rho V^2 S_w \begin{bmatrix} b\,C_l \\ \bar{c}\,C_m \\ b\,C_n \end{bmatrix} \tag{5.8}$$

where $\rho \approx 1.225 kg/m^3$ is the air mass density, $V = \sqrt{u^2+v^2+w^2}$ is the aircraft speed, C_X, C_Y, C_Z and C_l, C_m, C_n are the non-dimensional body axes aerodynamic force and moment coefficients, respectively. It is common in the aerodynamic field to approximate the aerodynamic coefficients by linear terms in their series expansions [53,54,65,68,86]

$$C_X = C_{X_0} + C_{X_q}\left(\frac{\bar{c}q}{2V}\right) + C_{X_{\delta_e}}\delta_e \tag{5.9}$$

$$C_Y = C_{Y_\beta}\beta + C_{Y_p}\left(\frac{bp}{2V}\right) + C_{Y_r}\left(\frac{br}{2V}\right) + C_{Y_{\delta_a}}\delta_a + C_{Y_{\delta_r}}\delta_r \tag{5.10}$$

$$C_Z = C_{Z_0} + C_{Z_q}\left(\frac{\bar{c}q}{2V}\right) + C_{Z_{\delta_e}}\delta_e \tag{5.11}$$

$$C_l = C_{l_\beta}\beta + C_{l_p}\left(\frac{bp}{2V}\right) + C_{l_r}\left(\frac{br}{2V}\right) + C_{l_{\delta_a}}\delta_a + C_{l_{\delta_r}}\delta_r \tag{5.12}$$

$$C_m = C_{m_0} + C_{m_q}\left(\frac{\bar{c}q}{2V}\right) + C_{m_{\delta_e}}\delta_e \tag{5.13}$$

$$C_n = C_{n_\beta}\beta + C_{n_p}\left(\frac{bp}{2V}\right) + C_{n_r}\left(\frac{br}{2V}\right) + C_{n_{\delta_a}}\delta_a + C_{n_{\delta_r}}\delta_r \tag{5.14}$$

Using a second-degree polynomial function to define the aerodynamic derivatives in terms of the angle of attack (α), i.e. $C(\alpha) = c_0 + c_1\alpha + c_2\alpha^2$. For example to fully define equation 5.9, it is noted that all the derivatives for AP-2 used below are available [53, 54, 68]

$$C_{X_0} = C_{X_{00}} + C_{X_{0\alpha}} \cdot \alpha + C_{X_{0\alpha^2}} \cdot \alpha^2$$
$$C_{X_q} = C_{X_{q0}} + C_{X_{q\alpha}} \cdot \alpha + C_{X_{q\alpha^2}} \cdot \alpha^2$$
$$C_{X_{\delta_e}} = C_{X_{\delta_e 0}} + C_{X_{\delta_e \alpha}} \cdot \alpha + C_{X_{\delta_e \alpha^2}} \cdot \alpha^2$$

5.3.2 Optimal control problem formulation using direct method

In this subsection the OCP will be formulated using direct method [95]. The system of equations (5.3-5.6) could be written in abstract form as

$$\dot{\boldsymbol{x}} = \boldsymbol{f}(\boldsymbol{x}, \boldsymbol{u}) \tag{5.15}$$

where the state vector $\boldsymbol{x} = [u, w, q, \theta]^T$ and $\boldsymbol{u} = [\delta_e, F_T]$ represents the control actions, where F_T is the thrust force. The optimal control problem is to find a piecewise continuous control action $\boldsymbol{u}(.) : [0, t_f^*] \rightarrow \Theta$ (admissible control set), that steers the system (5.15) from the hovering state to the forward flight state, using minimum energy. Choosing the objective of the optimal control problem to be the minimization of energy consumption. Clearly this is because the target is to generate energy, which means minimizing energy loss at each phase as much as possible, so that the net energy production will be higher. The cost function could be represented as follows:

$$\min_{\boldsymbol{u}(.)} J = \int_0^{t_f} u^T u \, dt \tag{5.16}$$

Also, for the sake of comparison, also results for the minimal-time problem will be presented, which is another minimization problem with a cost function represented as follows:

$$\min_{t_f} J = \int_0^{t_f^*} dt \tag{5.17}$$

For more comparison, lets modify the min. power cost function to be $\min_{\boldsymbol{u}(.)} J = N\int_0^{t_f^*} u^T u\ dt$. The solution will be represented for N=1.0, 1.7, 0.2 cases which indicate min. power, non-optimal (1), and non-optimal (2) respectively. Hence that the two important cases are the min. power and min. time cases. Their results are presented in details in [18].

The initial and final conditions could be achieved by solving the nonlinear trim condition $\dot{x} = 0$. The initial state is defined as follows

$$\boldsymbol{x}(t_0) = [u_0, w_0, q_0, \theta_0] = [0, 0, 0, \frac{\pi}{2}] \tag{5.18}$$

The aircraft, which is a tail-sitter, performs a hovering flight at this state, so there is no axial, vertical or rotational velocity. Also, the aircraft nose is upward, so the pitch angle is equal to 90°. There is still one remaining condition to sustain the aircraft at the hovering state without falling, which is that forces in the x direction should be equal (including thrust force) to the aircraft's weight.

The final state is defined as follow

$$\boldsymbol{x}(t_f^*) = [u_f, w_f, q_f, \theta_f] = [15, 0, 0, 0] \tag{5.19}$$

At this state, the aircraft performs a normal forward flight, so there is some non-zero value for the axial velocity and the remaining parameters are each equal to zero. In the forward flight condition, the aim was to find x such that the inertial forward speed is 15 m/s and $V_z = 0$.

The control action exerted by the elevator is bounded, due to the physical limitation

$$-30^\circ < \delta_e < 30^\circ \tag{5.20}$$

There is not any limitation on the thrust force, except that our target is to find the mini-

mum energy consumption. The thrust force will be a design parameter in modifying the AP-2 to perform VTOL. Also, there isn't any path constraints.

5.4 Solution and Results of the Optimal Control Problem

The optimal control problem represented in the last section is then solved using the Imperial College London Optimal Control Software (ICLOCS) [96–98]. This is a MATLAB-based software, which allows users to define optimal control problems with general path and boundary constraints, and free or fixed final times [96]. The code also allows users to include constant design parameters as unknowns. As an opening to its primary function, the ICLOCS software transforms the given optimal control problem to a static optimization problem using two methods, namely, direct multiple shooting or by direct collocation [96]. The direct multiple shooting formulation requires the solution of initial value problems (IVPs) of ordinary differential equations (ODEs), while the direct collocation formulations discretize the system dynamics using implicit Runge-Kutta formulas [99, 100]. Once the optimal control problem has been transcribed as a static optimization problem, it can be solved with a prudent choice of nonlinear constrained optimization algorithms, e.g., by using the open source non-linear programming (NLP) solver called Interior-Point OPTimizer (IPOPT) [101–103] or MATLAB's own NLP solver, namely its function fmincon [104, 105]. The derivatives of the underlying ODE right-hand side, cost and constraint functions are estimated numerically herein since they are required for the ICLOCS solution of the optimization problem. The discretized dynamical system of the optimal control problem is solved initially for an educated guess of the final time. The IPOPT solver continues to tackle the discretized problem until it reaches the minimum value of the consumed energy (5.16), or the minimum value of the final time (5.17), and then it terminates. The minimum consumed

energy would correspond to the maximum net energy gained, while the minimum final time would represent the minimum/optimal time at which the transition between hovering and forward flight takes place.

Simulation results are presented in Figures 5.7–5.14. Figures 5.7–5.10 represent the time history of the system states. Figures 5.11–5.12 represent the optimal control action variations with time. Finally, Figure 5.14 represents the optimal path/trajectory. The optimal control problem was solved for the two cases denoted by the objective functions (5.16) and (5.17), namely:

- **Minimizing time**; with the cost function being represented by equation (5.17). In this case the flight endurance is minimized; $t_f^* = 2.7$ s.
- **Minimizing power**; with the cost function being represented by equation (5.16). In this case our target is to minimize the power expenditure, without any restriction on the flight endurance; $t_f = 5.825$ s.

The 2$^{\text{nd}}$ case is more reasonable for our current application, as the target is seeking the maximum net gain of power, i.e., maximizing the difference between wind-generated power and power consumption or expenditure by the flying vehicle during flight, which amounts to minimizing this power consumption.

Figure 5.7 represents the time history of the 1$^{\text{st}}$ state, namely; the axial velocity u, which is the velocity in the direction of the nose of the aircraft. At the start, while the vehicle is in the hovering mode and behaves as a multi-copter, the value of the axial velocity is zero and its direction is upward in the global axes. For *minimizing time* case; the aircraft's axial speed increases very fast, with a high slope and quickly exceeds the desired final axial velocity $u_f = 15$ m/s. After that it decreases until it saturates at u_f. For *minimizing power* case; the axial velocity increases to 6.4 m/s in the first 1.1 s, after that it decreases to zero at 3 s. Then the axial velocity increases until it saturates directly at u_f, without any fluctuation around the final state.

Figure 5.8 represents the time history of the 2nd state variable, namely; the vertical velocity w. At the start, at the hovering state $w(0) = 0$ m/s, and at the final state $w(t_f) =$ 1.1 m/s. For *minimizing time* case; the vertical velocity is almost zero in the beginning for 0.34 s, after that it starts to decrease until it reaches its summit at 2.106 s, the point of time that corresponds to the summit of the angular velocity q. Then the vehicle is approximately performing a forward flight and the vertical velocity w starts to increase until it saturates at the final state w_f. For *minimizing power* case; in the beginning for 2.33 s the vertical velocity w fluctuates around zero. After that it starts to increase until almost 4.54 s, at which the aircraft starts to perform forward flight. Then the vertical velocity w decreases and saturates at its final state.

Figure 5.9 represents the time history of the 3rd state variable, namely; the angular velocity q. It begins with a zero value at the hovering state, after that its value changes during the flight and returns to zero at the end. For *minimizing time* case; like the vertical velocity, the angular velocity is approximately zero for the beginning 0.34 s,after that it starts to decrease until it reaches its minimum at 2.106 s, at which point the vehicle begins to perform forward flight; acting as an aircraft. Then the angular velocity begins to increase and returns to zero with some overshooting. For *minimizing power* case; in the first 3 s the angular velocity q is a bit below zero. After that it decreases until almost 4.66 s, within the region at which the aircraft begins to perform forward flight. Then the angular velocity q increases and saturates at zero.

Figure 5.10 represents the time history of the 4th state variable, namely; the pitch angle θ. As the aircraft is a tail-sitter and hovering at the beginning, so the pitch angle is equal to 90°. After that the aircraft rotates until the trim conditions are reached at the final state. For *minimizing time* case; the aircraft approximately remains at 90° within the first 0.59 s. After that, the aircraft rotates in quickly, as it turns from 90° to 10° in almost 1.55 s only. At the end, it makes a small fluctuation around its final state before it saturates. For *minimizing power* case; the aircraft approximately remains at 90° in

the first 0.815 s. After that it rotates gradually until reaching the final state with small fluctuation.

Figure 5.11 shows the non-dimensional thrust variation with time. For *minimizing time* case; this thrust is characterized by sudden, abrupt, and bang-bang changes. The non-dimensional thrust remains at the same value for 1.9 s, then it goes suddenly to zero for 0.6 s. For *minimizing power* case; the non-dimensional thrust makes some ups and downs until it saturates at almost zero at the final state; a reasonable behavior as the aircraft should start to behave as a glider.

Figure 5.12 shows the elevator deflection variation with time. For *minimizing time* case; similarly to the non-dimensional thrust, the elevator deflection follows a bang-bang fluctuation between two crisp bounds. The elevator deflection remains at 30° for the first two seconds, then it goes suddenly to -30° for 0.4 s. For *minimizing power* case; the elevator deflection fluctuates between -25° and 25° until 4.54 s, then it goes to -20° at the final state.

Figure 5.13 shows the non-dimensional power variation with time. For *minimizing time* case; the aircraft exerts a huge amount of power in the first 2 s, aiming to make the turning as fast as possible. For *minimizing power* case; the power values vary between 0 to 3, with most of the power exerted within the first 3 s. Note that the left vertical axis values are for the minimum time and the right vertical axis values are for the minimum power. For the *non-optimal (1)* and *non-optimal (2)* cases, the consumed power was very high and fluctuating over the time history.

Figure 5.14 shows the optimal path/trajectory from hovering to forward flight. For *minimizing time* case; the aircraft spends around 7 m hovering and rising up, after that spends another 15 m of height to turn. For *minimizing power* case; the aircraft spends 12 m hovering and rising up while rearranging its orientation. Then the aircraft makes a forward flight without gaining any additional height.

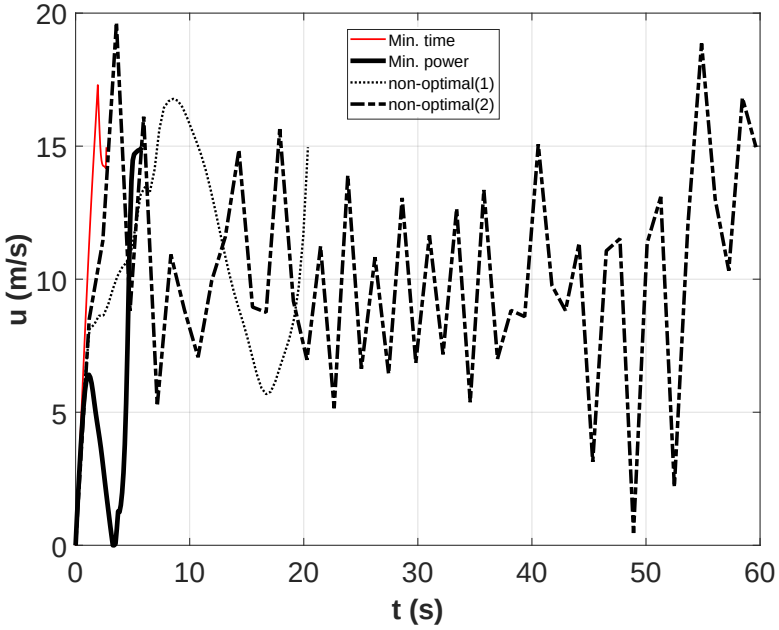

Figure 5.7: Axial velocity u versus time, for the represented 4 cases.

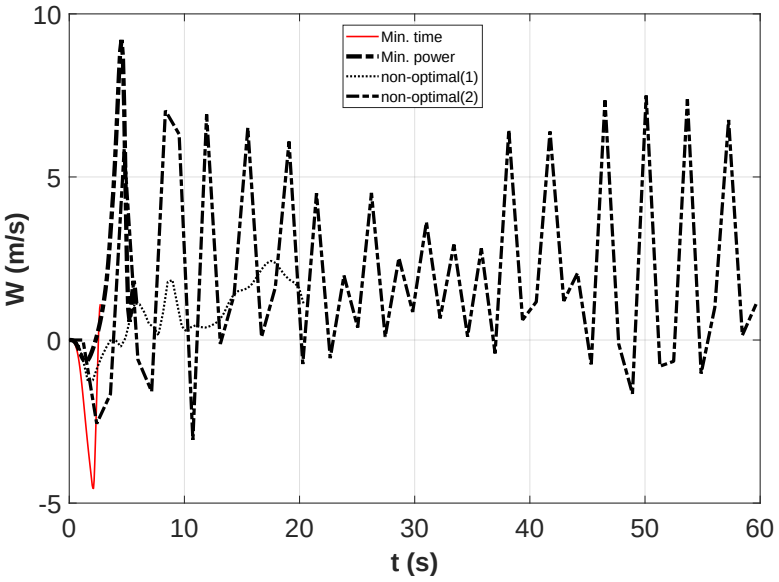

Figure 5.8: Vertical velocity w versus time, for the represented 4 cases.

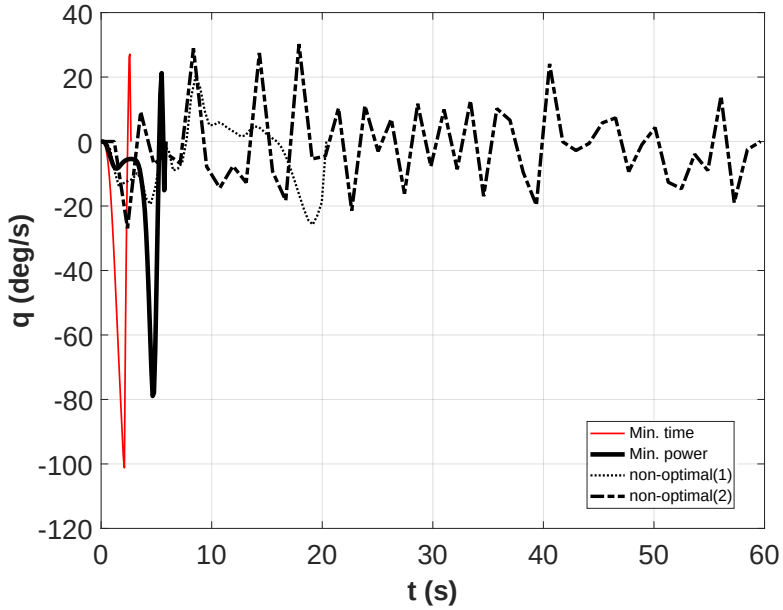

Figure 5.9: Angular velocity q versus time, for the represented 4 cases.

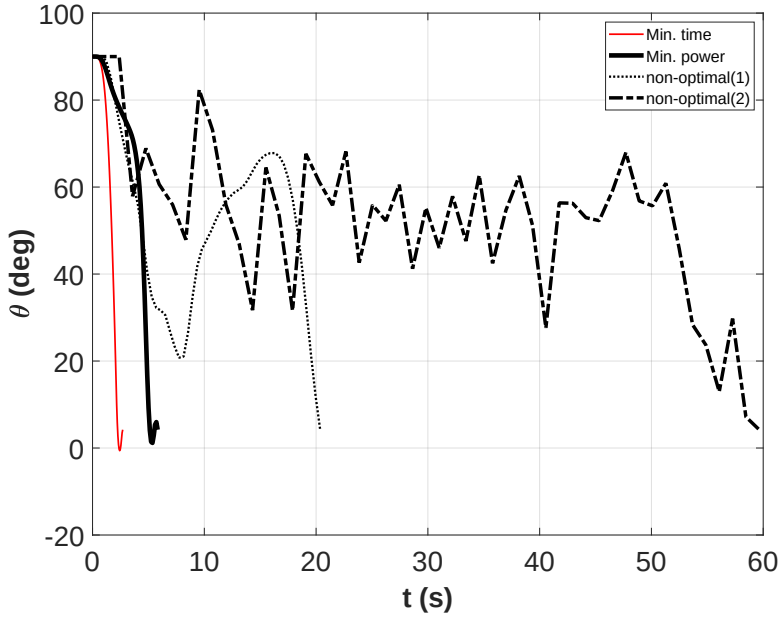

Figure 5.10: Pitch angle θ versus time, for the represented 4 cases.

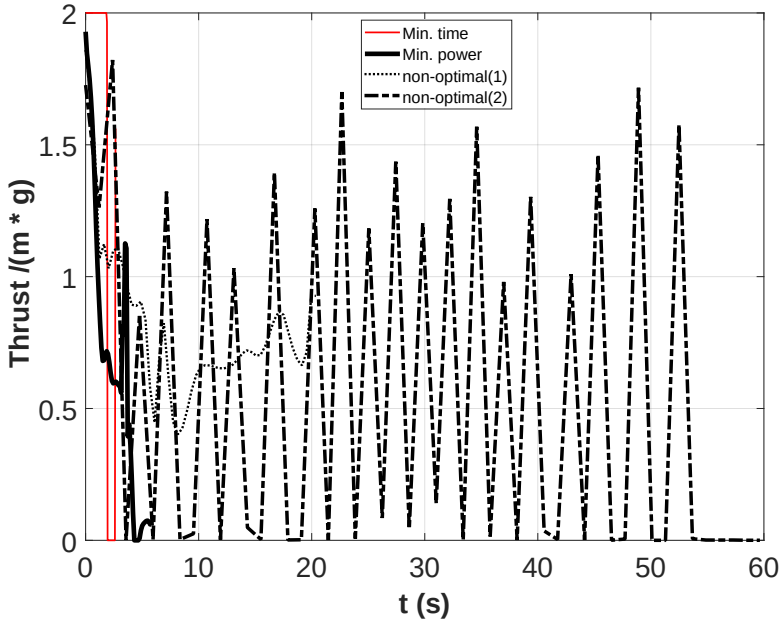

Figure 5.11: Non-dimensional thrust versus time, for the represented 4 cases.

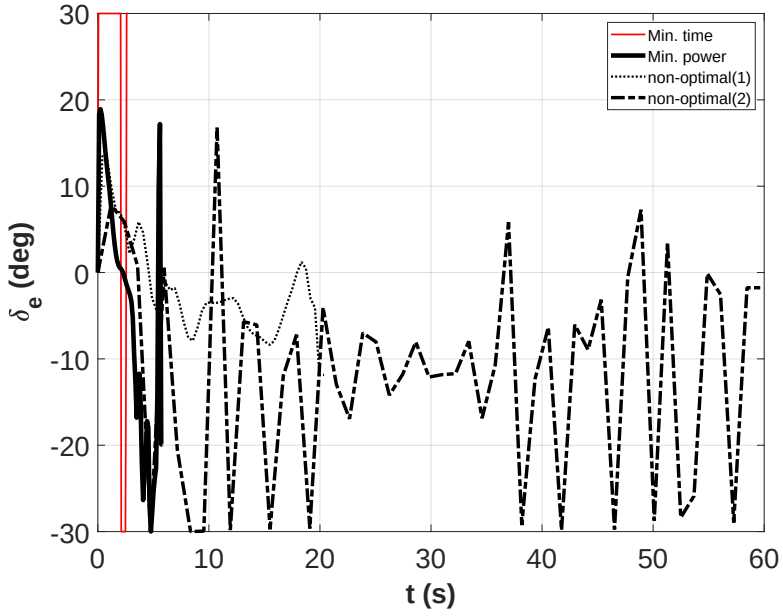

Figure 5.12: Elevator deflection δ_e versus time, for the represented 4 cases.

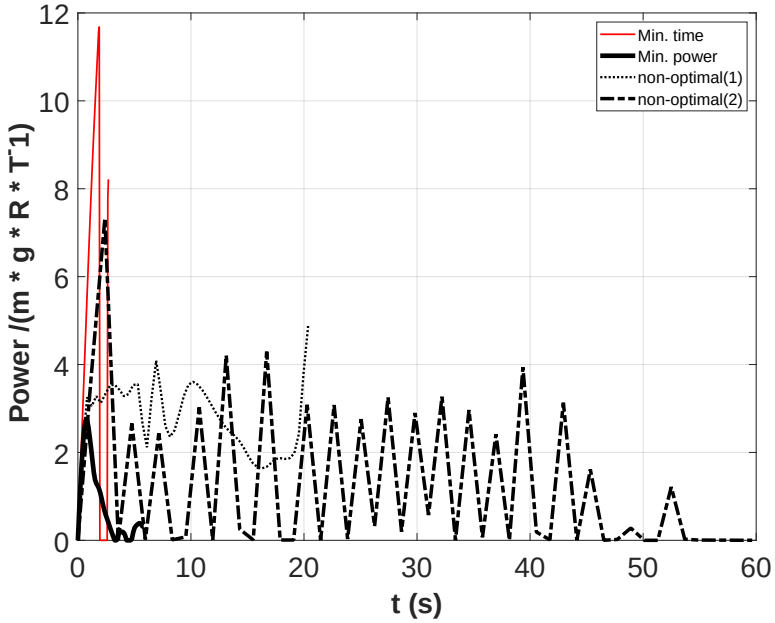

Figure 5.13: Non-dimensional power versus time, for the represented 4 cases.

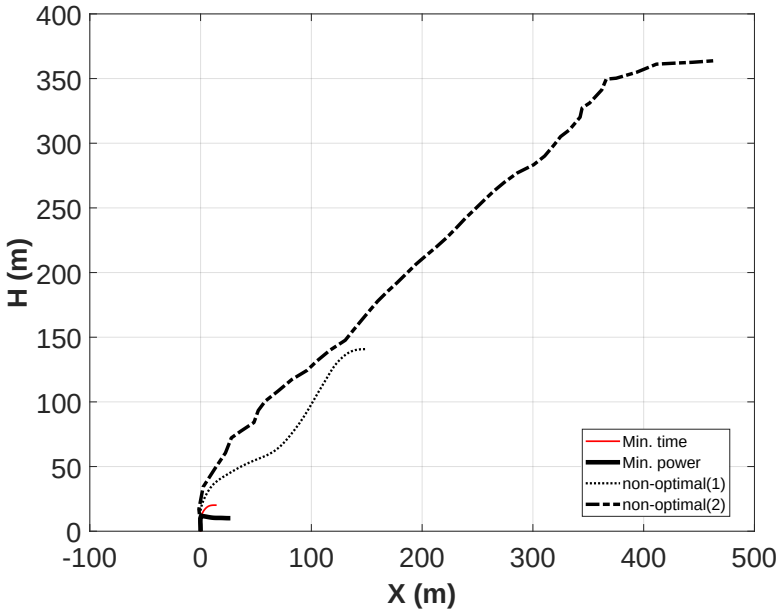

Figure 5.14: Optimal trajectory/path from hovering to forward flight, represented by height (z axis) versus x axis, for the represented 4 cases.

It could be noticed in all previous figures that the minimum time case always ends

first but with more power expenditure, mainly shown in Figure 5.13. It is clear that the target is seeking power production, so wanting to minimize power consumption. Choosing the optimality criterion to be minimizing power is reasonable, and that makes the second case of minimizing time is not optimal from the perspective of the first case. The two non-optimal cases shows that more power consumed, as shown in Figure 5.13. The results summary is listed in Table 5.2 and represented in form of bar charts in Figures 5.15 and 5.16.

Table 5.2: Results summary of the four cases

	non-optimal (2)	Min. power	non-optimal (1)	Min. time
Average non-dimensional power	1.2452	0.7742	2.7506	4.7260
Endurance (s)	59.6	5.8	21.0	2.7

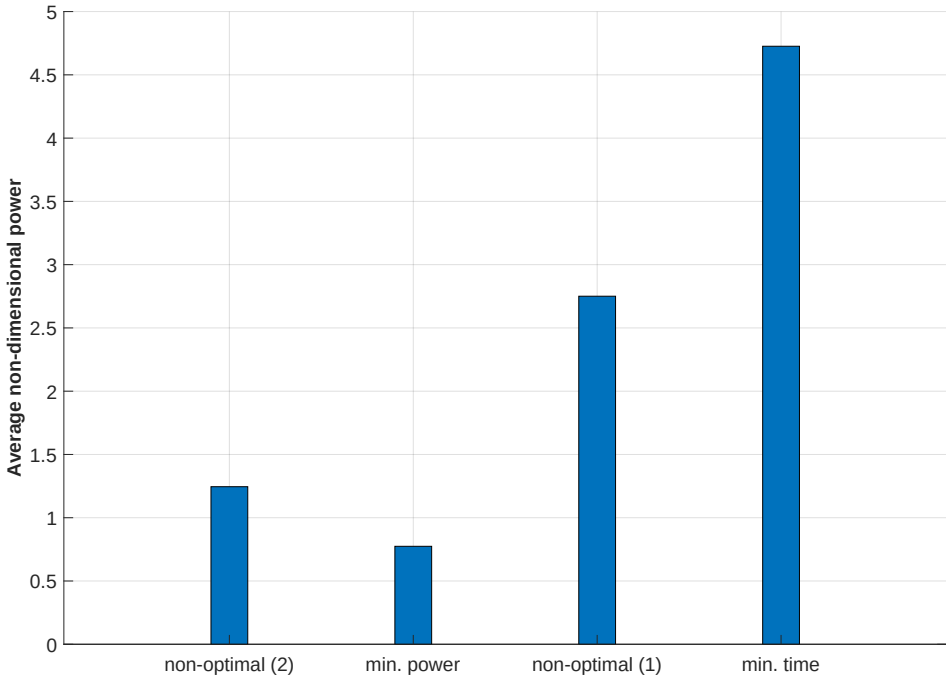

Figure 5.15: Bar chart of the average non-dimensional power of the 4 cases.

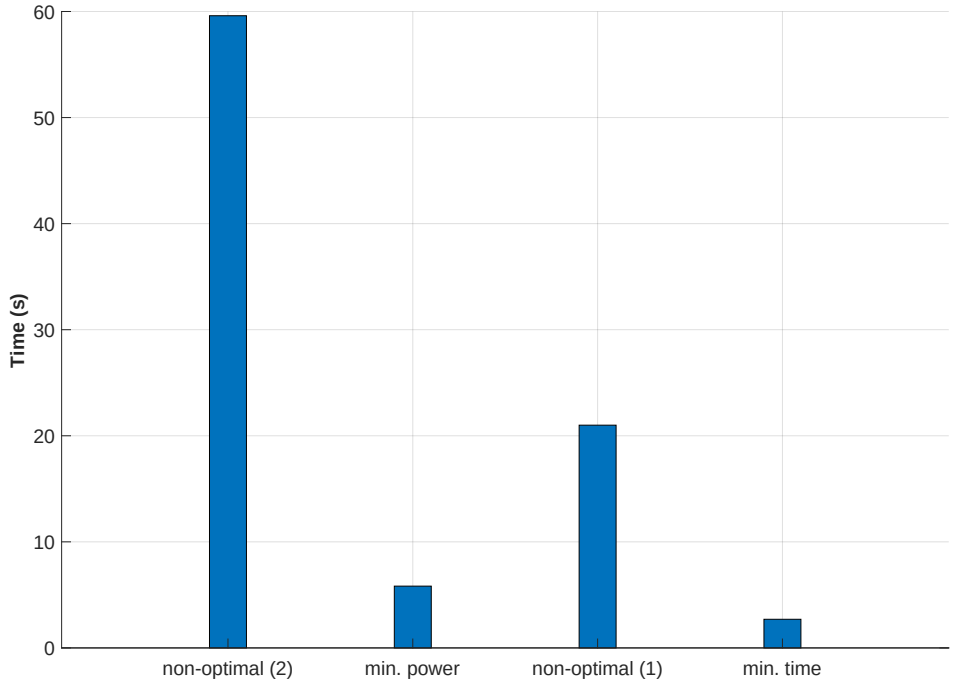

Figure 5.16: Bar chart of the endurance of the 4 cases.

5.5 Conclusion

Throughout this study, a technique for determining the optimal path of the transition phase, which is the middle phase of the 3 phases of the AWE full power cycle, was presented using direct method of optimal control. Two optimality criteria are utilized. The genuine concern is minimizing the control action or the consumption of power, or, equivalently, maximizing the net power gain. Also, the case of minimizing the flight endurance was explored for comparative purposes. Based on the aircraft characteristics, aerodynamic forces and moments, and boundary conditions of the pertinent optimal control problem, a several simulations, subjected to the both optimality criteria, were made. The optimal path was simulated for the two aforementioned criteria. Also, the required thrust over the transition phase was calculated, this parameter is important as it is a design parameter needed for choosing the capabilities of the rotors. By compar-

ing the results of the two criteria, it was noticed that time interval difference between the 2 cases is almost 3 s only, but with big difference in the consumed power. A huge reduction in the mass of the airborne component (battery) could be achieved, within the transition phase, by applying the minimization of energy criteria. This will lead to a better effect on the harvesting and cut-in wind speed. Even though there is a lot of attempts to control the flying device of the airborne system with several control techniques, the current work is considered one of the rare attempts to control the aircraft during the transition phase within the AWE community. A forthcoming sequel of the current work by extending the simulation to cover the full power cycle.

Chapter 6

Conclusion and Future Work

Due to the energy crisis and the increasing interest in renewable energy to cover the need for electricity because of modern life styles, a new emerging technology called Airborne Wind Energy was established. The most prominent features for this technology over horizontal axial wind turbine is that it could reach higher altitude, with less material and foundations. This thesis is concerned with AWE from three aspects:

Kite Power System Development

A kite power system prototype was built, aiming to generate 7 kW of electricity. This system consists of a soft kite connected to the ground using a Dyneema tether. The kite is controlled by a kite control unit (KCU), which consists of a servo motor that receives the control action from the remote control, and a lithium battery as a power source. With mounting a small measurement unit, which was built from scratch, on the kite it was able to measure the kite's position (longitude - latitude - hight), kite's orientation (roll - pitch - yaw). Then connecting a load cell to the main tether/power line, which plays the role of tension meter to measure the amount of tension force produced, which will give an indication of the power production.

By performing a fixed KCU flight test, the average resultant tension force was 350 N, which is promising. After that, a moving KCU flight test was performed by putting the KCU on a truck deck, in this configuration, it could be considered that the kite speed equal to the truck speed in case of non-windy days. For this reason, a speed sensor was added to the truck, so it could be possible to know the apparent wind speed of the kite. Several experiments were designed, based on the flight maneuver, towing speed, and control line length, which is an indication of the nominal angle of attack. The collected data is used in the data analysis part.

Data Analysis

The data collected during the experiment were analyzed using two approaches: System Identification of the kite behavior in real-time. This was done by benefiting from the tension meter data with the kite's orientation data from the measurement unit; specifically the rolling angle data. Using these two sets of data, it was able to build a transfer function that identifies the kite behavior, using Placket's algorithm. This will allow applying and implementing any control technique to stabilize the kite in real-time, as future work.

After enhancing the collected data and performing the moving KCU flight test, an intensive sensitivity analysis was made to study the important features that correlate with the output tension. Also, a comparison between the data-based and model-based sensitivity analysis was represented and showed consistency. Then several machine learning algorithms were applied to predict the power. It was found that the neural network algorithm is the most promising with less error according to the quality metrics. As future work, a further enhancement will be done to the data collection process and a hyper-parameter tuning of the machine learning models will be made.

The data analysis part is considered the main novel part of the thesis. Especially, the machine learning part, as these techniques wasn't used before within the AWE commu-

nity and the findings were promising. Also, the data-based system identification of the kite is valuable for the AWE community.

Modeling & Control

Due to the launching problem that faces the soft kites, several companies moved using rigid aircraft as the flying device of the AWE system. Modeling and control of a rigid VTOL aircraft were presented. It was assumed that the Ampyx power AP-2 aircraft has VTOL capabilities as a tail-sitter. An optimal control technique was applied to perform the transition from the vertical take-off to forward flight. The trajectory and power consumption were simulated for two cases of optimality; minimizing the power consumption and minimizing the endurance. The first case was more reasonable for the current application as it shows less power consumption and the main goal is to generate energy. As future work, the transition phase simulation will be accompanied by the remaining 2 phases to simulate the whole power cycle. This work is considered one of a few attempts that addressed the transition phase within the AWE community and its novel from point of view of the control method. Taking in consideration that this aircraft wasn't addressed within the transition phase before.

Appendices

Appendix A

Plackett's Algorithm

In this appendix, the Plackett's algorithm will be illustrated in details [55, 56]. The open-loop TF for the kite in z-form [106] can be approximated as

$$G(z^{-1}) = \frac{Y(z^{-1})}{U(z^{-1})} = \frac{B(z^{-1})}{A(z^{-1})}, \tag{A.1}$$

where $A(z^{-1})$ and $B(z^{-1})$ are considered as second order polynomial equations in z-form

$$A(z^{-1}) = 1 + a_1 z^{-1} + a_2 z^{-2}, \tag{A.2}$$

$$B(z^{-1}) = b_1 z^{-1} + b_2 z^{-2}. \tag{A.3}$$

The coefficients a_1, a_2, b_1 and b_2 are varying with time because of the change in the system dynamics. The kite is also exposed to a time-varying apparent wind speed which is not available in real time.

Substituting Eqs. (A.2) and (A.3) into Eq. (A.1), then obtain

$$\frac{Y}{U}(z^{-1}) = G(z^{-1}) = \frac{b_1 z^{-1} + b_2 z^{-2}}{1 + a_1 z^{-1} + a_2 z^{-2}}. \tag{A.4}$$

This equation can be rewritten in difference form

$$Y_k = -a_1 Y_{k-1} - a_2 Y_{k-2} + b_1 U_{k-1} + b_2 U_{k-2}, \tag{A.5}$$

or reformulated as a matrix expression

$$Y_k = \mathbf{X}_{k-1}^{\top} \boldsymbol{\theta}_{k-1}, \tag{A.6}$$

where

$$\mathbf{X}_{k-1} = [Y_{k-1},\ Y_{k-2},\ U_{k-1},\ U_{k-2}]^{\top}, \tag{A.7}$$

$$\boldsymbol{\theta}_{k-1} = [-a_1,\ -a_2,\ b_1,\ b_2]^{\top}. \tag{A.8}$$

From Eq. (A.6), the MSE can be written as

$$MSE = \frac{1}{k} \sum_{r=1}^{k} \left(\mathbf{X}_{r-1}^{\top} \boldsymbol{\theta}_{r-1} - Y_{m,r} \right)^2. \tag{A.9}$$

The objective of the SI algorithm is to obtain the values of the coefficient matrix $\boldsymbol{\theta}$ that minimize the MSE. From the derivation, these values can be calculated as

$$\boldsymbol{\theta}_k = \mathbf{P}_k \sum_{r=1}^{k} \mathbf{X}_{r-1} Y_{m,r}, \tag{A.10}$$

where $\mathbf{P}_{k-1}$ is a square matrix such that

$$\mathbf{P}_{k-1} = \left[\sum_{r=1}^{k} (\mathbf{X}_{r-1} \mathbf{X}_{r-1}^{\top}) \right]^{-1}. \tag{A.11}$$

From Eq. (A.11), the following could be obtained

$$\mathbf{P}_k^{-1} = \mathbf{P}_{k-1}^{-1} + \left(\mathbf{X}_{k-1} \mathbf{X}_{k-1}^{\top} \right). \tag{A.12}$$

Equation (A.10) is now rewritten as

$$\boldsymbol{\theta}_k = \mathbf{P}_k \left[\mathbf{X}_{k-1} Y_{m,k} + \sum_{r=1}^{k-1} \left(\mathbf{X}_{r-1} Y_{m,r} \right) \right]. \tag{A.13}$$

From Eqs. (A.13) and (A.10) it could be found that

$$\boldsymbol{\theta}_k = \mathbf{P}_k \mathbf{X}_{k-1} Y_{m,k} + \mathbf{P}_k \mathbf{P}_{k-1}^{-1} \boldsymbol{\theta}_{k-1}. \tag{A.14}$$

Equation (A.12) can be rewritten as

$$\mathbf{P}_{k-1}^{-1} = \mathbf{P}_k^{-1} - \left(\mathbf{X}_{k-1} \mathbf{X}_{k-1}^{\top} \right). \tag{A.15}$$

Substituting Eq. (A.15) into Eq. (A.14), then obtain

$$\boldsymbol{\theta}_k = \boldsymbol{\theta}_{k-1} + \mathbf{P}_k \mathbf{X}_{k-1} \left(Y_{m,k} - \mathbf{X}_{k-1}^{\top} \boldsymbol{\theta}_{k-1} \right). \tag{A.16}$$

In Eq. (A.16), the term $\mathbf{P}_k$ is unknown, thus applying the Lemma formula [107] to Eq. (A.15) to arrive at

$$\mathbf{P}_k = \mathbf{P}_{k-1} - \frac{\mathbf{P}_{k-1} \mathbf{X}_{k-1} \mathbf{X}_{k-1}^{\top} \mathbf{P}_{k-1}}{1 + \mathbf{X}_{k-1}^{\top} \mathbf{P}_{k-1} \mathbf{X}_k}. \tag{A.17}$$

Finally, substitute Eq. (A.17) into Eq. (A.16) to obtain

$$\boldsymbol{\theta}_k = \boldsymbol{\theta}_{k-1} - \frac{\mathbf{P}_{k-1} \mathbf{X}_{k-1}}{1 + \mathbf{X}_k^{\top} \mathbf{P}_{k-1} \mathbf{X}_{k-1}} \left(\mathbf{X}_{k-1}^{\top} \boldsymbol{\theta}_{k-1} - Y_{m,k} \right). \tag{A.18}$$

Thus, the unknown parameters a_1, a_2, b_1 and b_2 have to be calculated in every time step as $\boldsymbol{\theta}_k = [-a_{1,k} \quad -a_{2,k} \quad b_{1,k} \quad b_{2,k}]^{\top}$ to update the estimated course angle χ given in Eq. (A.5). The following calculation steps are required to obtain these parameters. First, the matrix $\mathbf{P}_{k-1}$ is initialized with large positive numbers on the leading diagonal and zeros on the off-diagonal elements. The matrix $\boldsymbol{\theta}_{k-1}$ must be populated with initial

parameters close to the model. Then. the simulation results of the SI algorithm are obtained by:

1. $\mathbf{X}_k$ is updated every sample time by the system outputs and inputs as defined before.

2. Calculate $\boldsymbol{\theta}_k$ and $\mathbf{P}_k$ from Eqs. (A.18) and (A.17), respectively.

3. Update $\boldsymbol{\theta}_{k-1}$ and $\mathbf{P}_{k-1}$ with $\boldsymbol{\theta}_k$ and $\mathbf{P}_k$, respectively.

4. Repeat the loop for each time step.

Appendix B

KCU Design

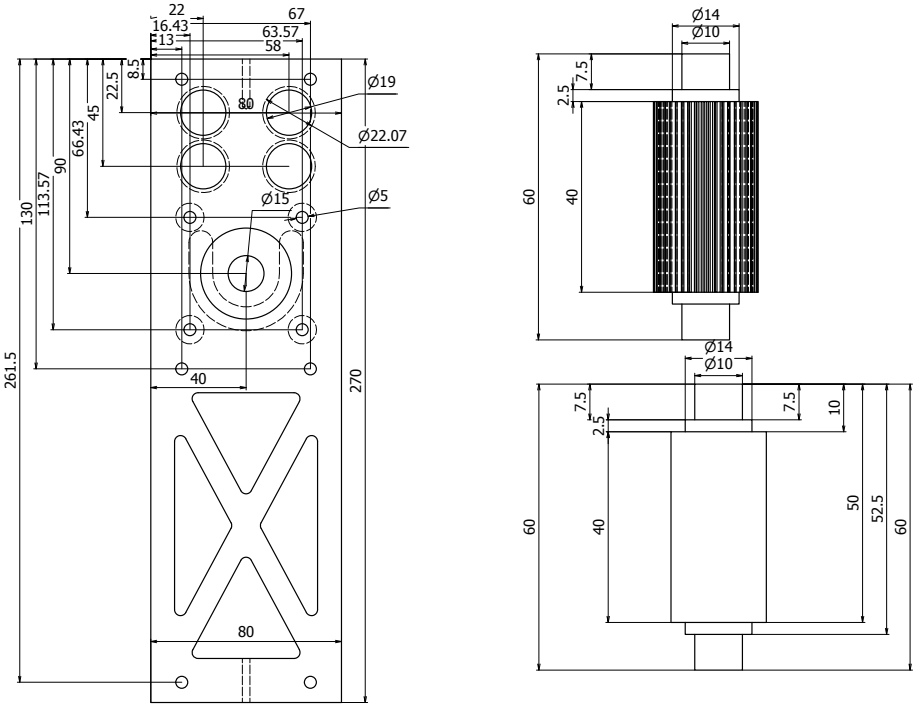

(a) casing dimensions

(b) pulley dimensions

Figure B.1: Detailed KCU design with dimensions in mm.

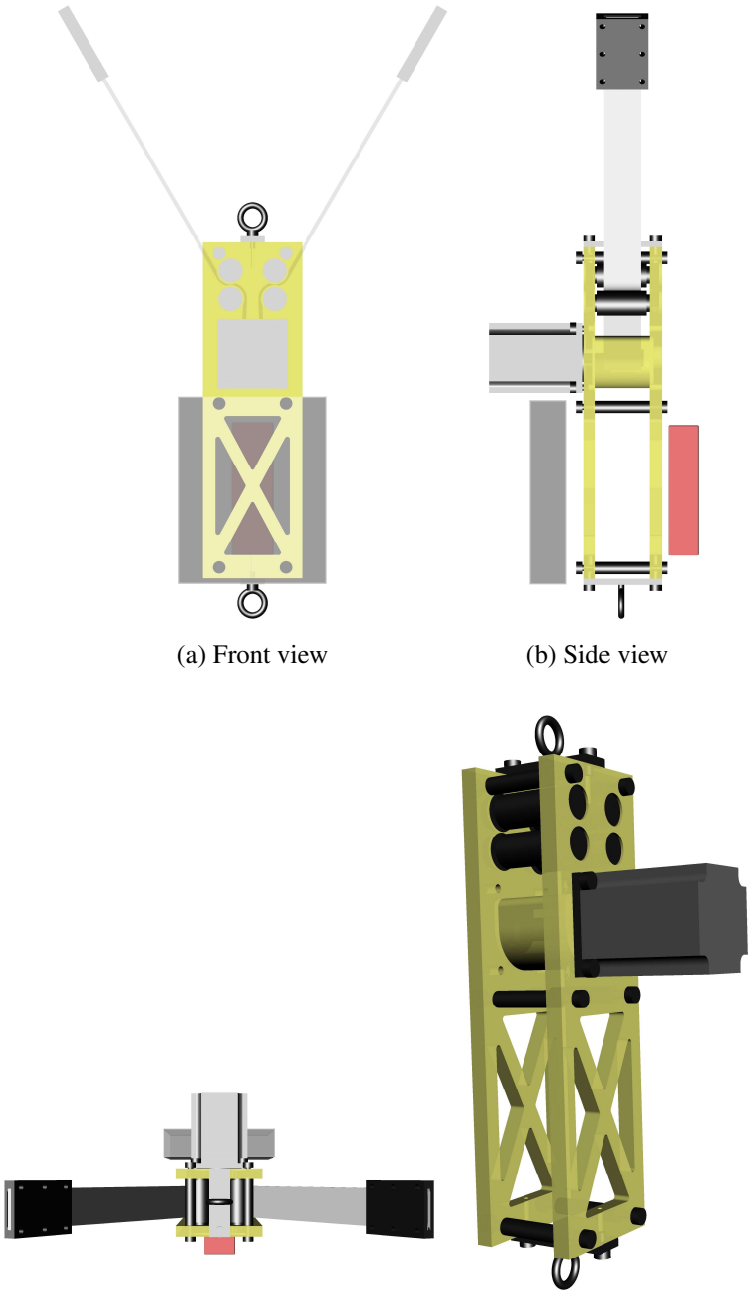

(a) Front view

(b) Side view

(c) Top view

(d) 3D view

Figure B.2: The 3 views of the KCU.

Bibliography

[1] Human Development Index. http://hdr.undp.org/en/content/human-development-index-hdi. Accessed 28 May 2020.

[2] RENEWABLES 2019 GLOBAL STATUS REPORT. http://www.ren21.net/gsr-2019/. Accessed 28 May 2020.

[3] GLOBAL WIND REPORT 2019. https://gwec.net/global-wind-report-2019/. Accessed 12 August 2020.

[4] K. Padmanathan, N. Kamalakannan, P. Sanjeevikumar, F. Blaabjerg, J. B. Holm-Nielsen, G. Uma, R. Arul, R. Rajesh, A. Srinivasan, and J. Baskaran, "Conceptual framework of antecedents to trends on permanent magnet synchronous generators for wind energy conversion systems," *Energies*, vol. 12, no. 13, p. 2616, 2019.

[5] M. Noom, *Theoretical analysis of mechanical power generation by pumping cycle kite power systems*. PhD thesis, Delft University of Technology, 2013.

[6] R. van der Vlugt, J. Peschel, and R. Schmehl, "Design and experimental characterization of a pumping kite power system," in *Airborne Wind Energy* (U. Ahrens, M. Diehl, and R. Schmehl, eds.), Green Energy and Technology, ch. 23, pp. 403–425, Berlin Heidelberg: Springer, 2013.

[7] AWESCO network, "Airborne wind energy - an introduction to an emerging technology." http://www.awesco.eu/awe-explained. Accessed 14 Feb 2020.

[8] U. Fechner, *A Methodology for the Design of Kite-Power Control Systems*. PhD thesis, Delft University of Technology, 2016.

[9] V. Salma, F. Friedl, and R. Schmehl, "Reliability and safety of airborne wind energy systems," *Wind Energy*, vol. 23, no. 2, pp. 340–356, 2019.

[10] Ozone Kites. https://ozonekites.com/products/water-kites/uno-v2/. Accessed 21 May 2020.

[11] M. A. Rushdi, T. N. Dief, S. Yoshida, and R. Schmehl, "Towing test data set of the kyushu university kite system," *Data*, vol. 5, no. 3, p. 69, 2020.

[12] N. Takiguchi, "Development of kite control unit for wind power generation," Master's thesis, Kyushu University, 2018.

[13] S. Haug, "Design of a kite launch and retrieval system for a pumping high altitude wind power generator," Master's thesis, 2012.

[14] KiteGen S.r.l. http://www.kitegen.com/en/. Accessed 14 Feb 2020.

[15] Skysails Power GmbH. https://skysails-power.com/. Accessed 14 Feb 2020.

[16] Alula Energy. http://energykitesystems.net/AlulaEnergy/index.html. Accessed 14 Feb 2020.

[17] Ampyx Power B.V. http://www.ampyxpower.com/. Accessed 30 December 2016, 2016.

[18] M. Rushdi, A. Hussein, T. N. Dief, S. Yoshida, and R. Schmehl, "Simulation of the transition phase for an optimally-controlled tethered vtol rigid aircraft for airbornewind energy generation," in *AIAA Scitech 2020 Forum*, p. 1243, 2020.

[19] L. Goldstein, "Airborne wind energy conversion systems with ultra high speed mechanical power transfer," in *Airborne Wind Energy*, pp. 235–247, Springer, 2013.

[20] S. W. Popper, R. J. Lempert, and S. C. Bankes, "Shaping the future," *Scientific American*, vol. 292, no. 4, pp. 66–71, 2005.

[21] C. Boyle and G. T. K. Coates, "Sustainability principles and practice for engineers," *IEEE Technology and Society Magazine*, vol. 24, no. 3, pp. 32–39, 2005.

[22] I. Dincer, "Renewable energy and sustainable development: a crucial review," *Renewable and sustainable energy reviews*, vol. 4, no. 2, pp. 157–175, 2000.

[23] P. T. Anastas and J. B. Zimmerman, "Peer reviewed: design through the 12 principles of green engineering," 2003.

[24] A. M. A. Rushdi, "Engineering thinking on exploring the future," *Engineering Sciences*, vol. 20, no. 2, 2009.

[25] R. Schmehl, ed., *Airborne wind energy: advances in technology development and research*. Green Energy and Technology, Singapore: Springer, 2018.

[26] U. Ahrens, M. Diehl, and R. Schmehl, eds., *Airborne Wind Energy*. Green Energy and Technology, Berlin Heidelberg: Springer, 2013.

[27] A. Cherubini, A. Papini, R. Vertechy, and M. Fontana, "Airborne wind energy systems: A review of the technologies," *Renewable and Sustainable Energy Reviews*, vol. 51, pp. 1461–1476, 2015.

[28] A. K. d. S. Mendonça, C. R. Vaz, Á. G. R. Lezana, C. A. Anacleto, and E. P. Paladini, "Comparing patent and scientific literature in airborne wind energy," *Sustainability*, vol. 9, no. 6, p. 915, 2017.

[29] J. Samson, R. Katebi, and C. Vermillion, "A critical assessment of airborne wind energy systems," in *2nd IET Renewable Power Generation Conference*, pp. 4–7, IET, 2013.

[30] M. L. Loyd, "Crosswind kite power (for large-scale wind power production)," *Journal of energy*, vol. 4, no. 3, pp. 106–111, 1980.

[31] W. J. Ockels, "Laddermill, a novel concept to exploit the energy in the airspace," *Aircraft design*, vol. 4, no. 2, pp. 81–97, 2001.

[32] P. Williams, B. Lansdorp, and W. Ockesl, "Optimal crosswind towing and power generation with tethered kites," *Journal of guidance, control, and dynamics*, vol. 31, no. 1, pp. 81–93, 2008.

[33] A. Cherubini, R. Vertechy, and M. Fontana, "Simplified model of offshore airborne wind energy converters," *Renewable Energy*, vol. 88, pp. 465–473, 2016.

[34] Kitenergy S.r.l. http://www.kitenergy.net/. Accessed 14 Feb 2020.

[35] Kitepower B.V. https://kitepower.nl/. Accessed 14 Feb 2020.

[36] P. Bechtle, M. Schelbergen, R. Schmehl, U. Zillmann, and S. Watson, "Airborne wind energy resource analysis," *Renewable Energy*, vol. 141, pp. 1103–1116, 10 2019.

[37] Dyneema. https://www.dsm.com/dyneema/en_GB/home.html. Accessed 28 May 2020.

[38] J. Breukels, *An Engineering Methodology for Kite Design*. PhD thesis, Delft University of Technology, 2011.

[39] A. Bosch, R. Schmehl, P. Tiso, and D. Rixen, "Dynamic nonlinear aeroelastic model of a kite for power generation," *Journal of Guidance, Control and Dynamics*, vol. 37, no. 5, pp. 1426–1436, 2014.

[40] T. N. Dief, M. Rushdi, A. Halawa, and S. Yoshida, "Hardwar-in-the-loop (hil) and experimental findings for the 7 kw pumping kite power system," in *AIAA Scitech 2020 Forum*, p. 1244, 2020.

[41] B. Ho and R. E. Kálmán, "Effective construction of linear state-variable models from input/output functions," *at-Automatisierungstechnik*, vol. 14, no. 1-12, pp. 545–548, 1966.

[42] K.-J. Åström and B. Torsten, "Numerical identification of linear dynamic systems from normal operating records," *IFAC Proceedings Volumes*, vol. 2, no. 2, pp. 96–111, 1965.

[43] M. Deistler, "System identification and time series analysis: Past, present, and future," in *Stochastic Theory and Control*, pp. 97–109, Springer, 2002.

[44] L. A. Petersen, B. W. Bequette, S. B. Jørgensen, J. Villadsen, I. Christensen, and K. V. Gernaey, "Modeling and system identification of an unconventional bioreactor used for single cell protein production," *Chemical Engineering Journal*, vol. 390, p. 124438, 2020.

[45] K. Kostoglou, C. Wallinger, and M. Huemer, "Volatility clustering in medical ultrasound imaging and system identification based deconvolution," in *2019 IEEE International Ultrasonics Symposium (IUS)*, pp. 1459–1462, IEEE, 2019.

[46] R. T. Torres and F. Sergii, "Brushless direct current propulsion system identification," in *Integrated Computer Technologies in Mechanical Engineering*, pp. 105–113, Springer, 2020.

[47] M. S. Gandhi, L. Whitcher, E. Theodorou, and E. N. Johnson, "Practical system identification for small vtol unmanned aerial vehicle," in *AIAA Scitech 2019 forum*, p. 1982, 2019.

[48] O. Ibrahim, "Prediction of power output of wind turbines using system identification techniques.," *International Review of Aerospace Engineering*, vol. 13, no. 1, 2020.

[49] T. Weber, J. Sossenheimer, S. Schäfer, M. Ott, J. Walther, and E. Abele, "Machine learning based system identification tool for data-based energy and resource modeling and simulation," *Procedia CIRP*, vol. 80, pp. 683–688, 2019.

[50] G. C. Goodwin, G. GC, and P. RL, "Dynamic system identification. experiment design and data analysis.," 1977.

[51] T. N. Dief, U. Fechner, R. Schmehl, S. Yoshida, and M. A. Rushdi, "Adaptive flight path control of airborne wind energy systems," *Energies*, 2020.

[52] T. N. Dief, U. Fechner, R. Schmehl, S. Yoshida, A. M. Ismaiel, and A. M. Halawa, "System identification, fuzzy control and simulation of a kite power system with fixed tether length," *Wind Energy Science*, vol. 3, no. 1, pp. 275–291, 2018.

[53] G. Licitra, A. Bürger, P. Williams, R. Ruiterkamp, and M. Diehl, "System identification of a rigid wing airborne wind energy system," *arXiv preprint arXiv:1711.10010*, 2017.

[54] G. Licitra, *Identification and Optimization of an Airborne Wind Energy System*. PhD thesis, Albert Ludwig Univ. of Freiburg, Freiburg im Breisgau, Germany, 2018.

[55] T. N. Dief, M. M. Kamra, and S. Yoshida, "Modeling, system identification, and pid-a controller for tethered unmanned quad-rotor helicopter.," *International Review of Aerospace Engineering*, vol. 10, no. 4, pp. 215–223, 2017.

[56] K. Dutton, *The art of control engineering*. Addison-Wesley Longman Publishing Co., Inc., 1997.

[57] C. M. Bishop, *Pattern recognition and machine learning*. springer, 2006.

[58] P. Baldi, S. Brunak, and F. Bach, *Bioinformatics: the machine learning approach*. MIT press, 2001.

[59] K. Kourou, T. P. Exarchos, K. P. Exarchos, M. V. Karamouzis, and D. I. Fotiadis, "Machine learning applications in cancer prognosis and prediction," *Computational and structural biotechnology journal*, vol. 13, pp. 8–17, 2015.

[60] F. Pedregosa, G. Varoquaux, A. Gramfort, V. Michel, B. Thirion, O. Grisel, M. Blondel, P. Prettenhofer, R. Weiss, V. Dubourg, *et al.*, "Scikit-learn: Machine learning in python," *Journal of machine learning research*, vol. 12, no. Oct, pp. 2825–2830, 2011.

[61] A. Paszke, S. Gross, S. Chintala, G. Chanan, E. Yang, Z. DeVito, Z. Lin, A. Desmaison, L. Antiga, and A. Lerer, "Automatic differentiation in pytorch," 2017.

[62] M. Abadi, P. Barham, J. Chen, Z. Chen, A. Davis, J. Dean, M. Devin, S. Ghemawat, G. Irving, M. Isard, *et al.*, "Tensorflow: A system for large-scale machine learning," in *12th {USENIX} Symposium on Operating Systems Design and Implementation ({OSDI} 16)*, pp. 265–283, 2016.

[63] M. Rushdi, S. Yoshida, and T. N. Dief, "Simulation of a tether of a kite power system using a lumped mass model," in *IECES*, (Fukuoka, Japan), pp. 42–47, 2018.

[64] R. van der Vlugt, A. Bley, R. Schmehl, and M. Noom, "Quasi-steady model of a pumping kite power system," *Renewable Energy*, vol. 131, pp. 83–99, 2019.

[65] S. Rapp, R. Schmehl, E. Oland, and T. Haas, "Cascaded pumping cycle control for rigid wing airborne wind energy systems," *Journal of Guidance, Control, and Dynamics*, pp. 1–18, 2019.

[66] J. Oehler and R. Schmehl, "Aerodynamic characterization of a soft kite by in situ flow measurement," *Wind Energy Science*, vol. 4, no. 1, pp. 1–21, 2019.

[67] A. Baheri and C. Vermillion, "Altitude optimization of airborne wind energy systems: A bayesian optimization approach," in *2017 American Control Conference (ACC)*, pp. 1365–1370, IEEE, 2017.

[68] G. Licitra, J. Koenemann, A. Bürger, P. Williams, R. Ruiterkamp, and M. Diehl, "Performance assessment of a rigid wing airborne wind energy pumping system," *Energy*, vol. 173, pp. 569–585, 2019.

[69] A. Clifton, L. Kilcher, J. Lundquist, and P. Fleming, "Using machine learning to predict wind turbine power output," *Environmental research letters*, vol. 8, no. 2, p. 024009, 2013.

[70] J. Heinermann and O. Kramer, "Machine learning ensembles for wind power prediction," *Renewable Energy*, vol. 89, pp. 671–679, 2016.

[71] N. A. Treiber, J. Heinermann, and O. Kramer, "Wind power prediction with machine learning," in *Computational sustainability*, pp. 13–29, Springer, 2016.

[72] Z. Ti, X. W. Deng, and H. Yang, "Wake modeling of wind turbines using machine learning," *Applied Energy*, vol. 257, p. 114025, 2020.

[73] M. A. Rushdi, A. A. Rushdi, T. N. Dief, A. M. Halawa, S. Yoshida, and R. Schmehl, "Power prediction of airborne wind energy systems using multivariate machine learning," *Energies*, vol. 13, no. 9, p. 2367, 2020.

[74] A. Saltelli, M. Ratto, T. Andres, F. Campolongo, J. Cariboni, D. Gatelli, M. Saisana, and S. Tarantola, *Global sensitivity analysis: the primer*. John Wiley & Sons, 2008.

[75] R. Schmehl, M. Noom, and R. van der Vlugt, "Traction power generation with tethered wings," in *Airborne Wind Energy* (U. Ahrens, M. Diehl, and R. Schmehl, eds.), Green Energy and Technology, ch. 2, pp. 23–45, Berlin Heidelberg: Springer, 2013.

[76] F. Chollet *et al.* https://keras.io. Accessed 23 Mar 2020.

[77] A. Géron, *Hands-On Machine Learning with Scikit-Learn, Keras, and TensorFlow: Concepts, Tools, and Techniques to Build Intelligent Systems*. O'Reilly Media, 2019.

[78] S. Rapp and R. Schmehl, "Vertical takeoff and landing of flexible wing kite power systems," *Journal of Guidance, Control, and Dynamics*, vol. 41, no. 11, pp. 2386–2400, 2018.

[79] D. Todeschini, L. Fagiano, C. Micheli, and A. Cattano, "Control of vertical take off, dynamic flight and landing of hybrid drones for airborne wind energy systems," in *2019 American Control Conference (ACC)*, pp. 2177–2182, IEEE, 2019.

[80] P. Martin, S. Devasia, and B. Paden, "A different look at output tracking: control of a vtol aircraft," *Automatica*, vol. 32, no. 1, pp. 101–107, 1996.

[81] L. Fagiano, E. Nguyen-Van, F. Rager, S. Schnez, and C. Ohler, "Autonomous takeoff and flight of a tethered aircraft for airborne wind energy," *IEEE Transactions on Control Systems Technology*, vol. 26, no. 1, pp. 151–166, 2017.

[82] L. Fagiano, E. N. Van, and S. Schnez, "Linear take-off and landing of a rigid aircraft for airborne wind energy extraction," in *Airborne Wind Energy*, pp. 491–514, Springer, 2018.

[83] L. Fagiano, E. Nguyen-Van, F. Rager, S. Schnez, and C. Ohler, "Automatic take-off of a tethered aircraft for airborne wind energy: Control design and experimental results," *IFAC-PapersOnLine*, vol. 50, no. 1, pp. 11932–11937, 2017.

[84] A. Schanen, J. Dumon, N. Meslem, and A. Hably, "On using drones for the take-off and landing phases of an awe system," in *Proceedings of the Airborne Wind Energy Conference*, p. 142, 15-16 October 2019.

[85] S. M. Amin, K. H. Ibrahim, A. Al-Naggar, A. Nabil, A. El-Sadek, M. Abdel-Galil, and A. H. Badawi, "Parametrized experience exchange in expert-fellow swarm robotic system, controller performance context," in *AIAA Information Systems-AIAA Infotech@ Aerospace*, p. 1066, 2017.

[86] S. Rapp, R. Schmehl, E. Oland, S. Smidt, T. Haas, and J. Meyers, "A modular control architecture for airborne wind energy systems," in *AIAA Scitech 2019 Forum*, p. 1419, 2019.

[87] M. A. Rushdi and A. M. Rushdi, "On the fundamental masses derivable by dimensional analysis.," *Journal of King Abdulaziz University: Engineering Sciences*, vol. 27, no. 1, pp. 35–42, 2016.

[88] Z. Li, L. Zhang, H. Liu, Z. Zuo, and C. Liu, "Nonlinear robust control of tail-sitter aircrafts in flight mode transitions," *Aerospace Science and Technology*, vol. 81, pp. 348–361, 2018.

[89] Z. Liu, J. Guo, M. Li, S. Tang, and X. Wang, "Vtol uav transition maneuver using incremental nonlinear dynamic inversion," *International Journal of Aerospace Engineering*, vol. 2018, 2018.

[90] P. Casau, D. Cabecinhas, and C. Silvestre, "Autonomous transition flight for a vertical take-off and landing aircraft," in *2011 50th IEEE Conference on Decision and Control and European Control Conference*, pp. 3974–3979, IEEE, 2011.

[91] J. Zhou, X. Lyu, Z. Li, S. Shen, and F. Zhang, "A unified control method for quadrotor tail-sitter uavs in all flight modes: Hover, transition, and level flight," in *2017 IEEE/RSJ International Conference on Intelligent Robots and Systems (IROS)*, pp. 4835–4841, IEEE, 2017.

[92] M. Kokume and K. Uchiyama, "Control architecture for transition from level flight to hover of a fixed-wing uav," in *IECON 2011-37th Annual Conference of the IEEE Industrial Electronics Society*, pp. 522–527, IEEE, 2011.

[93] A. Elsadek, H. E. Taha, and G. M. El-Bayoumi, "Stability analysis of longitudinal dynamics of hovering flapping mavs/insects," in *AIAA Atmospheric Flight Mechanics Conference*, p. 1635, 2017.

[94] A. A. Hussein, A. E. Seleit, H. E. Taha, and M. R. Hajj, "Optimal transition of flapping wing micro-air vehicles from hovering to forward flight," *Aerospace Science and Technology*, vol. 90, pp. 246–263, 2019.

[95] M. Zanon, A. Boccia, V. G. S. Palma, S. Parenti, and I. Xausa, "Direct optimal control and model predictive control," in *Optimal Control: Novel Directions and Applications*, pp. 263–382, Springer, 2017.

[96] P. Falugi, E. Kerrigan, and E. Van Wyk, "Imperial college london optimal control software user guide (iclocs)," *Department of Electrical and Electronic Engineering, Imperial College London, London, England, UK*, 2010.

[97] Y. Nie, O. Faqir, and E. C. Kerrigan, "Iclocs2: Try this optimal control problem solver before you try the rest," in *2018 UKACC 12th International Conference on Control (CONTROL)*, pp. 336–336, IEEE, 2018.

[98] Z. Foroozandeh, M. do rosário de Pinho, and M. Shamsi, "On numerical methods for singular optimal control problems: An application to an auv problem," *Discrete & Continuous Dynamical Systems-B*, vol. 24, no. 5, p. 2219, 2019.

[99] J. C. Butcher, "Implicit runge-kutta processes," *Mathematics of Computation*, vol. 18, no. 85, pp. 50–64, 1964.

[100] S. O. Fatunla, *Numerical methods for initial value problems in ordinary differential equations*. Academic Press, 2014.

[101] L. T. Biegler and V. M. Zavala, "Large-scale nonlinear programming using ipopt: An integrating framework for enterprise-wide dynamic optimization," *Computers & Chemical Engineering*, vol. 33, no. 3, pp. 575–582, 2009.

[102] A. Wächter, "Short tutorial: getting started with ipopt in 90 minutes," in *Dagstuhl Seminar Proceedings*, Schloss Dagstuhl-Leibniz-Zentrum für Informatik, 2009.

[103] L. T. Biegler, "Efficient nonlinear programming algorithms for chemical process control and operations," in *IFIP Conference on System Modeling and Optimization*, pp. 21–35, Springer, 2007.

[104] W. Chuan, Y. Lei, and Z. Jianguo, "Study on optimization of radiological worker allocation problem based on nonlinear programming function-fmincon," in *2014*

IEEE International Conference on Mechatronics and Automation, pp. 1073–1078, IEEE, 2014.

[105] F. Benhamida, "A new solution method to economic dispatch using the matlab function (fmincon)," in *Conference International AMSE MS*, vol. 5, 2016.

[106] R. Burns, *Advanced control engineering*. London: Butterworth-Heinemann, 1 ed., 2001.

[107] W. W. Hager, "Updating the inverse of a matrix," *SIAM review*, vol. 31, no. 2, pp. 221–239, 1989.

Vitae

MOSTAFA Ali Rushdi was born in Jeddah, KSA in October, 1991. In 2013, he got his Bachelor of Science degree in Aerospace Engineering from the Faculty of Engineering, Cairo University. Afterwards, he pursed his Master studies in the same department majoring in Guidance & Control and got his Master of Science in Aerospace Engineering in 2017. During the period 2013-2017, he was employed as a teaching assistant in the Mechatronics Department, at the Faculty of Engineering and Technology at Future University in Egypt (FUE). In October 2017, he joined the Earth System Science and Technology department in the Interdisciplinary Graduate School of Engineering Sciences at Kyushu University as a PhD student working on the modeling/control and data analysis of Kite power systems.

List of publications

Peer-Reviewed Journal Articles

- "Towing Test Data Set of the Kyushu University Kite System.", **Mostafa A. Rushdi**, Tarek N. Dief, Shigeo Yoshida, Roland Schmehl, Data (2020)

- "Power Prediction using Multivariate Machine Learning in Airborne Wind Energy Systems.", **Mostafa A. Rushdi**, Ahmad A. Rushdi, Tarek N. Dief, Amr M. Halawa, Shigeo Yoshida, Roland Schmehl, energies (2020)

- "System Identification of 6 m^2 Kite power system in Fixed-Tether Length Operation.", **Mostafa A. Rushdi**, Tarek N. Dief, Amr M. Halawa, Shigeo Yoshida, International Review of Aerospace Engineering (2020)

- "Adaptive Flight Path Control of Airborne Wind Energy Systems.", Tarek N. Dief, Uwi Fechner, Roland Schmehl, Shigeo Yoshida, **Mostafa A. Rushdi**, energies

Peer-Reviewed Conference Articles

- "Simulation of the Transition Phase for an Optimally-Controlled Tethered VTOL Rigid Aircraft for Airborne Wind Energy Generation." **Mostafa A. Rushdi**, Ahmad A. Hussein, Tarek N. Dief, Shigeo Yoshida, Roland Schmehl, AIAA SciTech Forum, pp.1243, Orlando, Florida, , USA, January 6^{th} - 10^{th}, 2020.

- "Hardware-in-the-Loop (HIL) and Experimental Findings for the 7 kW Pumping Kite Power Syatem." Tarek N. Dief, **Mostafa A. Rushdi**, Amr M. Halawa, , Shigeo Yoshida, AIAA SciTech Forum, pp.1244, Orlando, Florida, , USA, January 6^{th} - 10^{th}, 2020.

- "Hardware-in-the-Loop (HIL) and System Identification of a Pumping Kite Power",

Tarek N. Dief, **Mostafa A. Rushdi**, Amr M. Halawa, , Shigeo Yoshida, Wind Energy Science Conference (AWEC), Glasgow, UK, October 15^{th} 2019.

- "Aeroelastic CFD-FEM Study of a Kite for Power Generation." Amr M. Halawa, Tarek N. Dief, **Mostafa A. Rushdi**, Shigeo Yoshida, Wind Energy Science Conference (WESC 2019), Cork, Ireland, June 17^{th} -20^{th} 2019.

- "Modeling and Simulation of Kite Power System using lumped mass model." **Mostafa A. Rushdi**, Shigeo Yoshida, Tarek N. Dief, 20^{th} Cross Straits Symposium on Energy and Environmental Science & Technology (CSS-ESST), Busan, Korea, Nov. 26^{th} - 28^{th}, 2018.

- "Modeling & Simulation of a Tether Connected to a Kite Using a Lumped Mass Model.", **Mostafa A. Rushdi**, Shigeo Yoshida, Tarek N. Dief, 4^{th} International Exchange and Innovation Conference on Engineering & Sciences (IEICES), Fukuoka, Japan, Oct. 18^{th}, 2018.

- "Modeling and control of Kite Power System.", Tarek N. Dief, **Mostafa A. Rushdi**, Shigeo Yoshida, Grand Renewable Energy conference, Yokohama, Japan, June 18^{th} - 23^{rd}, 2018